DYNAMIC ANALYSIS OF CAGE SYSTEMS UNDER WAVES AND CURRENT FOR OFFSHORE AQUACULTURE

A Dissertation

by

CRISTIAN ALEJANDRO CIFUENTES SALAZAR

Submitted to the Office of Graduate and Professional Studies of
Texas A&M University
in partial fulfillment of the requirements for the degree of

DOCTOR OF PHILOSOPHY

Chair of Committee,	Moo-Hyun Kim
Committee Members,	Jun Zhang
	Michael Masser
	Richard S. Mercier
Head of Department,	Sharath Girimaji

May 2016

Major Subject: Ocean Engineering

ABSTRACT

The accurate computation of forces and corresponding deformation of cages subjected to waves and current loading is critical to the design of mooring systems for fish farms. In the present work, a complete methodology describing the numerical modeling of net structures and its corresponding interaction with mooring lines and floating platforms has been developed. The effect of every element on the cage over the global response and the effective numerical representation of these components of a cage system are studied.

The numerical model of cages is built and calculated using the commercial software OrcaFlex *v9.6*a. In this software, an equivalent net model is created using an array of cylinders connected by buoys. This model has the same wet mass, axial stiffness and projected area as the prototype net, allowing for the accurate calculation of forces and deformations over the cage due to wave and current loading. A variable drag coefficient formulation is implemented in the software, based on the relative normal velocity between line elements and fluid. This drag coefficient is fed into the modified version of the Morison equation, which accounts for relative motion, to obtain the drag force on the netting using the cross flow principle. In addition, shielding effect is included in the calculations by using riser interaction models. Furthermore, blockage due to large deformations of flexible cages is also accounted for by the derivation of a semi empirical formulation for drag coefficient on Raschel nets.

Careful validation of the present methodology is conducted by comparing numerical results with experimental published data. Validation is presented for a single cage, which includes a surface flexible collar, netting, ballast and mooring lines. Applied loads include current, regular waves and a combination of regular waves and current to evaluate interaction effects. The influence of wave kinematics stretching models on mooring line tension results is also analyzed. Additionally, calculations considering irregular waves and following current are performed for the completeness of the study.

Further analyses consider the coupled response of a mooring/platform/cage system. The system intends to describe the interaction of a single cage and a feeder vessel installed in deep water. Effects of the location of the cage in the water column and the net selection on the dynamics of the platform are studied. The results are qualitatively compared against field measurements in a similar installation 6 miles offshore of Kona Hawaii.

This study can directly be applied to the calculation of the coupled response of multiple technologies such as floating offshore wind turbines, wave energy conversion and offshore fish farming.

DEDICATION

To Ana Victoria Suescún Torres for all the love, support, encouragement, time, miles ran and travelled, tears and laughs, but overall, for all the memories we share and that are now part of the best years of my life.

ACKNOWLEDGEMENTS

First and foremost, I would like to acknowledge the permanent and invaluable support of my academic advisor Professor Moo-Hyun Kim. His vast knowledge in offshore engineering and interest for innovative research in new topics such as offshore fish farming were key factors in the completion of the present work.

Thanks to my committee members, professors Richard S. Mercier, Jun Zhang and Michael Masser for their insights and guidance during these years.

I would like to thank the Fulbright Commission Chile and the National Commission of Research, Science and Technology CONICYT Chile for their financial support to complete this graduate program. I would also like to thank the financial support from Kampachi Farms LLC. Their technical insight into the topic of offshore aquaculture greatly helped me to better understand the practical aspects of fish farming. Without their valuable assistance this work would not had been possible.

Special thanks to my Alma Mater the Instituto de Ciencias Navales y Marítimas at Universidad Austral de Chile. The encouragement from its faculty and staff members was the main motivation to leave my country and continue my education in the United States. I look forward to develop my academic career at UACh teaching and researching in areas that could contribute to the further development of my country.

To my family in Chile, my mother Ana, my sister Belen and my father Antonio. Thanks for letting me know that nothing is out of reach.

Finally, all these years have been a success not because the papers published or conferences attended, but for all the people that I have met and that are now my friends. Learning about views and experiences from people coming from all over the world is the most valuable lesson from my time at Aggieland.

NOMENCLATURE

S_n	Solidity ratio
HDPE	High Density Polyethylene
Re	Reynolds number
KC	Keulegan Carpenter number
C_d	Drag coefficient
C_M	Inertia coefficient
SFT	Submerged Floating Tunnel
PIV	Particle Image Velocimeter
ADV	Acoustic Doppler Velocimeter
CFD	Computational Fluid Dynamics
TF	Transfer Function
FEM	Finite Element Method
BEM	Boundary Element Method
SPM	Single Point Mooring

TABLE OF CONTENTS

Page

ABSTRACT ii

DEDICATION iv

ACKNOWLEDGEMENTS v

NOMENCLATURE vii

TABLE OF CONTENTS viii

LIST OF FIGURES xi

LIST OF TABLES xvi

1. INTRODUCTION 1

1.1 Background and literature review 1
1.2 Objective and scope 12

2. LOADS ON FLOATING PLATFORMS AND NET STRUCTURES 16

2.1 Introduction 16
2.2 Wave theory formulation 16
2.3 Wave loads on floating structures 21
2.3.1 Diffraction/Radiation theory 22
2.3.2 First order boundary value problem 23
2.3.3 First order potential forces 26
2.3.4 Wave loads in time domain 29
2.4 Floating body motions in regular waves 31
2.5 Line and buoy theory in OrcaFlex 35
2.5.1 OrcaFlex line theory 35
2.5.2 OrcaFlex buoy theory 42
2.5.3 Coupled solution of motion for net and collar 43

3. MOORING LINE DYNAMICS 45

3.1 Introduction 45
3.2 Rod theory 46

4. NUMERICAL SIMULATION OF DRAG FORCE AND DEFORMATION OF NETS UNDER STEADY CURRENT 52

4.1 Introduction 52
4.2 Numerical model of nets 52
4.3 Drag coefficient formulation 56
4.4 Validation using the results by Lader and Enerhaug (2005) 58
4.4.1 Results 60
4.5 Discussion 68

5. NUMERICAL SIMULATION OF THE COUPLED DYNAMIC RESPONSE OF A SUBMERGED FLOATING TUNNEL 71

5.1 Introduction 71
5.2 Numerical simulation of SFT under regular wave loading 74
5.3 Physical experiments 76
5.4 Results of coupled analysis 78
5.5 Discussion 87

6. SHIELDING EFFECT ON NETS UNDER STEADY CURRENT 90

6.1 Introduction 90
6.2 Wake models for riser interaction 91
6.2.1 Huse model 92
6.2.2 Blevins model 93
6.2.3 Modified Blevins model 94
6.3 Numerical implementation of wake models 94
6.3.1 Wake implementation in cages 96
6.4 Application of semi-empirical wake models to a cage under steady current 96
6.4.1 Results 97
6.5 Discussion 113

7. DRAG COEFFICIENT FORMULATION FOR HIGH SOLITY RATIO NETS 115

7.1 Introduction 115
7.2 Drag force calculations for high S_n nets using DeCew et al. (2010) formulation 116
7.2.1 Experiment conditions and net characteristics 117
7.2.2 Numerical models 119
7.2.3 Drag force results using C_d formulation by DeCew et al. (2010) 121
7.3 C_d formulation based on experimental and numerical data 123
7.4 Drag force calculations based on semi-empirical model 127
7.5 Discussion 129

8. FORCES ON CAGES UNDER COMBINED CURRENT AND REGULAR WAVES 133

8.1 Introduction 133
8.2 Numerical model of cage and steady current calculation 135
8.3 Mooring line tension over cage under regular wave loading 138
8.3.1 Influence of wave kinematics extrapolation models on mooring forces 141
8.4 Mooring line tension over cage under regular wave current interaction 149
8.5 Discussion 156

9. FORCES AND MOTION ANALYSIS OF CAGE UNDER IRREGULAR WAVES/CURRENT INTERACTION 159

9.1 Introduction 159
9.2 Description of numerical model and environmental conditions 161
9.3 Mooring line tension analysis 163
9.3.1 Regular wave cases 164
9.3.2 Irregular wave cases 167
9.4 Cage motion analysis under irregular waves 176
9.5 Discussion 185

10. COUPLED ANALYSIS OF MOORING/PLATFORM/CAGE SYSTEM UNDER IRREGULAR WAVES AND CURRENT 188

10.1 Introduction 188
10.2 Description of components 189
10.2.1 Cage 189
10.2.2 Netting materials 191
10.2.3 Mooring lines and buoys 192
10.2.4 Feeder vessel 193
10.3 Environmental conditions 195
10.4 Results 196
10.4.1 Underwater cage results 197
10.4.2 Surface cage results 201
10.4.3 Coupled mooring cage system 204
10.4.4 10 Year storm condition 204
10.4.5 100 Year storm condition 207
10.5 Conclusions 209

11. CONCLUSIONS AND FUTURE WORK 211

11.1 General conclusions 211
11.2 Future work 213

REFERENCES 215

LIST OF FIGURES

Page

Figure 1.1 World capture fisheries and aquaculture production (FAO, 2014) 1

Figure 1.2 Traditional cage fish farm in the south of Chile (Courtesy of http://www.sermar.cl/) 2

Figure 1.3 Circular and square cages (Courtesy of http://www.akvagroup.com/) 2

Figure 1.4 Offshore fish farm (Courtesy of http://www.kampachifarm.com/) 12

Figure 2.1 Time and frequency domain representation of waves (Faltinsen, 1993) 21

Figure 2.2 Basic discretization of line elements (Orcina, 2014) 36

Figure 2.3 Structural line model (Orcina, 2014) 37

Figure 3.1 Rod coordinate system definition (Bae, 2013) 47

Figure 4.1 Net patterns (a) Flattened expanded, (b) Chain-link, (c) Welded, (d) Woven, (e) Nylon knotless. (Tsukrov et al., 2011) 53

Figure 4.2 Net representation (a) Physical net (b) Numerical equivalent net 54

Figure 4.3 Surface floater representation (a) Physical floater (b) Numerical equivalent floater 56

Figure 4.4 Experiment setup (Lader and Enerhaug, 2005) 59

Figure 4.5 Numerical representation of the net 60

Figure 4.6 Coordinates location for volume and area reduction coefficient calculations (Lader and Enerhaug, 2005). 61

Figure 4.7 Cage deformation (Lader and Enerhaug, 2005) 63

Figure 4.8 Calculation matrix from experiments (Lader and Enerhaug, 2005) 63

Figure 4.9 Drag force comparison (a) C_1, (b) C_2, (c) C_3 64

Figure 4.10 Volume reduction coefficient C_{vr} comparison (a) C_1, (b) C_2, (c) C_3 66

Figure 4.11 Area reduction coefficient C_{vr} comparison (a) C_1, (b) C_2, (c) C_3 67

Figure 5.1 SFT under vertical mooring configuration 75

Figure 5.2 Experimental configuration (a) Vertical mooring (VM), (b) inclined mooring (IM) 77

Figure 5.3 Wave elevation, surge and tension variation 79

Figure 5.4 (a) Surge and (b) Heave SFT motions as function of wave height/period. 80

Figure 5.5 (a) Surge and (b) Heave SFT motions as function of water depth. 82

Figure 5.6 Tension force on vertically moored SFT 83

Figure 5.7 Fluid acceleration by OrcaFlex at SFT depth 84

Figure 5.8 (a) Surge and (b) Heave SFT motions for VM and IM as function of wave height and period 85

Figure 5.9 Numerical results for Tension for VM and IM as function of wave height and period. 86

Figure 5.10 Tension force on inclined mooring 87

Figure 6.1 Blevins wake model (Blevins, 2005) 94

Figure 6.2 Wake frame of reference (Wu et al., 2008) 95

Figure 6.3 Wake zone and vertical plane definition U_o represents undisturbed current velocity. 96

Figure 6.4 Time series of drag load under steady current. 98

Figure 6.5 Deformation comparison between (a) Experiments (Lader and Enerhaug, 2005), (b) Model A and (c) Model B. 98

Figure 6.6 Drag force for C_1 using (a) Huse, (b) Blevins and (c) Blevins modified wake model. 100

Figure 6.7 Drag force for C_2 using (a) Huse, (b) Blevins and (c) Blevins modified wake model. 101

Figure 6.8 Drag force for C_3 using (a) Huse, (b) Blevins and (c) Blevins modified wake model. 102

Figure 6.9 Volume reduction coefficient for C_1 using (a) Huse, (b) Blevins and (c) Blevins modified wake model. 103

Figure 6.10 Volume reduction coefficient for C_2 using (a) Huse, (b) Blevins and (c) Blevins modified wake model. 104

Figure 6.11 Volume reduction coefficient for C_3 using (a) Huse, (b) Blevins and (c) Blevins modified wake model. 105

Figure 6.12 Area reduction coefficient for C_1 using (a) Huse, (b) Blevins and (c) Blevins modified wake model. 106

Figure 6.13 Area reduction coefficient for C_2 using (a) Huse, (b) Blevins and (c) Blevins modified wake model. 107

Figure 6.14 Area reduction coefficient for C_3 using (a) Huse, (b) Blevins and (c) Blevins modified wake model. 108

Figure 6.15 Relative error for drag forces (a) C_1, (b) C_2 and (c) C_3. 110

Figure 6.16 Relative error for volume (a) C_1, (b) C_2 and (c) C_3. 111

Figure 6.17 Relative error for area (a) C_1, (b) C_2 and (c) C_3. 112

Figure 7.1 Raschel netting (Kristiansen and Faltinsen, 2012) 118

Figure 7.2 Numerical representation cage used by Moe-Føre et al. (2014) 120

Figure 7.3 Net deformation 120

Figure 7.4 Comparison numerical and experimental results for drag force under steady current (a) $S_n=0.1904$, (a) $S_n=0.2205$, (a) $S_n=0.3020$ and (a) $S_n=0.4340$ 122

Figure 7.5 C_d as a function of Re based on experimental and numerical data. 125

Figure 7.6 C_d as a function of Re and S_n 126

Figure 7.7 C_d as a function of factor $Re*S_n^2$ 126

Figure 7.8 Comparison numerical and experimental results for drag force under steady current using new C_d definition (a) $S_n=0.1904$, (a) $S_n=0.2205$, (a) $S_n=0.3020$ and (a) $S_n=0.4340$ 128

Figure 8.1 Numerical model including cage and mooring lines 137

Figure 8.2 Drag force under current 137

Figure 8.3 Cage deformation comparison for experimental and numerical model 138

Figure 8.4 C_M values as function of Re and KC numbers from (Sarpkaya, 1976) 141

Figure 8.5 Wave kinematics extrapolation methods. 142

Figure 8.6 Maximum mooring line tension over front mooring line under regular wave loading. 143

Figure 8.7 Mean and total tension on front mooring line under regular wave loading..145

Figure 8.8 Mean and total tension on aft mooring line under regular wave loading 146

Figure 8.9 Comparison wave current interaction for $U_C = 0.1$ m/s, front mooring line 151

Figure 8.10 Comparison wave current interaction for $U_C = 0.1$ m/s, aft mooring line..152

Figure 8.11 Comparison wave current interaction for $U_C = 0.2$ m/s front mooring line 153

Figure 8.12 Comparison wave current interaction for $U_C = 0.2$ m/s, aft mooring line..154

Figure 9.1 Input spectrum and wave time series 162

Figure 9.2 Mooring line tension response under waves only condition.....164

Figure 9.3 Mooring line tension under regular wave loading 165

Figure 9.4 Mooring line tension under irregular wave loading.....168

Figure 9.5 Wave elevation and mooring line tension under irregular wave loading 171

Figure 9.6 Spectral density of mooring tension under current and irregular wave loading 173

Figure 9.7 Transfer function of mooring tension under current and irregular wave loading 175

Figure 9.8 Coordinate describing cage motion 177

Figure 9.9 Cage motion under irregular wave loading.....178

Figure 9.10 Wave elevation and cage motion under irregular wave loading.....180

Figure 9.11 Spectral density of cage motion under current and irregular wave loading 182

Figure 9.12 Transfer function of cage motion under current and irregular wave loading 184

Figure 10.1 Mooring/vessel/cage system 195

Figure 10.2 SPM line tension for underwater cage 197

Figure 10.3 Umbilical line tension for underwater cage 197

Figure 10.4 Vessel surge for underwater cage 198

Figure 10.5 Vessel heave for underwater cage 199

Figure 10.6 Vessel pitch for underwater cage 199

Figure 10.7 Cage heave for underwater cage 200

Figure 10.8 Cage surge in underwater conditions (a) Numerical result, (b) GPS tracking. 201

Figure 10.9 SPM line tension for surface cage 202

Figure 10.10 Umbilical line tension for surface cage 202

Figure 10.11 Vessel surge for surface cage 203

Figure 10.12 SPM line tension under 10 year storm event 205

Figure 10.13 Cage surge under 10 year storm event 205

Figure 10.14 Cage heave under 10 year storm event 206

Figure 10.15 SPM line tension under 100 year storm event 207

Figure 10.16 Cage surge under 100 year storm event 208

Figure 10.17 Cage heave under 100 year storm event 208

LIST OF TABLES

Page

Table 4.1 Experimental conditions....59
Table 5.1 Prototype conditions....78
Table 6.1 Average error for drag force....111
Table 7.1 Netting characteristics....119
Table 8.1 Cage characteristics....136
Table 8.2 Regular wave load conditions....139
Table 8.3 Regular wave current interaction conditions....150
Table 9.1 Irregular wave load conditions....162
Table 9.2 Statistics for front mooring line under regular waves....166
Table 9.3 Statistics for aft mooring line under regular waves....166
Table 9.4 Statistics for front mooring line under irregular waves....169
Table 9.5 Statistics for aft mooring line under irregular waves....169
Table 9.6 Statistics for surge cage motion under irregular waves....179
Table 9.7 Statistics for heave cage motion under irregular waves....179
Table 10.1 Cage characteristics....190
Table 10.2 Netting characteristics....192
Table 10.3 Mooring lines material properties....193
Table 10.4 Feeder vessel characteristics....194
Table 10.5 JONSWAP spectrum input data....196

1. INTRODUCTION

1.1 Background and literature review

Aquaculture production has shown a constant rise in the last decades due to the high demand for fish in the world, particularly in Asia, in addition to a plateau on the wild fish capture. These trends can be seen in Figure 1.1 extracted from FAO (2014).

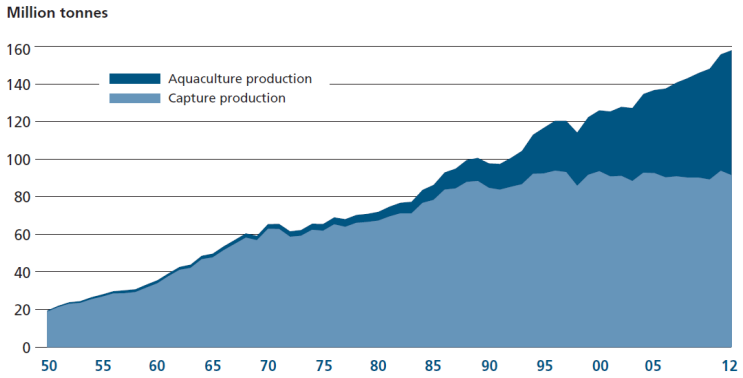

Figure 1.1 World capture fisheries and aquaculture production (FAO, 2014)

The National Oceanic and Atmospheric Administration NOAA defines aquaculture as the process of "breeding, rearing, and harvesting of plants and animals in all types of water environments including ponds, rivers, lakes, and the ocean". In this study, we focus our attention on cage marine aquaculture which can be described as the production of fish in cages installed in open waters.

Traditional cage aquaculture has been widely developed in countries such as Norway and Chile, where near shore areas are populated with fish farms mainly for

salmon production and few other species. A typical installation of a fish farm including an array of cages, mooring system and feeder vessel is presented in Figure 1.2.

Figure 1.2 Traditional cage fish farm in the south of Chile (Courtesy of http://www.sermar.cl/)

The basic component on these fish farms is the cage which contains the fish until it reaches the caliber to be processed and sold in different markets. The most common cages currently installed are square cages made up of steel frames and HDPE circular cages. Both types of cages are presented in Figure 1.3.

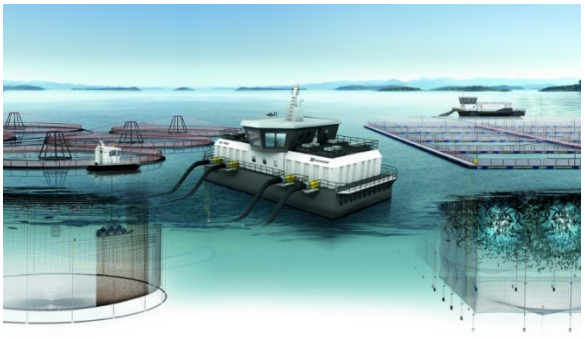

Figure 1.3 Circular and square cages (Courtesy of http://www.akvagroup.com/)

New alternatives to traditional cages, such as Closed Fish Production System (CFPS) are being considered due to the ability to better control the growing conditions of the fish. Its dynamic response under steady current differs from net based structures and further analyses are necessary before this concept can be used in exposed locations (Lader et al., 2014).

Regardless of its shape and building materials, the basic components of a cage system are: a floating surface collar which serves as buoyancy reserve and working platform, lower collar which holds the ballast necessary to extend the net and maintain maximum volume when exposed mainly to current loading, and the net which encloses the fish. For traditional netting, e.g. nylon, besides the main net which is in direct contact with the fish, an external net is used to keep predators away from the fish. New netting materials such as Predator-X, UR-30, Bekaert and Kikko-net are able to sustain shark attacks which allow the use of a single net, increasing the internal flow, promoting constant water exchange inside the cage. These materials are particularly useful for offshore operations. In addition, these netting materials have anti fouling properties which reduces the need for constant maintenance of cages.

The rises of diseases affecting the quality of the fish and environmental concerns about the impact of production centers on local ecosystems have raised questions about the future of the industry. In the early years of aquaculture, production centers were located in coastal areas close to each other and usually near to populated areas to reduce the costs of transport of supplies, workers and the final product (Cifuentes et al., 2014). Generally, closed bays were selected to avoid wave loading over the structures.

However, in these locations, there is not enough water exchange which depletes oxygen and basic nutrients creating challenges to keep the fish alive. A partial solution to these issues is the forced injection of oxygen inside the cages; thus increasing production costs. In addition, calm water promotes the growth of biofouling in the nets increasing the structural mass and drag forces in addition to significantly reduce the flow inside the cage.

To supply the demand, fish cages have increased in volume and biomass density (Jensen et al., 2010). As the industry expanded, remote locations, close to shore, were utilized for aquaculture adding costs and operational challenges. As space has become scarcer, the industry is now looking for new horizons in terms of a more environmentally friendly and profitably manner of production. This leads to the logic development of offshore aquaculture facilities.

In offshore locations, space is unlimited and the presence of strong current reduces risks of diseases or low nutrients concentration (Sims and Key, 2011). In addition, strong current speeds favor the development of the fish since it is swimming most of the time as if it was on wild conditions. In exposed locations, a whole new technological challenge has arisen. In order to endure the environmental conditions offshore, including higher waves, currents and winds, new cages and feeder systems need to be designed. This expansion requires numerical tools to aid in the design, installation and operation of offshore fish farms. These tools need to be able to predict forces and deformations of cage components in addition to describe the interaction between cage, feeder platform and mooring system. Thus, the development of a method

to accurately predict the dynamic response of the different components in a fish farm, and their interaction in high energy seas is the main focus of the present work.

The analysis of forces over nets is a relatively new discipline which only started in the 90's when cage aquaculture began to play an important role in Norway. Meanwhile in the U.S., University of New Hampshire, funded by NOAA/Sea Grant established an experimental site to start the development of the offshore aquaculture industry in waters off the cost of New England.

Given the complexity of the hydroelastic problem of forces over flexible structures, studies have focused on a combination of experimental and numerical work considering current and wave loading. These studies range from the analysis of flow around the basic cruciform structure form by threads and a single knot up to the full description of complex flow patterns on an array of cages including fouling and its biological effects over the fish (Klebert et al., 2013).

The first attempt to calculate forces over net panels can be found in the early work of Aarnes and Loland (1990). In their study, empirical formulations for drag force based on experimental work were presented. In this work, the load over a net panel was calculated based on net geometry and angle of attack of the flow with respect to a net panel. In 1993, the first work to calculate forces over a series of cages was done by Løland (1993) including an empirical formulation for the speed loss of the flow when crossing the netting, effect better known as shielding effect. This study showed the influence of shielding effect on the deformation, oxygen concentration and drag force over cages installed in array configuration.

Later, numerical models were developed specifically for nets. The pioneer work in this matter was done in University of New Hampshire by Tsukrov et al. (2000). In this analysis, an equivalent truss element is used to describe the net. In their study, it was addressed that a simple truss element is not able to model the inertia and net buoyancy of the prototype net at once without adding extra mass to the system. To solve this problem Tsukrov et al. (2002) derived a consistent finite-element model, which represents inertial and structural characteristics of the netting material. This code uses Morison equation to calculate forces over the net and has been tested against experimental results and field measurements showing good agreement under different load scenarios (DeCew et al., 2010; Fredriksson et al., 2007, 2003b; M. Shainee et al., 2013). When using Morison equation (Morison et al., 1950) to predict forces and deformation over nets, a crucial point is the selection of C_d values to determine the viscous drag portion of the force . Nowadays, the formulation by DeCew et al. (2010) which describes C_d as a function of *Re* is widely used. However, this model tends to over predict the loads at high current speeds where deformation of the net is significant. Experimental results have emphasized the urge to include shielding effect into numerical models (Kristiansen and Faltinsen, 2015). The reduction of fluid velocity due to the presence of the net can reach up to a 20 % of the incoming velocity depending on the S_n of the net, according to laboratory data using plane net panels (Bi et al., 2013). This reduction is even larger when multiple cages are installed in array form. Once installed, biofouling on nets leads to an increase on S_n and a larger blockage of the flow.

Laboratory and field measurements confirm this phenomenon and its relation with a drastic increase in drag force (Lader et al., 2015; Swift et al., 2006) and volume reduction on the cage (DeCew et al., 2013). Numerical application of shielding effect has been limited due to its complexity. Efforts range from a simple reduction of velocity over the downstream panel (Lader and Enerhaug, 2005) to the latest inclusion of wake models suitable for riser arrays (Endresen et al., 2013) and variations of those models (Cifuentes and Kim, 2015a, 2014). These models still show some deviations from experimental data under high currents and large deformations. Under these conditions, a flexible net pen shows a substantial volume reduction. In this condition, a significant blockage of the fluid flow leads to a reduction of the drag force when compared to the same cage at undeformed conditions (Kristiansen et al., 2015). This is mainly due to the deflection of the flow below and around the cage (Gansel et al., 2012). This blockage is even more significant for nets with high solidity ratios which experience changes on the direction of the flow even at mild current speeds (Moe-Føre et al., 2014). Most of the previously described research has been focused on current loading since viscous drag load significantly adds to the total force over net structures (Kristiansen and Faltinsen, 2015). In reality, for an offshore location there will always be a combination of waves and current. Hence, the analysis of wave loading plays a relevant role on the hydrodynamic analysis of cages. Even more relevant is the interaction between current and wave loading since the order of magnitude can be similar depending on current speed and wave steepness. It is important to mention that wind loads are not considered in the analysis of fish farms since the surface collar does not have a significant portion of

its structure exposed to the elements, thus wind loading does not influence the response of the system.

For the prediction of the hydrodynamic response of cages under multiple load scenarios, numerical models present significant advantages when compared to experiments. Numerical simulations can be run for multiple environmental scenarios in a relatively short period of time. Numerical models are able to determine load levels and predict failure due to overload of components or fatigue. Existing numerical tools are based on a Morison element model (Bi et al., 2014a; Cifuentes and Kim, 2015a; Moe-Føre et al., 2014), consistent finite element (Tsukrov et al., 2002) and screen model (Kristiansen and Faltinsen, 2012; Lader and Fredheim, 2006). These methods have been validated against experiments, considering current and wave loading. As for wave loading, most studies consider a highly stiff surface collar using constant values for inertia and drag coefficients. This does not correspond to the highly flexible nature of HDPE pipes, consequently, careful analysis of the modeling of the surface collar must be taken into account in the numerical approach, given that the load over the floater has a great influence on the total load and motions of the cage under wave conditions (Kristiansen and Faltinsen, 2015).

At the same time, few studies consider wave current interaction for irregular seas. Therefore, it is of relevance to find a rational method to select drag and inertia coefficients for netting and collar under irregular sea states. Under irregular wave loading, a cage using a rigid collar will follow the wave elevation at low wave frequencies. Further, a linear relation can be seen between wave elevation, mooring line

tension, surge and heave motion for frequencies up to 1.0 Hz (Dong et al., 2010). For high wave frequencies, negligible motion is observed and high damping is present in the system (Xu et al., 2011). Under wave loading, studies regarding the dynamic response of the floating collar have shown the relevant effect of the flexural modes over the global response of the cage (Endresen, 2011; Faltinsen et al., 2011). For the whole cage system, mooring line forces are strongly dependent on wave elevation, while volume reduction is driven by current loading. As for the surface collar, large deformations are expected due to the low bending stiffness of the HDPE material typically used (Li et al., 2013a). Another component of the response of the floating collar is the variable buoyancy force due to the constant piercing of the floater on the water surface (Li et al., 2013b). Modeling of bending and axial stiffness of floater and netting, in addition to the approximation of wave kinematics up to the instantaneous free surface are critical, given the significant effect of these parameters on the tension force on mooring lines (Kristiansen and Faltinsen, 2015). Under experimental conditions, most of the analyses have been conducted considering open cages. Top and bottom of the cage are open in order to simplify the model and do not induce further uncertainties into the results. This is particularly important when laboratory data is used as calibration for numerical codes. Recently new studies including more complex cage configuration, including a closed bottom, have shown the complexity of the deformation of the net and how contact between the netting and mooring elements could potentially cause failure in high current and wave conditions (Kristiansen et al., 2015).

Another aspect of the analysis of nets and cages is the flow pattern inside and around the system. Most of the analyses are focused on the determination of forces, which can be done using structural principles; however, when considering multiple cages it is interesting to know the behavior of the flow, as it goes through the net, in order to define the optimal separation between cages. Numerically this can be done using Computational Fluid Dynamics (CFD) techniques describing the net as a porous media. This approach relies on experimental data to find the resistance coefficients. This procedure has revealed that for net panels without including deformation, parameters such as flow angle of attack, net geometry and distance between panels highly influence the total drag load (Patursson et al., 2010; Zhao et al., 2013). CFD results reveal the acceleration of the flow below the net panel due to conservation of mass on the flow field. An even more complex model using fluid structure interaction was developed by Bi et al. (2014b) showing that current speed is reduced up to 8% inside a cage and this reduction can reach up to 47% on the fourth cage on an inline configuration. Turner and Reid (2015) experimentally studied the wake behind an array of cages and found that for close proximity between cages, the array behaves as a single body being the upstream cages the one taking most of the current loading. In addition, their study shows that an even greater reduction of velocity can be found inside a cage when the production netting is surrounded by the predator net which significantly increases blockage effect.

In traditional fish farms installed in protected areas, the mooring system of the cage array and the feeder platform are independent. This allows increasing the safety factor of the system since the load from the platform is not transferred to the cage

mooring lines. On the other hand, in harvesting operations in coastal areas and in daily operations of offshore fish farms, a vessel or platform will share the mooring system and the entire system mooring/platform/cage will be coupled in terms of hydrodynamic response. Under such a case, the coupled response of the system must be calculated to determine loads on mooring and umbilical lines as well as to predict the motions of the platform and cage. A first approach to this coupled problem was numerically performed by Jia et al. (2012) using the interaction of a well boat and a cage during harvesting operations. The reduction of wave elevation due to the presence of the well boat was analyzed and its effect over the Froude Krylov forces and hydrodynamic coefficients for the surface collar were obtained showing small changes compared to an isolated cage. The model used in this analysis applied a static force to represent the effect of the net and a rigid surface collar, thus its results are only valid for small wave amplitudes and weak currents. More complete analyses have been performed as a part of the work performed during the completion of this PhD program by the author considering a single cage installed in 6000 ft. water depth and anchored to the seabed by a single line. Irregular waves and following current are applied over a cylindrical cage with a flexible upper collar. The effect of location of the cage over the water column reveals the advantages of placing the cage under water, even under normal operational conditions in terms of mooring tension levels (Cifuentes et al., 2014). A similar research shows the significant effect of net selection on the tension loads on the different components of the mooring system; in addition to the response of the cage itself under strong shear currents (Cifuentes and Kim, 2015b). A similar system as the one described in the two last

references, was installed and successfully operated from November 2013 to September 2014 6 miles offshore Kona, Hawaii, the system is presented in Figure 1.4. This fish farm showed similar motions of the cage/platform as the ones predicted in the numerical calculations. In this exposed location, survival rate of fish was close to 98% .These facts are the primary sources of motivation for further investigation of the full interaction between cages and platforms, since offshore aquaculture proves to be a feasible alternative to increase fish production to supply the constant demand.

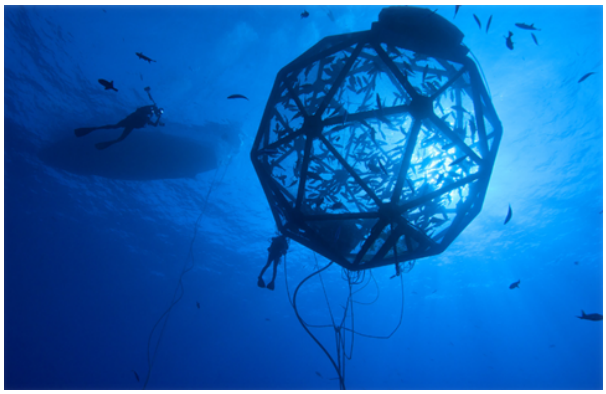

Figure 1.4 Offshore fish farm (Courtesy of http://www.kampachifarm.com/)

1.2 Objective and scope

The final goal of this research is to develop a computationally efficient and robust methodology to describe the forces and deformations of flexible cages and to investigate the coupled response of a fish farm including mooring/platform/cage interaction under irregular waves and following current.

In order to achieve the previous objectives, several steps need to be taken since the final system considers the response of a vessel and a flexible structure. As for the cage, a Morison force model will be used to describe forces on the netting and surface/bottom collar of the cage. The analyses of the cage will be carried out using the commercial software OrcaFlex *v9.6* as the main solver.

Several studies using a similar force model show a lack of accuracy when compared to experimental data for high current speed and high S_n values (Moe-Føre et al., 2015). Under these conditions, reduction of fluid velocity inside the cage plays a significant role and needs to be accounted for in a numerical tool. A complete analysis of the effect of flow velocity reduction inside the net is carried out using wake models developed for riser interaction. By the use of these models it is expected to increase the level of accuracy of calculations involving drag force and deformation of highly flexible cages. This part of the analysis is tested against the experimental and numerical results presented by Lader and Enerhaug (2005).

In addition, when net elements are subjected to different current velocities, the determination of drag coefficient must be time dependent. A variable formulation for C_d will be included into the calculations in order to be able to obtain precise values according to each flow condition.

At high deformations of a net, flow is blocked by the presence of the net and instead of flowing throughout the net; it is deflected to go around and below the cage. Under these conditions, the cage acts similar to a solid body and the drag force versus velocity curve changes its slope at a low rate for experimental measurements while for

numerical models the slope stay almost constant. To account for blockage effects at high current speed and solidity ratios of the net, the determination of C_d values must consider not only flow regime, but net geometry as well based on S_n values. A new formulation for drag coefficient values is derived in this work, implemented in OrcaFlex and later validated against published experimental data.

After the validation of the numerical methodology using steady current is complete, a validation using waves and current is carried out. Previously, most research has considered a stiff surface collar e.g. (Xu et al., 2013); nevertheless, a surface collar withstand most of wave loading and its deformation significantly changes mooring line tension records. Thus, an accurate numerical description of the floater bending stiffness, drag an inertia forces is carried out and the results compared to recently publish experimental data. Since linear wave theory is used when modelling different sea states, wave kinematics above mean water level need to be accounted for using an approximation method. For large mass offshore platforms, the differences between extrapolation models do not induce large differences on the loads. On the other hand, there is no evidence whether the selection of a particular method will increase the accuracy of the calculations when motions and forces over a cage are analyzed. This is another important topic in the present work where three models for extension of wave kinematics above mean water level are studied leading to the conclusion that Wheeler stretching technique proves to be the adequate model when calculating mooring line tension on flexible cages. Additionally, a rational method for the selection of drag and

inertia coefficients under irregular waves and following currents is proposed considering a realistic bending stiffness, including shielding and blockage effect.

Once the numerical model for the cage is completely validated, the coupled response of the vessel and cage is studied. In the present study, an offshore fish farm is modeled in OrcaFlex including mooring lines, feeder vessel and a single cage. This model is based on a real installation allowing a qualitative comparison of the performance of the numerical model. Net selection and position of the cage over the water column will be analyzed. Several complex load scenarios including storm and survival conditions are studied. This is the first analysis of this kind corresponding to the first fish farm installed in deep water (6000 ft.).

The full interaction, translated into forces and motions of platform, cage and connecting elements is expected to be analyzed, finding useful information for the future developments of the offshore aquaculture industry.

In addition, an analysis of a new concept, a Submerged Floating Tunnel (SFT) is included to show further applications of the analysis of slender members under wave loading. This analysis helps to evaluate the relevance of the application of variable drag coefficient values on slender members. Further, the analysis of a SFT compares the results of OrcaFlex and CHARM3D helping to validate the mooring line solver in both codes. Tension on mooring lines and motion of a submerged body are obtained and successfully compared to experimental data. This is one of the few numerical analyses in a concept that could potentially benefit areas with fjords and straits to improve connectivity.

2. LOADS ON FLOATING PLATFORMS AND NET STRUCTURES

2.1 Introduction

Since two different numerical tools are used in the present work, its fundamentals will be separately presented. First an overview of first order wave theory is included since this is the base of the calculations of forces on platforms when exposed to irregular waves. Later the theory of wave loads over floating platforms is summarized including diffraction and radiation problems. Then, the description of the numerical definition of the elements used in OrcaFlex to model a cage is included with emphasis on the structural and hydrodynamic force model. In addition, a description of the numerical scheme used to solve the equation of motion is presented. In order to include viscous effects on the platform, the description of Morison's formula applications is included.

2.2 Wave theory formulation

In order to calculate forces and motion of floating platforms, diffraction and radiation theory needs to be revised. The first step is to review wave theory to follow with the determination of forces and moments on floating platforms.

As described by Faltinsen (1993), the flow is assumed to be incompressible, inviscid and irrotational. A convenient manner to mathematically represent the fluid velocity vector $\boldsymbol{V}(x,y,z,t) = (u,v,w)$ at time t at a particular point $\boldsymbol{x} = (x,y,z)$ is by the concept of velocity potential Φ. Velocity and potential are correlated by the gradient of Φ.

$$V = \nabla \Phi \equiv i\frac{\partial \Phi}{\partial x} + j\frac{\partial \Phi}{\partial y} + k\frac{\partial \Phi}{\partial z} \tag{2.1}$$

In this expression i, j and k are unit vectors along x, y and z axis. A fluid is irrotational when the vorticity vector $\omega = \nabla \times V$ is zero on the fluid domain. The incompressibility condition means that $\nabla \bullet V = 0$. From the previous conditions it follows that the velocity potential must satisfy Laplace equation.

$$\frac{\partial^2 \Phi}{\partial x^2} + \frac{\partial^2 \Phi}{\partial y^2} + \frac{\partial^2 \Phi}{\partial z^2} = 0 \tag{2.2}$$

To complete this problem, proper boundary conditions need to be defined at the sea surface and seabed. Once these conditions are defined, the Boundary Value Problem (BVP) can be solved.

Boundary conditions include kinematic and dynamic boundary conditions applied at the sea surface while impermeability condition is applied at the seabed. Bottom boundary condition expresses that there is no flow going through the seabed and it is defined as the partial derivate of the potential along the normal direction to the seabed pointing towards the fluid domain.

$$\frac{\partial \Phi}{\partial n} = 0 \tag{2.3}$$

Kinematic free surface boundary condition implies that a fluid particle on the free surface is assumed to stay on the free surface. This is express as:

$$\frac{\partial \eta}{\partial t} + \frac{\partial \Phi}{\partial x}\frac{\partial \eta}{\partial x} + \frac{\partial \Phi}{\partial y}\frac{\partial \eta}{\partial y} - \frac{\partial \Phi}{\partial z} = 0 \qquad on \quad z=\eta(x,y,t) \tag{2.4}$$

In this expression, $\eta(x,y,t)$ represents the instantaneous free surface elevation at the position (x,y) at time t. Dynamic free surface boundary condition states that the water pressure is equal to the atmospheric pressure along the free surface.

$$g\eta - \frac{\partial \Phi}{\partial t} + \frac{1}{2}\left(\left(\frac{\partial \Phi}{\partial x}\right)^2 + \left(\frac{\partial \Phi}{\partial y}\right)^2 + \left(\frac{\partial \Phi}{\partial z}\right)^2\right) = 0 \qquad on \qquad z=\eta(x,y,t) \tag{2.5}$$

Solving Laplace equation using the given nonlinear boundary conditions is difficult since we do not have information about the location of the free surface before the problem is solved. In order to obtain a solution, perturbation method is applied, assuming that wave amplitude is small when compared to a characteristic wavelength and body dimension. This can give us an approximate solution that is presented up to second order accuracy in this work. Using Taylor expansion, free surface conditions can be transferred form the instantaneous free surface to the mean water level at which $z=0$. Only linear terms are kept.

$$\frac{\partial \eta^{(1)}}{\partial t} = \frac{\partial \Phi^{(1)}}{\partial z} \qquad on \quad z=0 \tag{2.6}$$

$$g\eta^{(1)} - \frac{\partial \Phi^{(1)}}{\partial t} = 0 \qquad on \qquad z=0 \tag{2.7}$$

The solution is now in the form of the first and second order velocity potential and free surface elevation.

$$\Phi^{(1)} = Re\left[-\frac{igA}{\omega}\frac{\cosh k(z+d)}{\cosh kd} e^{i(kx\cos\theta + ky\sin\theta - \omega t)}\right] \tag{2.8}$$

$$\eta^{(1)} = A\cos(kx\cos\theta + ky\sin\theta - \omega t) \tag{2.9}$$

By combining the linear free surface boundary conditions we have.

$$\frac{\partial^2 \Phi^{(1)}}{\partial t^2} + g\frac{\partial \Phi^{(1)}}{\partial z} = 0 \qquad on \quad z=0 \tag{2.10}$$

If we substitute $\Phi^{(1)}$ on the combined free surface boundary condition, we obtain the linear dispersion relationship which relates wave period with wave length and water depth.

$$\omega^2 = gk\tanh(kd) \tag{2.11}$$

The water particle velocities are obtain by taking the spatial derivative of $\Phi^{(1)}$

$$\begin{aligned} u(t,x,z) &= \frac{\partial \Phi^{(1)}}{\partial x} = \mathrm{Re}\left[\frac{gkA}{\omega}\frac{\cosh k(z+d)}{\cosh kd} e^{i(kx-\omega t+\varepsilon)}\cos\theta\right] \\ v(t,x,z) &= \frac{\partial \Phi^{(1)}}{\partial y} = \mathrm{Re}\left[\frac{gkA}{\omega}\frac{\cosh k(z+d)}{\cosh kd} e^{i(kx-\omega t+\varepsilon)}\sin\theta\right] \\ w(t,x,z) &= \frac{\partial \Phi^{(1)}}{\partial z} = \mathrm{Re}\left[\frac{-igkA}{\omega}\frac{\sinh k(z+d)}{\cosh kd} e^{i(kx-\omega t+\varepsilon)}\right] \end{aligned} \tag{2.12}$$

As for accelerations, these are obtained by taking derivatives of velocity with respect to time neglecting high order convective terms

$$\begin{aligned} \dot{u}(t,x,z) &\approx \frac{\partial u}{\partial t} = \mathrm{Re}\left[-igkA\frac{\cosh k(z+d)}{\cosh kd} e^{i(kx-\omega t+\varepsilon)}\cos\theta\right] \\ \dot{v}(t,x,z) &\approx \frac{\partial v}{\partial t} = \mathrm{Re}\left[-igkA\frac{\cosh k(z+d)}{\cosh kd} e^{i(kx-\omega t+\varepsilon)}\sin\theta\right] \\ \dot{w}(t,x,z) &\approx \frac{\partial w}{\partial t} = \mathrm{Re}\left[gkA\frac{\sinh k(z+d)}{\cosh kd} e^{i(kx-\omega t+\varepsilon)}\right] \end{aligned} \tag{2.13}$$

The above wave kinematics are especially useful when calculating forces in slender structures exposed to waves such as the surface collar. Wave kinematics are used to determine C_d and C_M coefficients in Morison equation.

The second order velocity potential and free surface elevation is given by.

$$\Phi^{(2)}=Re\left[-\frac{3}{8}\omega A^2\frac{\cosh 2k(z+d)}{\sinh^4 kd}e^{i(2kx\cos\theta+2ky\sin\theta-2\omega t)}\right] \tag{2.14}$$

$$\eta^{(2)}=A^2\frac{\cosh kd}{\sinh^3 kd}cos(2kx\cos\theta+2ky\sin\theta-2\omega t) \tag{2.15}$$

In the previous expressions A represents wave amplitude, $\omega=2\pi/T$ wave frequency in radians per second, T wave period, $k=2\pi/\lambda$ wave number with λ being wave length, d is water depth, g acceleration of gravity and θ incident wave heading angle.

To represent an irregular wave field, linear theory can be used by representing the sea surface elevation as the sum of a large number of individual wave components N with different amplitudes and random phase angles ε_i distributed between 0 and 2π.

$$\eta(x,t)=\sum_{i=1}^{N}A_i\cos(k_i x+\omega_i t+\varepsilon_i) \tag{2.16}$$

Wave amplitudes can also be represented by a wave spectrum $S(\omega)$ from which the most commons are JONSWAP (Joint North Sea Wave Observation Project) and Pierson-Moskowitz. A wave spectrum is related to wave amplitudes as follows considering intervals of frequency $\Delta\omega$.

$$\frac{1}{2}A_i^2=S(\omega_i)\Delta\omega \tag{2.17}$$

When using a finite number of wave components, repetition of wave elevation time series is likely. To avoid this phenomenon, minor modifications to the sea surface elevation can be made as shown below.

$$\eta(x,t) = \mathrm{Re}\left[\sum_{i=1}^{N} A_i e^{i(k_i x - \omega_i^{'} + \varepsilon_i)}\right] \tag{2.18}$$

where $\omega_i^{'} = \omega_i + \delta\omega_i$ and $\delta\omega_i$ is a random perturbation number uniformly distributed between $-\Delta\omega/2$ and $\Delta\omega/2$.

The following figure is included to better understand the relation between time and frequency domain representation *S(ω)* of water waves.

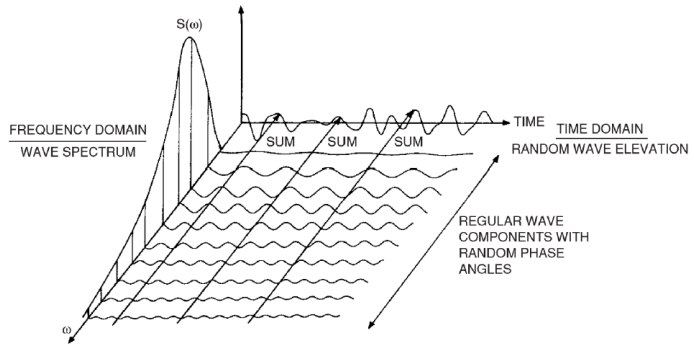

Figure 2.1 Time and frequency domain representation of waves (Faltinsen, 1993)

2.3 Wave loads on floating structures

Once the numerical description of waves in the ocean environment is complete, the determination of forces and motion of a floating platform under such conditions is presented. When a large volume structure is included in the fluid domain, the wave field is disturbed by the platform. In addition to the incident wave field, waves diffracted by the presence of the platform are generated as well as radiated waves due to the wave induced motion of the platform. In case of slender bodies, where the characteristic length

is small compared to wave length, forces can be computed using Morison equation (Haritos and He, 1992). The same method is applied to account for viscous loads over the platform when current loading is applied. Diffraction/radiation theory is described in the following section.

2.3.1 Diffraction/Radiation theory

Diffraction forces are defined as forces over the platform when its motion is restrained in the presence of an incident wave field. On the other hand, radiation forces are those generated when the platform is externally excited and there is not incident waves in the fluid domain. Radiation forces include added mass, restoring force and radiation damping. To solve these forces, potentials for each component are defined. The total velocity potential Φ_T is now composed of incident potential Φ_I, diffraction potential Φ_D, and radiation potential Φ_R. Total potential can be expressed as a perturbation series depending on wave slope parameter ε.

$$\Phi_T = \sum_{n=1}^{\infty} \varepsilon^{(n)} \Phi^{(n)} = \sum_{n=1}^{\infty} \varepsilon^{(n)} [\Phi_I^{(n)} + \Phi_D^{(n)} + \Phi_R^{(n)}] \tag{2.19}$$

where $\Phi^{(n)}$ represents the nth order solution for Φ. In the present study, solutions up to first order are considered.

As before, to solve the BVP, boundary conditions need to be applied. In the present case a body surface boundary condition is defined which states that the fluid has the same velocity as the floating body on the normal direction to the body surface.

$$\frac{\partial \Phi_T}{\partial n} = V_n \tag{2.20}$$

where n is defined as the normal vector to the body surface and V_n is the normal velocity vector of the platform at its surface.

Both diffraction Φ_D, and radiation potential Φ_R must satisfy the Sommerfeld radiation condition which implies that both potential vanish at a large radial distance r from the body.

$$\lim_{r\to\infty} \sqrt{r}\left(\frac{\partial \Phi_{D,R}}{\partial r}\right) \pm ik\Phi_{D,R} = 0 \tag{2.21}$$

Once boundary conditions are defined, the solutions for first order are presented.

2.3.2 First order boundary value problem

The solution to the previous problem up to first order for the interaction between a freely floating platform and monochromatic waves is presented in this section. First, the first order total potential Φ_T is written separating its temporal and spatial dependency.

$$\begin{aligned} \Phi_T^{(1)} &= \varepsilon[\Phi_I^{(1)} + \Phi_D^{(1)} + \Phi_R^{(1)}] \\ \Phi_T^{(1)} &= \mathrm{Re}\left\{[\phi_I^{(1)}(x,y,z) + \phi_D^{(1)}(x,y,z) + \phi_R^{(1)}(x,y,z)]e^{-i\omega t}\right\} \end{aligned} \tag{2.22}$$

Rewriting the first order incident potential $\phi_I^{(1)}$ as

$$\phi_I^{(1)} = Re\left[-\frac{igA}{\omega}\frac{\cosh k(z+d)}{\cosh kd}e^{i\mathbf{k}\bullet\mathbf{x}}\right] \tag{2.23}$$

where $\boldsymbol{k}$ is the wave number vector defined as $(k\cos\theta, k\sin\theta, 0)$ and $\boldsymbol{x}$ is the position vector on the fluid, while θ represents the angle between the incident wave field and the positive x axis on the fluid domain.

For the first order diffraction and radiation potential boundary value problem, the following boundary conditions apply.

$$\nabla^2\phi_{D,R}^{(1)}=0 \qquad \text{in the fluid } (z<0) \tag{2.24}$$

$$\left(-\omega^2+g\frac{\partial}{\partial z}\right)\phi_{D,R}^{(1)}=0 \qquad \text{on the free surface } (z=0) \tag{2.25}$$

$$\frac{\partial\phi_{D,R}^{(1)}}{\partial z}=0 \qquad \text{on the bottom } (z=d) \tag{2.26}$$

$$\frac{\partial\phi_{R}^{(1)}}{\partial n}=-i\omega\boldsymbol{n}\bullet(\boldsymbol{\xi}^{(1)}+\boldsymbol{\alpha}\times\boldsymbol{r}) \qquad \text{on the body surface} \tag{2.27}$$

$$\lim_{r\to\infty}\sqrt{r}\left(\frac{\partial}{\partial r}\pm ik\right)\phi_{D,R}^{(1)}=0 \qquad \text{at far field} \tag{2.28}$$

In the previous boundary conditions $\boldsymbol{r}$ represents the position vector on the surface of the body, r is the radial distance from the origin ($r^2=x^2+y^2$) while $\boldsymbol{n}$ is the outward unit normal vector on the body surface of the platform. Translational $\left(\Xi^{(1)}\right)$ and rotational $\left(\Theta^{(1)}\right)$ motions of the platform up to first order are defined as follows.

$$\Xi^{(1)}=\mathrm{Re}\left\{\boldsymbol{\xi}^{(1)}e^{-i\omega t}\right\} \qquad \boldsymbol{\xi}^{(1)}=\left\{\xi_1^{(1)},\xi_2^{(1)},\xi_3^{(1)}\right\} \tag{2.29}$$

$$\Theta^{(1)}=\mathrm{Re}\left\{\boldsymbol{\alpha}^{(1)}e^{-i\omega t}\right\} \qquad \boldsymbol{\alpha}^{(1)}=\left\{\alpha_1^{(1)},\alpha_2^{(1)},\alpha_3^{(1)}\right\} \tag{2.30}$$

Subscripts 1, 2 and 3 denote surge, sway and heave translational motion, while for rotational motion subscripts represent roll, pitch and yaw. Translational and rotational motion are referred to *x*, *y* and *z* axis respectably. Further simplification of notation for the first order six degree of freedom motions is carried out.

$$\zeta_i = \xi_i^{(1)} \qquad \text{for } i = 1,2,3 \tag{2.31}$$

$$\zeta_i = \alpha_{i-3}^{(1)} \qquad \text{for } i = 4,5,6 \tag{2.32}$$

Using the previous concepts for motion, the radiation potential $\phi_R^{(1)}$ can be define as follows.

$$\phi_R^{(1)} = \sum_{i=1}^{6} \zeta_i \phi_i^{(1)} \tag{2.33}$$

where $\phi_i^{(1)}$ represents the first order velocity potential of the rigid body motion with unit amplitude in the i^{th} mode ,under no presence of incident waves. A solution is found when the free surface, bottom, far field and body boundary conditions are satisfied. Body boundary conditions on the body surface S_B are defined in the next expressions.

$$\frac{\partial \phi_i^{(1)}}{\partial n} = n_i \qquad i = 1,2,3 \tag{2.34}$$

$$\frac{\partial \phi_i^{(1)}}{\partial n} = (\boldsymbol{r} \times \boldsymbol{n})_{i-3} \qquad i = 1,2,3 \tag{2.35}$$

Similarly, for the first order diffraction potential $\phi_D^{(1)}$, a new body surface boundary condition is defined in order to find the velocity potential.

$$\frac{\partial \phi_D^{(1)}}{\partial n} = -\frac{\partial \phi_I^{(1)}}{\partial n} \qquad i = 1,2,3 \tag{2.36}$$

Once all the components of the first order problem are defined, the calculation of forces can be computed.

2.3.3 First order potential forces

Once diffraction $\phi_D^{(1)}$ and radiation $\phi_R^{(1)}$ potentials have been solved, forces over the floating platform can be obtained as well as the free surface elevation. By following the perturbation method, we can express hydrodynamic pressure *P(t)* and free surface elevation *η(t)* up to first order as follows.

$$P^{(1)} = -\rho \frac{\partial \Phi_T^{(1)}}{\partial t} \tag{2.37}$$

$$\eta^{(1)} = -\frac{1}{g}\frac{\partial \Phi_T^{(1)}}{\partial t} \qquad \text{at } z = 0 \tag{2.38}$$

Once pressure is solved, the forces and moments over the platform can be directly obtained by integrating the pressure over the instantaneous wetted surface of the body *S(t)*.

$$F(t)_i = \begin{cases} \iint_{S_B} P n_i dS & i = 1,2,3 \\ \iint_{S_B} P(\boldsymbol{r} \times \boldsymbol{n})_i dS & i = 4,5,6 \end{cases} \tag{2.39}$$

The total first order force can be defined as the sum of its different components.

$$\boldsymbol{F}^{(1)} = \boldsymbol{F}_{HS}^{(1)} + \boldsymbol{F}_R^{(1)} + \boldsymbol{F}_{EX}^{(1)} \tag{2.40}$$

In this expression, subscripts *HS* stands for hydrostatic force and moment, *R* represents force and moment contributions from the radiation potential while *EX* represents wave exciting forces from incident and diffraction wave potentials.

Each component is now fully described. First, hydrostatic restoring forces and moment $\boldsymbol{F}_{HS}^{(1)}$ are generated due to pressure changes induced by motions of the body and can be defined as follows.

$$\boldsymbol{F}_{HS}^{(1)} = -\left[\boldsymbol{K}\right]\left\{\boldsymbol{\xi}^{(1)}\right\} \tag{2.41}$$

where $\boldsymbol{\xi}^{(1)}$ is the first order motion of the body and $\boldsymbol{K}$ represents the hydrostatic restoring stiffness matrix which components are defined as:

$$\begin{aligned}
&K_{33} = \rho g A_w \\
&K_{34} = \rho g A_w y_f \\
&K_{35} = -\rho g A_w x_f \\
&K_{44} = \rho g (S_{22} + \forall z_b) - mgz_g \\
&K_{45} = -\rho g S_{12} \\
&K_{46} = -\rho g \forall x_b + mgx_g \\
&K_{55} = \rho g (S_{11} + \forall z_b) - mgz_g \\
&K_{56} = -\rho g \forall y_b + mgy_g \\
&Otherwise\ K_{ij} = 0
\end{aligned} \tag{2.42}$$

where A_w represented water plane area, (x_f, y_f) is the coordinate of the center of flotation of the body in the horizontal plane, (x_b, y_b, z_b) represents the location of the center of buoyancy and (x_g, y_g, z_g) represents the position of the center of gravity of the platform and

$$S_{11} = \iint_{S_B} x^2 dS$$
$$S_{22} = \iint_{S_B} y^2 dS \tag{2.43}$$
$$S_{12} = \iint_{S_B} xy dS$$

The second component on the total first order force comes from the radiation force $\boldsymbol{F}_R^{(1)}$. This includes added mass and radiation damping which are generated due to the outgoing waves formed by the forced first order motion of the floating body. $\boldsymbol{F}_R^{(1)}$ can be defined as follows.

$$\boldsymbol{F}_R^{(1)} = \mathrm{Re}\left(\left[\boldsymbol{f}\right]\left\{\boldsymbol{\xi}^{(1)}\right\}\right) \tag{2.44}$$

where

$$\boldsymbol{f} = f_{ij} = -\rho \iint_{S_B} \frac{\partial \phi_i}{\partial n} \phi_j dS \qquad i, j = 1, 2, ..., 6 \tag{2.45}$$

The coefficients f_{ij} are complex being the real and imaginary parts dependent on the exciting frequency ω. Thus, coefficients take the form.

$$f_{ij} = -\omega^2 M_{ij}^a - i\omega C_{ij} \tag{2.46}$$

Finally, force and moment from radiation potential can be expressed in terms of added mass and radiation damping as follows.

$$\boldsymbol{F}_R^{(1)} = \mathrm{Re}\left(\left[\boldsymbol{M}^a\right]\left\{\ddot{\boldsymbol{\xi}}^{(1)}\right\} + \left[\boldsymbol{C}\right]\left\{\dot{\boldsymbol{\xi}}^{(1)}\right\}\right) \tag{2.47}$$

where $\boldsymbol{M}^a$ and $\boldsymbol{C}$ are the added mass and radiation damping matrices.

The last component in the calculation of the total first order forces are external forces and moments $\boldsymbol{F}_{EX}^{(1)}$ which represent first order wave exciting components due to the incident and diffraction wave potentials.

$$\boldsymbol{F}_{EX}^{(1)} = \mathrm{Re}\left\{-\rho A e^{-i\omega t}\iint_{S_B}(\phi_I + \phi_D)\frac{\partial \phi_j}{\partial n}dS\right\} \qquad j = 1,2,...,6 \tag{2.48}$$

First order wave exciting forces are linearly dependent on wave amplitude A which is frequency dependent. A convenient method to define first order wave components is the Linear Transfer Function (*LTF*) which relates the exciting force to a unit amplitude incident wave ($LTF = \boldsymbol{F}_{EX}^{(1)} / A$).

2.3.4 Wave loads in time domain

In previous sections, wave forces were obtained based on potential theory. Linear wave forces are calculated at a specific frequency while second order sum and difference frequency forces are determined based on the interaction of bichromatic waves. In this section an extension of this theory is presented to extend the solution of forces and moments to random waves. First and second order hydrodynamic forces and moment on a body due to a stationary Gaussian random sea can in general be expressed as a two-term Volterra series in time domain.

$$\boldsymbol{F}^{(1)}(t) + \boldsymbol{F}^{(2)}(t) = \int_{-\infty}^{\infty} h_1(\tau)\eta(t-\tau)d\tau + \int_{-\infty}^{\infty}\int_{-\infty}^{\infty} h_2(\tau_1+\tau_2)\eta(t-\tau_1)\eta(t-\tau_2)d\tau_1 d\tau_2 \tag{2.49}$$

where $\eta(t)$ is the ambient free surface condition at the reference point, $h_1(\tau)$ is the linear impulse response function, and $h_2(\tau_1,\tau_2)$ is the quadratic impulse response function. For unidirectional seas using N wave components, the wave exciting forces from incident and diffraction potential can be defined as:

$$\boldsymbol{F}^{(1)}(t) = \mathrm{Re}\left[\sum_{j=1}^{N} A_j \boldsymbol{L}(\omega_j) e^{i\omega_j t}\right] \tag{2.50}$$

$$\boldsymbol{F}^{(2)}(t) = \mathrm{Re}\left[\sum_{j=1}^{N}\sum_{k=1}^{N} A_j A_k^* \boldsymbol{D}(\omega_j, -\omega_k) e^{i(\omega_j-\omega_k)t} + \sum_{j=1}^{N}\sum_{k=1}^{N} A_j A_k \boldsymbol{S}(\omega_j, \omega_k) e^{i(\omega_j+\omega_k)t}\right] \tag{2.51}$$

where (*) represents complex conjugate. $\boldsymbol{L}(\omega_j)$ is the linear force transfer function (*LFT*), $\boldsymbol{D}(\omega_j, -\omega_k)$ and $\boldsymbol{S}(\omega_j, \omega_k)$ are the difference and sum frequency quadratic transfer functions (*QTF*) respectively.

In time domain, radiation forces and moment adopt the following form considering contributions from first and second order motions.

$$\boldsymbol{F}_R(t) = -\boldsymbol{M}^a(\infty)\ddot{\xi}(t) - \int_{-\infty}^{t} \boldsymbol{R}(t-\tau)\dot{\xi}(\tau)d\tau \tag{2.52}$$

where $\boldsymbol{M}^a(\omega)$ represents the added mass at infinite frequency, and $\boldsymbol{R}(t)$ is called retardation function and it is related to the frequency domain solution of the radiation problem as presented.

$$\boldsymbol{R}(t) = \frac{2}{\pi}\int_0^{\infty} C(\omega)\frac{\sin\omega t}{\omega}d\omega \tag{2.53}$$

where $C(\omega)$ is the wave radiation damping coefficient previously defined at frequency ω. As for added mass at infinite frequency this is obtained using the following expression considering $M^a(\omega)$ as added mass at frequency ω.

$$\boldsymbol{M}^a(\infty) = M^a(\omega) - \int_0^\infty \boldsymbol{R}(t)\cos\omega t\, dt \tag{2.54}$$

With all components defined, the total force in time domain can now be defined.

$$\boldsymbol{F}_{Total}(t) = \boldsymbol{F}^{(1)}(t) + \boldsymbol{F}^{(2)}(t) + \boldsymbol{F}_R(t) \tag{2.55}$$

where the first two components represent the total wave exciting force while the third component is the previously defined radiation term.

2.4 Floating body motions in regular waves

Once all forces are calculated, the next step is to obtain the response of the floating body to those forces. External forces such as wave, current and gravitational forces need to be taken into account for a freely floating body. According to Newton's second law, once the sum of all external forces is known, the motion of the body can be calculated. Motions are solved using the conservation of momentum principle which can be represented by the following two expressions.

$$m\frac{d^2\boldsymbol{x}_g}{dt^2} = \boldsymbol{f} \tag{2.56}$$

$$\boldsymbol{I}\frac{d\boldsymbol{\psi}}{dt^2} + \boldsymbol{\psi}\times(\boldsymbol{I}\boldsymbol{\psi}) = \boldsymbol{m} \tag{2.57}$$

where m represents the mass of the body, $\boldsymbol{x}_g$ is the vector of coordinates of the center of gravity of the body, $\boldsymbol{I}$ moment of inertia matrix, $\boldsymbol{\psi}$ angular velocity and $\boldsymbol{m}$, $\boldsymbol{f}$ are the

external moments and forces. In the previous expression, nonlinear terms arise $(\boldsymbol{\psi} \times (\boldsymbol{I}\boldsymbol{\psi}))$; however small rotations of the body are here considered thus the linearized version of these equations can be applied. This is consistent with the assumptions made to determine diffraction forces. Under the small rotation assumption, a single linear equation of motion for the floating body can be defined.

$$\boldsymbol{M}\ddot{\boldsymbol{\zeta}} = \boldsymbol{F}(t) \tag{2.58}$$

where $\ddot{\zeta}$ is the second time derivative of the six degrees of freedom body motion vector $\boldsymbol{\zeta} = (\zeta_1, ..., \zeta_6)$. $\zeta_1, \zeta_2, \zeta_3$ represent linear motions of the platform at origin in *x*, *y*, *z* direction (surge, sway, heave) while $\zeta_4, \zeta_5, \zeta_6$ are the rotational motions along *x*, *y*, *z* directions (roll, pitch, yaw). ***F(t)*** is the vector of external forces including hydrostatic and hydrodynamic forces in addition to contributions from mooring lines. ***M*** is defined as the *6x6* mass matrix defined as follows.

$$\boldsymbol{M} = \begin{Bmatrix} m & 0 & 0 & 0 & mz_g & -my_g \\ 0 & m & 0 & -mz_g & 0 & mx_g \\ 0 & 0 & m & my_g & -mx_g & 0 \\ 0 & -mz_g & my_g & I_{11} & I_{12} & I_{13} \\ mz_g & 0 & -mx_g & I_{21} & I_{22} & I_{23} \\ -my_g & mx_g & 0 & I_{31} & I_{32} & I_{33} \end{Bmatrix} \tag{2.59}$$

In this expression, *(x_g, y_g, z_g)* are the coordinates of the center of gravity of the body. Then moments of inertia are calculated as follows.

$$I_{ij} = \iiint_{V_B} \rho_B \left[\boldsymbol{x} \cdot \boldsymbol{x}\delta_{ij} - x_i x_j \right] dV \tag{2.60}$$

where V_B denotes integration over the body volume, ρ_B is the density of the body and δ_{ij} is the Kronecker delta function.

When nonlinearities in the system are significant, a time domain analysis becomes the best option since no linearization needs to be done as in the case of frequency domain. The equation of motion can be expressed as the summation of contributions as follows.

$$\left[\boldsymbol{M} + \boldsymbol{M}^a(\infty)\right]\ddot{\boldsymbol{\varsigma}} + \boldsymbol{K}\boldsymbol{\varsigma} = \boldsymbol{F}_I(t) + \boldsymbol{F}_C(t,\dot{\boldsymbol{\varsigma}}) + \boldsymbol{F}_n(t,\dot{\boldsymbol{\varsigma}}) \tag{2.61}$$

where radiation force is defined next, in addition to $\boldsymbol{F}_I(t)$ first and second order wave forces previously defined and $\boldsymbol{F}_n(t,\varsigma)$ defined as nonlinear drag from Morison equation which later will be defined.

$$\boldsymbol{F}_C(t,\dot{\boldsymbol{\varsigma}}) = -\int_{-\infty}^{t} \boldsymbol{R}(t-\tau)\dot{\varsigma}\, d\tau \tag{2.62}$$

In order to numerically solve this equation of motion in time domain, the Adams-Moulton method is applied. First, the equation of motion is reduced to a set of two first order differential equations.

$$\bar{\boldsymbol{M}}\dot{\boldsymbol{\xi}} = \boldsymbol{F}_I(t) + \boldsymbol{F}_C(t,\dot{\boldsymbol{\varsigma}}) + \boldsymbol{F}_n(t,\dot{\boldsymbol{\varsigma}}) - \boldsymbol{K}\boldsymbol{\varsigma} \tag{2.63}$$

$$\dot{\boldsymbol{\varsigma}} = \boldsymbol{\xi} \tag{2.64}$$

where $\bar{\boldsymbol{M}} = \boldsymbol{M} + \boldsymbol{M}^a(\infty)$

After integrating the previous equation from time step $t^{(n)}$ to $t^{(n+1)}$ we have:

$$\bar{\boldsymbol{M}}\boldsymbol{\xi}^{(n+1)} = \bar{\boldsymbol{M}}\boldsymbol{\xi}^{(n)} + \int_{t^{(n)}}^{t^{(n+1)}} (\boldsymbol{F}_I + \boldsymbol{F}_C + \boldsymbol{F}_n)dt + \int_{t^{(n)}}^{t^{(n+1)}} -\boldsymbol{K}\boldsymbol{\varsigma}\, dt \tag{2.65}$$

$$\varsigma^{(n+1)} = \varsigma^{(n)} + \int_{t^{(n)}}^{t^{(n+1)}} \xi dt \tag{2.66}$$

Applying the Adams-Moulton scheme and rearranging the equations we have

$$\int_{t^{(n)}}^{t^{(n+1)}} x dt = \frac{\Delta t}{2}\left[x^{(n)} + x^{(n+1)}\right] \tag{2.67}$$

$$\begin{aligned}\bar{\boldsymbol{M}}\boldsymbol{\xi}^{(n+1)} = \bar{\boldsymbol{M}}\boldsymbol{\xi}^{(n)} &+ \frac{\Delta t}{2}\left(\boldsymbol{F}_I^{(n+1)} + \boldsymbol{F}_I^{(n)} + \boldsymbol{F}_C^{(n+1)} + \boldsymbol{F}_C^{(n)} + \boldsymbol{F}_n^{(n+1)} + \boldsymbol{F}_n^{(n)}\right) \\ &- \frac{\Delta t}{2}\boldsymbol{K}\left(\boldsymbol{\varsigma}^{(n+1)} + \boldsymbol{\varsigma}^{(n)}\right)\end{aligned} \tag{2.68}$$

$$\boldsymbol{\xi}^{(n+1)} = \frac{2}{\Delta t}\left(\boldsymbol{\varsigma}^{(n+1)} - \boldsymbol{\varsigma}^{(n)}\right) - \boldsymbol{\xi}^{(n)} \tag{2.69}$$

These last linear algebraic equations with unknowns $\boldsymbol{\xi}^{(n+1)}$ and $\boldsymbol{\varsigma}^{(n+1)}$ can be solved using an iterative process due to the dependency of the convolution and drag load on unknown velocity at time (*n+1*). To solve for $\boldsymbol{F}_C^{(n+1)}$ and $\boldsymbol{F}_n^{(n+1)}$ an initial guess for $\boldsymbol{\xi}^{(n+1)}$ is required. This iteration can be avoided by using the Adam-Bashforth scheme on the following nonlinear terms.

$$\int_{t^{(n)}}^{t^{(n+1)}} \boldsymbol{F}_C dt = \frac{\Delta t}{2}\left(3\boldsymbol{F}_C^{(n)} - \boldsymbol{F}_C^{(n-1)}\right) \qquad \text{and } = \Delta t \boldsymbol{F}_C^{(0)} \text{ for } n = 0 \tag{2.70}$$

$$\int_{t^{(n)}}^{t^{(n+1)}} \boldsymbol{F}_n dt = \frac{\Delta t}{2}\left(3\boldsymbol{F}_n^{(n)} - \boldsymbol{F}_n^{(n-1)}\right) \qquad \text{and } = \Delta t \boldsymbol{F}_n^{(0)} \text{ for } n = 0 \tag{2.71}$$

Combining the previous expressions we arrive at the final equation of motion of the platform.

$$\left[\frac{4}{\Delta t^2}\bar{\boldsymbol{M}}+\boldsymbol{K}\right]\Delta\boldsymbol{\varsigma}=\frac{4}{\Delta t}\bar{\boldsymbol{M}}\dot{\boldsymbol{\xi}}^{(n)}+\left(\boldsymbol{F}_I^{(n+1)}+\boldsymbol{F}_I^{(n)}\right)+\left(3\boldsymbol{F}_C^{(n)}-\boldsymbol{F}_C^{(n-1)}\right)+\left(3\boldsymbol{F}_n^{(n)}-\boldsymbol{F}_n^{(n-1)}\right)-2\boldsymbol{K}\boldsymbol{\varsigma}^{(n)}+2\boldsymbol{F}_o \tag{2.72}$$

$$\Delta\boldsymbol{\varsigma}=\boldsymbol{\varsigma}^{(n+1)}-\boldsymbol{\varsigma}^{(n)} \tag{2.73}$$

$\boldsymbol{F}_o$ represents a constant force such a net buoyancy to balance mooring payloads. Numerical instability when applying the Adam-Bashford scheme could arise leading to large numerical errors. To avoid errors and assure accuracy on the results, a small time step must be selected. Considering that the platform is connected to mooring lines where strong nonlinearities require even smaller time steps when compared to the platform motions, mooring line analysis drives the selection of Δt.

2.5 Line and buoy theory in OrcaFlex

In OrcaFlex, net, mooring lines and surface/bottom collars are modeled by using line elements joint together by either six or three degree of freedom buoys. Three degree of freedom buoys are used to connect the elements representing the net where bending stiffness is negligible. For the floating and bottom collars lines are connected using six degree of freedom buoys since bending stiffness plays an important role in the determination of mooring line forces when exposed to wave loading.

2.5.1 OrcaFlex line theory

In OrcaFlex lines are discretize in terms of massless segments connected by nodes located at each end. Segments represent axial and torsional properties of the line

while other properties such as mass, buoyancy and hydrodynamic force are lumped to the end nodes in equal parts. Then, each node considers contributions from two adjacent line segments except for the segment at the anchoring position which has contribution from only one segment. A schematic view of the discretization of a line is presented in Figure 2.2.

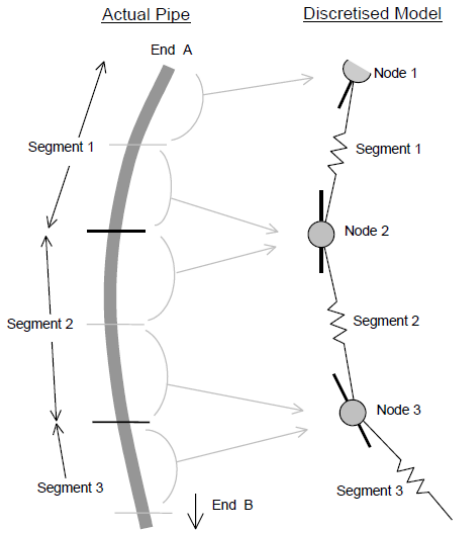

Figure 2.2 Basic discretization of line elements (Orcina, 2014)

For elements located at the sea surface, buoyancy, added mass and weight are determined based on the submerged portion of the segment up to the instantaneous surface elevation at each time step (Orcina, 2014).

In a segment, axial and torsional stiffness are represented by a combination of massless linear and torsional spring damper system at the center of each line segment, providing the effective tension component of the load as well as torque moment to the adjacent nodes. When bending stiffness is included in the model, rotational springs and

dampers at the nodes are included in the model. Torsional and bending stiffness are optional in order to model highly flexible components such as net threads. The complete structural model is described in Figure 2.3.

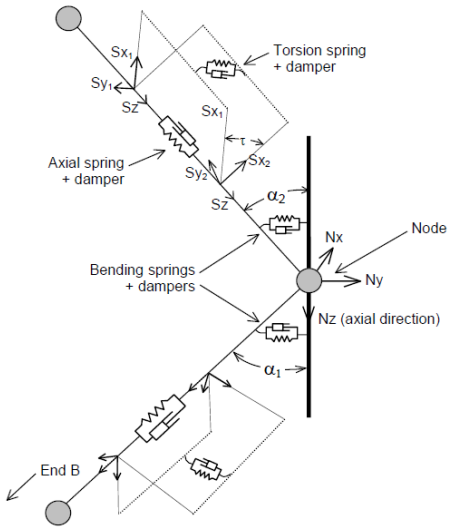

Figure 2.3 Structural line model (Orcina, 2014)

Once the structural model is complete, the calculation of forces and moments are determined in a sequence to calculate all components of the total load over lines. These components include tension force, bending moment, shear force and torsion moment. Their combined effect plus external loads from weight, buoyancy and hydrodynamic loads result on the total load over a segment. For the present analysis, the only effects included on the lines are tension forces and bending moment, thus the description of its calculation is presented.

To determine tension on a segment, the distance and the rate of increase of length between nodes is used plus the axial unit vector. In this case linear stiffness is applied on the model and the axial tension T_e is expressed as follows.

$$T_e = T_w + (P_o A_o - P_i A_i) \tag{2.74}$$

where

T_e : *effective tension*

T_w : *wall tension* $= EA\varepsilon\text{-}2\nu(P_o A_o - P_i A_i) + EAe(dL/dt)/L_o$

In the determination of T_w, axial stiffness, internal and external pressure (for the case of riser modeling) and axial damping effects are included. A description of each component on the equation is given.

EA: axial stiffness (E: Young's modulus, A: cross sectional area)

ε : total mean axial strain = $(L\text{-}\lambda L_o)/(\lambda L_o)$

L: instantaneous length of the element

λ: expansion factor of segment

L_o: unstretched length of the segment

v: Poisson ratio

P_i, P_o: internal and external pressure

A_i, A_o: internal and external cross sectional area

e: damping coefficient of the line

dL/dt: rate of increase of length

The effective tension resultant is applied at the nodes. Numerical damping e is defined later. Target axial damping is one of the user inputs, in our case this parameter is

set to zero since we are not interested on the structural response of the net but on it motions and hydrodynamic forces.

$$e = e_{critical}(Target\ axial\ damping/100) \tag{2.75}$$

where

$$e_{critical} = (2 * Segment\ mass\ L_o / EA)^{1/2}$$

After tension is obtained, the bending moment is calculated based on the relative angle between the axial direction of the node and the axial direction of the segment. The cartesian axis on the node rotates with it. The angle α between these vectors defines the effective curvature vector C which is orthogonal to the normal axial axis of node and segment. The magnitude of angle α is defined as $\alpha / (1/2L_o)$. Actual formulation for bending moment is as follows.

$$M = EI|C| + D(d|C|/dt) \tag{2.76}$$

EI: bending stiffness (E: Young's modulus, I: moment of inertia cross sectional area)

$D = (\lambda_b/100)D_c$

D_c: bending critical damping = $L_o(Segment\ mass * EI * L_o)^{1/2}$

λ_b: numerical target bending damping

Loads are then applied to the nodes, thus each node accounts for the contributions of the two adjacent nodes. With this forces, translational and rotational accelerations of each node are determined, then by integration velocity and position for the next time step are obtained (Orcina, 2014).

The hydrodynamic loads over the line segments are calculated using the modified version of Morison equation which accounts for the relative normal velocity and acceleration between segment and fluid flow (Haritos and He, 1992). Forces are calculated based on the cross flow principle in which the relative velocity between line and flow is separated into a normal component and a component parallel to the segment axis. Then, based on the normal component, x and y drag forces are computed. For normal directions x and y, normal projected area is used based on the product of the segment diameter and its length. Axial drag can also be calculated based on the component of velocity parallel to the segment axis. For drag coefficients C_d, the same values are applied in x and y direction while for the parallel direction a different value can be applied. The general expression for Morison equation used in this analysis, including drag and inertia components is described.

$$F_w(t) = \frac{1}{2}\rho C_d dl[v(t) - u(t)]\left|v(t) - u(t)\right| + \rho C_M \frac{\pi}{4} d^2 l\dot{v}(t) - \rho(C_M - 1)\frac{\pi}{4} d^2 l\dot{u}(t) \qquad (2.77)$$

In the previous expression, $F_w(t)$ is the fluid force, ρ is water density, d is segment effective diameter, l is length diameter, C_M and C_d are inertia and drag coefficient, $u(t)$ and $v(t)$ are element and fluid velocity while $\dot{u}(t)$ and $\dot{v}(t)$ are element and fluid acceleration. In this formulation, $v(t)$ and $\dot{v}(t)$ consider wave current interaction effects. In particular for the netting, given the small diameter of the threads components of the net, inertia forces are negligible. In this sense a detailed description of viscous load is given. Classical standard formulation is used in OrcaFlex based on

normal relative velocity and its components in x and y directions. This formulation is appropriate for general flow conditions (Casarella and Parsons, 1970).

$$F_x = \frac{1}{2} P \rho C_{dx} (d_n l)[v_{rx}] \left| v_{rn}(t) \right|$$
$$F_y = \frac{1}{2} P \rho C_{dy} (d_n l)[v_{ry}] \left| v_{rn}(t) \right| \tag{2.78}$$

On this expression $d_n l$ is the normal projected area of the segment; v_r is the relative velocity between element and fluid flow while P represents the proportion of the segment underwater to account for piercing effect of lines close to the sea surface. It is estimated by the intersection between a diagonal from the dry to the wet end of a segment and the free surface. Based on this proportion, the software evaluates buoyancy force and the node of application of the force on the line (Orcina, 2014).

The relative velocity form of Morison equation reveals that viscous drag contributes to the exciting force as well as to the damping force on the structure. Viscous effects of slender members of hull such as a cylindrical hull, TLP columns or truss elements are computed using the previous expression and combined to the potential forces to obtain the global force on a floating platform.

Force components are based on normal projected area which implicitly includes the relative angle of attack of fluid flow respect to the segment. The same formulation can be expressed to show how drag load changes with angle of attack between fluid and segment.

Considering an axially symmetric line with same C_d values for x and y axis and let φ be the angle between flow vector V and segment axis, then $V_n = V\sin(\varphi)$ and normal force is expressed as:

$$\begin{aligned} R &= \tfrac{1}{2} P\rho(dl)C_{dn}|V|^2 \\ |F_n| &= R\sin^2(\varphi) \end{aligned} \tag{2.79}$$

When using the previous formulation, C_d values become a major component of the formulation. It can be defined as variable during the simulation time based on Reynolds Number Re which is also dependent on φ.

$$Re_{flow} = \frac{|v_r|d}{\upsilon\cos(\varphi)}; \tag{2.80}$$

In the previous expression, υ represents kinematic viscosity. As for the values of inertia coefficient C_M, these are constant for the netting portion of the cage and equal to 2 based on previous experimental and numerical examples (Lader et al., 2007; Li et al., 2013a). As for the surface collar, C_M depends on KC and Re numbers and the treatment of this effect will be discussed in detail in further sections.

2.5.2 OrcaFlex buoy theory

The surface collar of the cage is modeled using short line elements to capture the circular shape of it. These elements are connected using six degree of freedom buoys. These buoys do not add neither drag nor inertia load to the system. This is achieved by applying negligible mass and volume in addition to forcing C_d, C_M and drag area equal to zero. Six degree of freedom buoys transfer translational and rotational motions, thus

bending stiffness of the material used to build the collar can be represented by this combination of lines and buoys.

As for the netting portion of the cage, lines representing the net are connected using three degree of freedom buoys which do not add drag nor inertia load to the system following a similar procedure as for six degree of freedom buoys. Three degree of freedom buoys only transfer linear motion, thus bending stiffness is not modeled. This assumption holds true for very flexible nets such as Nylon and Polyester nets. For metallic nets the assumption of zero bending stiffness is common practice; however further studies beyond the scope of the present work are required to confirm this assumption.

2.5.3 Coupled solution of motion for net and collar

Once line elements and buoys are modeled and located at its initial position on the numerical model, the motion on the time domain simulation under waves and current load must be determined. In OrcaFlex in order to calculate the global response of the system, a local equation of motion must be solved first for each element. The form of this equation of motion is given as:

$$M(p,a) = F(p,v,t) - C(p,v) - K(p) \tag{2.81}$$

In the previous formula, $M(p,a)$ is the local inertia load, $F(p,v,t)$ is the external load over the element, $C(p,v)$ is the element damping load and $K(p)$ is the element stiffness load. p,v,a and t are the position, velocity, acceleration and simulation time step respectively. The forcing component $F(p,v,t)$ includes $F_w(t)$ in addition to buoyancy and

gravity forces. The global equation of motion for the system has the same form as the local one, except that it uses global loads and vectors (Orcina, 2014). In order to solve this equation, two integration schemes, explicit and implicit methods, are available in OrcaFlex. Its selection is based on computational efficiency. Both methods account for geometric nonlinearities since system geometry is obtained at each time step.

Explicit integration solves for acceleration at the start of the time step and integrates *a* using forward Euler scheme, thus a constant time step *dt* is used as follows

$$\begin{aligned} v_{t+1} &= v_t + dt * a_t \\ p_{t+1} &= p_t + dt * v_{t+1} \end{aligned} \tag{2.82}$$

When using the explicit option, time step is small to achieve numerical stability, thus computational time is large and mainly dependent on the number of lines included in the model.

When using the implicit method, the Generalized α integration scheme is used (Chung and Hulbert, 1993). In this case the system of equations is solved at the end of each time step using an iterative solution. In this case longer time steps can be applied which reduces the computational time.

3. MOORING LINE DYNAMICS

3.1 Introduction

Previously, the calculation of loads over floating platforms and nets has been described. In this section, the mathematical description of the dynamic analysis of mooring systems in CHARM3D will be presented.

Mooring systems are common to all floating platforms being these used for oil and gas exploration and production or feeder platforms for fish farms. These systems are essential for station keeping and its detailed design needs to be carried out to withstand high energy seas assuring the safety of the platform. Several mooring systems can be identified such as spread mooring system, taut and semi tout system as well as tethers. In terms of materials, its selection is dependent of water depth and platform type. A combination of steel wire and chain is typically used in Spar platforms, while steel pipes or tethers are used for TLP platforms. As water depth increases, the use of synthetic materials such as polyester is considered. For the specific case of fish farms in deep water, a combination of chain and polyester lines have proven to be an adequate combination given the loads encounter in the experimental site used by Kampachi Farms offshore Kona, Hawaii (Cifuentes and Kim, 2015b). In that particular case, a single mooring line connected the feeder platform to the sea bed and an umbilical line join the cage to the vessel, thus the design of the mooring system was critical in the success of the daily operations.

Several methods to calculate the dynamics of mooring lines can be found being the simplest of all the quasi static catenary equations. This gives reasonable results when the platform is installed in shallow water and the payload from mooring lines is not significant. However, in deep water as the dynamic response of the mooring lines is significant due to its drag and inertia loading, as well as its mass when compared to the total mass of the platform, more complex analysis tools such as finite element method able to include nonlinear effects need to be considered.

For the study of mooring system, the rod theory presented by Garrett (1982) is adopted. This is a three dimensional model including line stretching which equation of motion can be expressed in a single global coordinate system, allowing an efficient representation of geometric nonlinearities.

3.2 Rod theory

The dynamic response of mooring lines modeled as slender rods is based on the position of the centerline of the rod in a 3D Cartesian coordinate system. As presented in Figure 3.1, the position vector ***r(s,t)*** is a function of arc length *s* measured along the rod and time *t*. At first, the rod is assumed to be inextensible which means *s* does not change between the deformed and original state of the rod. Under this assumption we can define the unit tangent vector to the space curve $\boldsymbol{r}'$, the principal normal vector directed along $\boldsymbol{r}''$ and the bi normal is directed along $\boldsymbol{r}' \times \boldsymbol{r}''$ where the prime symbols represent derivatives with respect to arc length *s*.

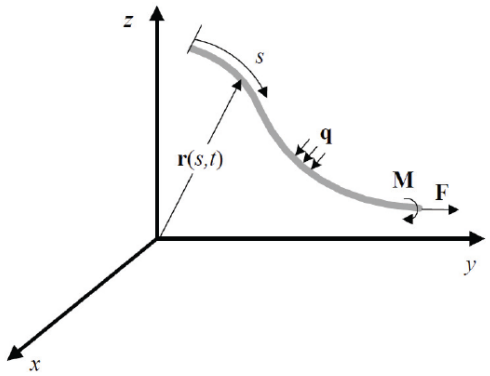

Figure 3.1 Rod coordinate system definition (Bae, 2013)

The equilibrium of forces and moments in a segment of the rod can be expressed in the equation of motion for a unit arc length segment of the rod.

$$\boldsymbol{F}' + \boldsymbol{q} = \rho \ddot{\boldsymbol{r}} \tag{3.1}$$

$$\boldsymbol{M}' + \boldsymbol{r}' \times \boldsymbol{F}' + \boldsymbol{m} = 0 \tag{3.2}$$

where $\boldsymbol{q}$ represents the applied force per unit length, ρ is the mas per unit length of the rod, $\boldsymbol{m}$ is the applied moment per unit length. $\boldsymbol{F}$ and $\boldsymbol{M}$ are the resultant force and moment along the centerline of the rod. Time differentiation is represented by the upper dot.

Bending moment is proportional to curvature and directed along the bi normal direction. It can be defined as follows, where EI is defined as bending stiffness and $\boldsymbol{H}$ is torque.

$$\boldsymbol{M} = \boldsymbol{r}' \times EI\boldsymbol{r}'' + H\boldsymbol{r}' \tag{3.3}$$

Substituting Equation (3.3) into Equation (3.2)

$$\boldsymbol{r}' \times \left[\left(EI\boldsymbol{r}'' \right)' + \boldsymbol{F} \right] + H'\boldsymbol{r}' + H\boldsymbol{r}'' + \boldsymbol{m} = 0 \tag{3.4}$$

and the scalar product of the above equation with $\boldsymbol{r}'$ yields.

$$H' + \boldsymbol{m} \cdot \boldsymbol{r}' = 0 \tag{3.5}$$

Assuming that there is no distributed torsional moment on the rod ($\boldsymbol{m} \cdot \boldsymbol{r}' = 0$) and considering that mooring lines have circular cross sections, there is no distributed torsional motion from hydrodynamic forces *H,* and $\boldsymbol{m}$ can be neglected. Equation 3.4 is re-written as:

$$\boldsymbol{r}' \times \left[\left(EI\boldsymbol{r}'' \right)' + \boldsymbol{F} \right] = 0 \tag{3.6}$$

Considering a scalar function $\lambda(s,t)$, this is called Lagrangian multiplier, the resultant force $\boldsymbol{F}$ can be defined as follows:

$$\boldsymbol{F} = -\left(EI\boldsymbol{r}'' \right)' + \lambda \boldsymbol{r}' \tag{3.7}$$

The scalar product of the previous expression and $\boldsymbol{r}'$ gives as a result

$$\lambda = \boldsymbol{F} \cdot \boldsymbol{r}' - \left(EI\boldsymbol{r}'' \right)' \cdot \boldsymbol{r}' \tag{3.8}$$

or

$$\lambda = T - EI\kappa^2 \tag{3.9}$$

where T is tension and κ is the curvature of the rod.

The equation of motion of the rod is obtained by combining Equations (3.7) and (3.1).

$$-\left(EI\boldsymbol{r}'' \right)'' + \left(\lambda \boldsymbol{r}' \right)' + \boldsymbol{q} = \rho \ddot{\boldsymbol{r}} \tag{3.10}$$

In addition $\boldsymbol{r}$ must satisfy the inextensibility condition

$$\boldsymbol{r}' \cdot \boldsymbol{r}' = 1 \tag{3.11}$$

If small stretch of the rod is allowed and this extension is linear, the boundary condition can be approximated as follows.

$$\frac{1}{2}\left(\boldsymbol{r}' \cdot \boldsymbol{r}' - 1\right) = \frac{T}{AE} \approx \frac{\lambda}{AE} \tag{3.12}$$

Combining the equation of motion of the rod in addition to either the inextensibility or extensible conditions, initial and boundary conditions plus applied load vector $\boldsymbol{q}$ there is enough information to determine the position vector $\boldsymbol{r}(s,t)$ and the Lagrangian multiplier $\lambda(s,t)$. The applied force vector can be expressed as the sum of hydrodynamic ($\boldsymbol{F}^d$), hydrostatic ($\boldsymbol{F}^s$) and gravity forces in terms of mass per unit length ($\boldsymbol{w}$) over the rod.

$$\boldsymbol{q} = \boldsymbol{w} + \boldsymbol{F}^s + \boldsymbol{F}^d \tag{3.13}$$

Further, the hydrostatic force can be expressed as

$$\boldsymbol{F}^s = \boldsymbol{B} - \left(P\boldsymbol{r}'\right)' \tag{3.14}$$

where $\boldsymbol{B}$ represents buoyancy force of the rod per unit length and P is the hydrostatic pressure at point $\boldsymbol{r}$ on the rod.

The hydrodynamic force $\boldsymbol{F}^d$ is then calculated by using Morison equation as presented.

$$\begin{aligned} \boldsymbol{F}^d &= -C_A \ddot{\boldsymbol{r}}^n + C_M \dot{\boldsymbol{V}}^n + C_D \left|\boldsymbol{V}^n - \dot{\boldsymbol{r}}^n\right|\left(\boldsymbol{V}^n - \dot{\boldsymbol{r}}^n\right) \\ &= -C_A \ddot{\boldsymbol{r}}^n + \bar{\boldsymbol{F}}^d \end{aligned} \tag{3.15}$$

where C_A is the added mass coefficient per unit length, C_M is the inertial coefficient per unit length per unit normal acceleration and C_D is the drag coefficient per unit length per unit normal velocity. $\boldsymbol{V}^n$ and $\dot{\boldsymbol{V}}^n$ are fluid velocity and acceleration respectively normal to the rod center line. They are defined as follows.

$$\boldsymbol{V}^n = \left(\boldsymbol{V} - \dot{\boldsymbol{r}}\right) - \left[\left(\boldsymbol{V} - \dot{\boldsymbol{r}}\right) \cdot \boldsymbol{r}'\right]\boldsymbol{r}' \tag{3.16}$$

$$\dot{\boldsymbol{V}}^n = \dot{\boldsymbol{V}} - \left(\dot{\boldsymbol{V}} \cdot \dot{\boldsymbol{r}}\right) \cdot \boldsymbol{r}' \tag{3.17}$$

where $\dot{\boldsymbol{V}}$ and $\boldsymbol{V}$ represent the total undisturbed fluid particle acceleration and velocity at the centerline of the rod.

In Equation (3.15) $\ddot{\boldsymbol{r}}^n$ and $\dot{\boldsymbol{r}}^n$ represent components of the rod acceleration and velocity normal to its centerline and can be defined as follows.

$$\dot{\boldsymbol{r}}^n = \dot{\boldsymbol{r}} - \left(\dot{\boldsymbol{r}} \cdot \boldsymbol{r}'\right)\boldsymbol{r}' \tag{3.18}$$

$$\ddot{\boldsymbol{r}}^n = \ddot{\boldsymbol{r}} - \left(\ddot{\boldsymbol{r}} \cdot \boldsymbol{r}'\right)\boldsymbol{r}' \tag{3.19}$$

Combining all previous expressions, the equation of motion of the rod under hydrostatic and hydrodynamic loading plus self-weight becomes.

$$\rho\ddot{\boldsymbol{r}} + C_A\rho_w\ddot{\boldsymbol{r}}^n + \left(EI\boldsymbol{r}''\right)'' - \left(\tilde{\lambda}\boldsymbol{r}'\right)' = \tilde{\boldsymbol{w}} + \bar{\boldsymbol{F}}^d \tag{3.20}$$

where

$$\tilde{\lambda} = T + P - EI\kappa^2 = \tilde{T} - EI\kappa^2 \tag{3.21}$$

$$\tilde{\boldsymbol{w}} = \boldsymbol{w} + \boldsymbol{B} \tag{3.22}$$

where $\tilde{T}$ is the effective tension on the rod and $\tilde{\boldsymbol{w}}$ is the wet weight.

The combination of Equation (3.20) with the line stretching condition represents the governing equations for the static or dynamic analysis of rods under hydrodynamic loading.

4. NUMERICAL SIMULATION OF DRAG FORCE AND DEFORMATION OF NETS UNDER STEADY CURRENT[۞]

4.1 Introduction

In this section, a complete description of the methodology to model nets using lines and buoys in OrcaFlex is presented. Conditions for projected area, wet mass and axial stiffness are imposed in the numerical model to simulate the response of a physical net. The focus on this section is on the drag force, volume and exposed area reduction of a single cylindrical net under steady current. This simple case will help to establish the basis for further analysis of cages focusing on the netting. Validation of the method is carried out by direct comparison of the numerical results with previously published experimental data. The use of a drag coefficient formulation as function of *Re* is included. Lastly, a convergence analysis based on number of elements used to represent the net is conducted.

4.2 Numerical model of nets

A net is basically a thread that has been arranged in a certain pattern such as diamond or square. The diameter of the thread is rather small ranging from less than a couple millimeters for nylon nets to four millimeters for metallic nets. Net openings are

---

[۞] Part of this section is reprinted with permission from "Numerical simulation of wake effect in nets under steady current" by Cifuentes and Kim 2015. Proceeding of the ASME 2015 34th International Conference on Ocean, Offshore and Arctic Engineering OMAE2015, St. John's, Newfoundland, Canada. Copyright © 2015 by ASME.

no larger than 50 to 60 millimeters. Some nets are built with nodes at the intersection of each basic shape while other are knotless. The selection of nets is based on the type of fish to grow, the stage of growth as well as environmental conditions and predators in the area of operation. Some of the net patterns used in industry are represented in Figure 4.1.

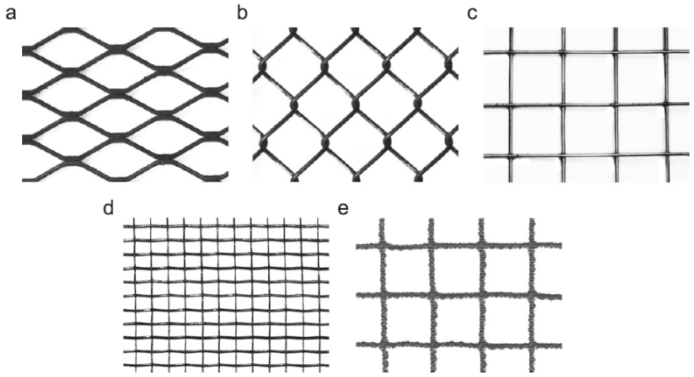

Figure 4.1 Net patterns (a) Flattened expanded, (b) Chain-link, (c) Welded, (d) Woven, (e) Nylon knotless. (Tsukrov et al., 2011)

The main parameter to characterize a net is its solidity ratio S_n which is defined as the ratio of the projected area of a net panel divided by the total area covered by the panel.

$$S_n = \frac{A_{projected}}{A_{total}} = \frac{L_{total} d}{A_{total}} \tag{4.1}$$

where L_{total} represents the total length of the thread in the net panel and d is the strand diameter. For each net outline, empirical formulations have been developed to obtain S_n values. Nevertheless, a most accurate calculation of this parameter is obtained when

using image processing techniques (Tsukrov et al., 2011). Other relevant net parameters are mass and buoyancy per unit area, and axial stiffness.

Considering the dimensions of the net threads and patterns openings, the modeling of each thread of the net is impractical since the number of elements on the numerical net will be extremely large and the computational time to obtain the response of a cage will be unreasonable for design purposes. Instead, an equivalent net is built using a finite number of lines and three degree of freedom buoys. This net has the same projected area, wet mass and axial stiffness as the physical net in order to replicate its response to environmental loading. A single twine on the numerical model represents now a group of twines in the physical net. This approach is represented in Figure 4.2.

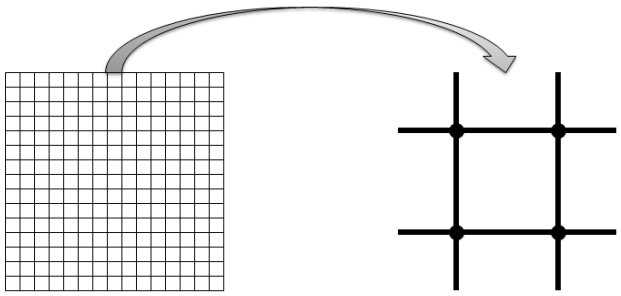

(a) (b)

Figure 4.2 Net representation (a) Physical net (b) Numerical equivalent net

Based on S_n the new diameter of the equivalent net is obtained. Following this procedure the projected area between physical and numerical net is the same. This is fundamental when calculating viscous loading from Morison equation. By using this approach a challenge is faced given that the equivalent net is now heavier than the

physical model. To solve this problem, the buoyancy of the three degree of freedom buoys is modified to achieve same wet mass between numerical and physical net. In this manner, inertia loading is captured. As for the axial stiffness, we assume that the axial stiffness of the numerical twine is equal to the axial stiffness of the group of threads that represents as presented by Fredheim (2005). The previous conditions can be summarized as follows.

$$\begin{aligned} &\sum L_m d_m = \sum L_p d_p \\ &S_{n_m} = S_{np} \end{aligned} \tag{4.2}$$

$$\begin{aligned} &Wet\ mass_m = Wet\ mass_p \\ &W_m - B_m = W_p - B_p \end{aligned} \tag{4.3}$$

$$\begin{aligned} &(EA)_m = \frac{n_p}{n_m}(EA)_p \\ &E_m = E_p \frac{n_p}{n_m}\frac{d_p^2}{d_m^2} \end{aligned} \tag{4.4}$$

where subscript *m* stands for numerical model and *p* for physical net. *L* and *d* represent the total length and diameter of the threads on the respective net. *W* and *B* are weight and buoyancy respectively. *E* is the Young Modulus of the net material while *A* is the cross sectional area of the twine of the net. Notice that the Young Modulus of the numerical net needs to be modified to achieve the conditions of same axial stiffness. The last element of the previous expressions is *n* which holds for the number of elements that represent the same part of the net structure in the numerical and physical net.

As for the surface collar, this can be represented exactly as in the physical cage since it is a single or double pipe arrange in a circular or square shape. The procedure to

discretize it is to divide the circumference in small segments connected by six degree of freedom buoys. These buoys have negligible properties and are used only to create complex geometries using straight line segments. The illustration of this procedure is presented in the following figure.

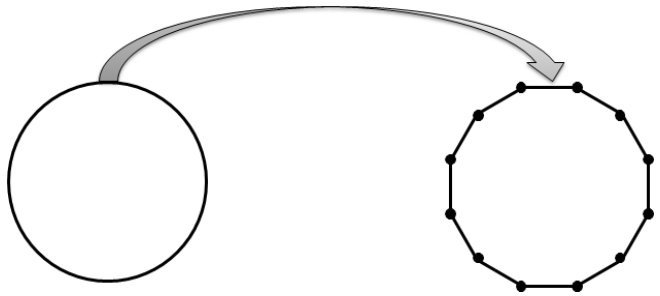

(a) (b)

Figure 4.3 Surface floater representation (a) Physical floater (b) Numerical equivalent floater

Once the numerical geometry has been completed, hydrodynamic loads are determined using a Morison force model. In this case a variable formulation for drag coefficient is used as described in the next section.

4.3 Drag coefficient formulation

In a net structure, inertia loading is negligible and the main force comes from the viscous drag term in Morison equation. This term is based on the relative normal velocity between the fluid flow and the lines representing the net. This relative velocity is calculated at each time step during the simulation considering current, line velocity,

and wave orbital velocity at each location. A critical component in Morison equation is the drag coefficient. This must be carefully selected according to the local relative velocity. In the present study, the formulation for drag coefficient presented by DeCew et al. (2010) has been used. The original expression was derived considering towed cables up to a *Re* of 10^5 (Choo and Casarella, 1971). In the present formulation, the expression for C_d is defined up to $Re=10^7$ capturing the drop in drag coefficient due to the transition to turbulent flow at high *Re.* The expression is derived for a smooth cylinder under steady current, making it suitable for the determination of drag forces on nets under wave and current effects (DeCew et al., 2006; Shainee et al., 2014; M. Shainee et al., 2013). The formulation is as follows.

$$C_d = \begin{cases} \dfrac{8\pi}{Re * s}(1 - 0.87s^{-2}), & 0 < Re < 1 \\ 1.45 + 8.55Re^{-0.9}, & 1 < Re \le 30 \\ 1.1 + 4Re^{-0.5}, & 30 < Re \le 2.33x10^5 \\ -3.41x10^{-6}(Re - 5.78x10^5), & 2.33x10^5 < Re \le 4.92x10^5 \\ 0.401(1 - e^{-Re/5.99x10^5}), & 4.92x10^5 < Re \le 10^7 \\ s = -0.077215655 + ln(8/Re) & \end{cases} \tag{4.5}$$

where C_d represents the normal drag coefficient and *Re* is Reynolds number. This formulation is implemented into OrcaFlex as an external variable. At each time step, the relative normal velocity and acceleration between line element and fluid flow is calculated, then by using this relative velocity, *Re* is obtained and finally the right C_d is calculated and input into Morison equation. *Re* is calculated considering the angle of attack between fluid flow and line elements as previously described.

This formulation is particularly important during the first stages of the simulation when the current load is gradually applied using a ramping function. By using a variable C_d, the transient response is avoided and the simulation does not show large variations in drag forces or numerical instability, thus shortening the total simulation time.

In order to validate this numerical approach, existing experimental data was used to compare the results and evaluate the strengths and weaknesses of the current model.

4.4 Validation using the results by Lader and Enerhaug (2005)

One of the benchmark studies related with the calculation of forces and deformations of nets under current was carried out by Lader and Enerhaug (2005). This study has been used by several researchers to validate their numerical approach given the conditions presented in the experimental analysis. In their experimental work, Lader and Enerhaug (2005) studied the forces and deformation of a single net exposed to steady current. Only the cylindrical portion is considered since the top and bottom of the net are open. The net was subjected to a set of five different current speeds. In addition, three different bottom weight configurations were analyzed. Ballast was applied by using steel cylinders located at 16 points along the bottom on the net. Testing conditions are summarized in Table 4.1.

In the experiment, a cylindrical net suspended from a steel ring was used. The stiff ring was designed to avoid deformations during tests runs, isolating this effect from the total system response.

Table 4.1 Experimental conditions

Description	Mass	Current speed *(m/s)*
C_1	16 x 400 *gr.*	0.13, 0.21, 0.26, 0.33, 0.52
C_2	16 x 600 *gr.*	
C_3	16 x 800 *gr.*	0.21, 0.26, 0.33, 0.52

To evade surface flow effects, the system was installed under water and kept in place by four pairs of lines. Loads cells were installed in these lines to capture the drag force over the system. The drag over the net was isolated by subtracting the drag forces on the upper ring and bottom weights. This experiment is a reliable source of validation since the net is detached from other cage elements, and thus the equivalent-net model can directly be tested. The net pen used in the experiment has a diameter of 1.435 m. and a draft of 1.44 m. A Raschel type nylon knotless net was used with a bar length of 16 mm, twine diameter of 1.8 mm. and S_n of 0.225. The density of the net is 1130 kg/m^3 and its Young Modulus is 82 MPa.

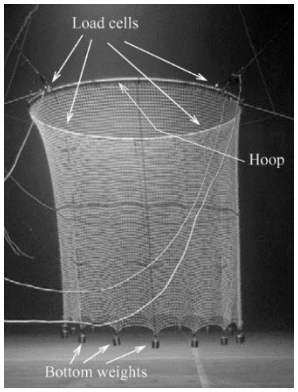

Figure 4.4 Experiment setup (Lader and Enerhaug, 2005)

The net was not scaled, thus the previously mentioned properties correspond to a full scale net. Results include drag force, volume and area reduction. Same results were extracted in our simulations to directly compare with the test data.

The numerical model in this case was built using the same dimensions as in the experimental work to avoid scale effects. The analyses were carried out using two numerical nets as presented in Figure 4.5. The objective is to analyze the influence of a higher number of elements and to check for convergence on the numerical results. Model A consists of 320 3-DOF buoys and 672 lines (10 rings using 32 segments), while Model B is built using 1280 3-DOF buoys and 2624 lines (20 rings using 64 segments). The ballast was modeled by incrementing the mass, up to the one specified for each case, at 16 buoys on the bottom of the cage in each model.

(a) Model A (b) Model B

Figure 4.5 Numerical representation of the net

4.4.1 Results

The results to be presented consider the drag force over the net, as well as volume and area reduction. To be consistent with the experimental data, the same

methodology was used to process the results for area and volume reduction. In the experiment, markers were located in the net, as described in Figure 4.6, and used to define volume (C_{vr}) and area reduction coefficient (C_{ar}). The coordinates of the corresponding nodes in the numerical net are then used to determine C_{vr} and C_{ar}.

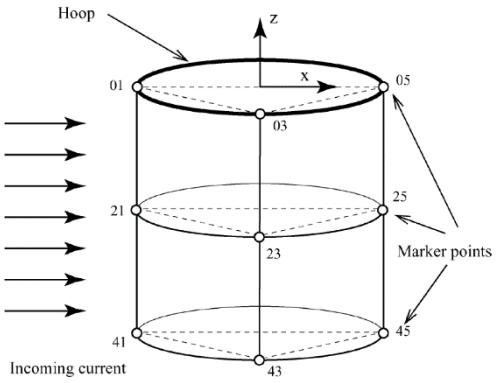

Figure 4.6 Coordinates location for volume and area reduction coefficient calculations (Lader and Enerhaug, 2005).

Volume is determined by the volume of two prisms enclosed by coordinates 01-03-05-21-23-25 and 21-23-25-41-43-45 showed in Figure 4.6. Volume is calculated using Equation (4.6).

$$V_p = \frac{1}{2}(A_{01,03,05} + A_{21,23,25})\left(-\frac{1}{3}((z_{21}-z_{01})+(z_{23}-z_{03})+(z_{25}-z_{05}))\right)+ \\ \frac{1}{2}(A_{21,23,25} + A_{41,43,55})\left(-\frac{1}{3}((z_{41}-z_{21})+(z_{43}-z_{23})+(z_{45}-z_{25}))\right) \tag{4.6}$$

where $A_{n1,n3,n5}$ is the area of the triangle spanned by the points *n1*, *n3*, *n5* and z_n is the vertical coordinate of point *n*.

Volume reduction coefficient C_{vr} is calculated according to Equation (4.7), where V_{p0} is the volume of the prims at zero current speed.

$$C_{vr} = \frac{V_p}{V_{p0}} \tag{4.7}$$

Exposed area is calculated by the projection of the cylindrical net onto a plane perpendicular to the current direction. This is calculated by Equation (4.8).

$$A_e = 2\left(-\frac{(y_{03} + y_{23})}{2}(-z_{23} + z_{03}) - \frac{(y_{23} + y_{43})}{2}(-z_{43} + z_{23}) \right) \tag{4.8}$$

where y_n is the coordinate of point n in the transverse direction.

Area reduction coefficient C_{ar} is calculated according to Equation (4.9), where A_{e0} is the area of the projection at zero current speed.

$$C_{ar} = \frac{A_e}{A_{e0}} \tag{4.9}$$

Results are presented as direct comparison between numerical and experimental data. Since drag force depends on projected area, the corresponding deformation of the net under the conditions analyzed is a key point of the study. As current speed increases, the internal available volume of the net decreases. In addition, as the ballast weight increases, a vertical deformation of the net is expected, thus a higher drag will be developed since more area will be exposed. This complex scenario can be observed in Figure 4.7 where the deformation of the experimental cage under C_1 at 0.33 m/s current speed is presented.

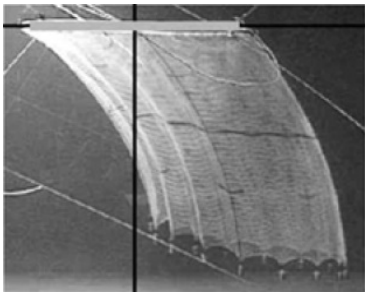

(a)

Figure 4.7 Cage deformation (Lader and Enerhaug, 2005)

The results showing the correlation between experiments and numerical simulation for drag force are presented in Figure 4.9 for the three ballast conditions using model A and B. A total of 14 simulations were carried out for each model.

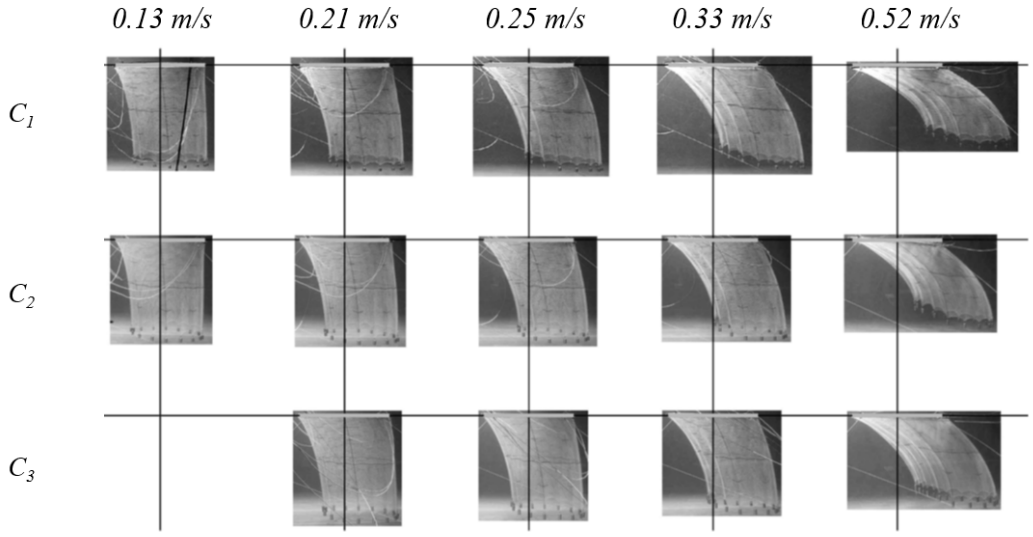

Figure 4.8 Calculation matrix from experiments (Lader and Enerhaug, 2005)

In addition, the numerical calculations by Endresen et al. (2013) is included to evaluate the accuracy of the present scheme compared to a numerical tool developed for the calculation of forces in net structures. This numerical tool, called FhSim, was

developed by SINTEF and it is based on triangular net elements connected by nodes. It uses an equivalent net approach similar to the one presented in our calculations where drag force is obtained based on Morison cross flow model, further details of FhSim can be found in the work by Enerhaug et al. (2012).

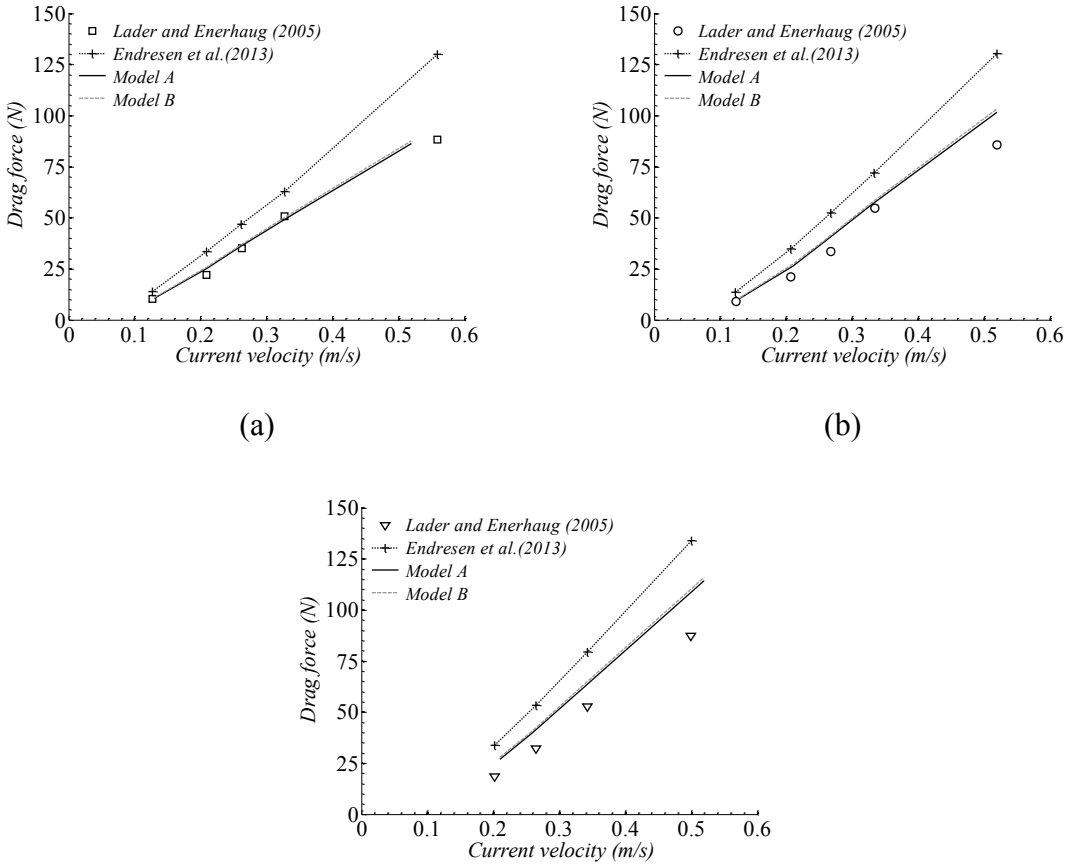

(a) (b)

(c)

Figure 4.9 Drag force comparison (a) C_1, (b) C_2, (c) C_3

From Figure 4.9 it can be seen that the present numerical model tends to over predict the drag load. This is a typical trend for numerical simulations of flexible net

structures when using a Morison force model (Endresen et al., 2013). The maximum average error of 38 % comes from the model with the heaviest ballast weight. This tendency can be observed across the spectra of results. As the mass of the ballast system increases, so does the error. This can be explained considering the deformation experienced by the net in the vertical direction. In the numerical model, the equivalent diameter of the cylinders representing the net is based on S_n to match the total projected area. As the real net stretches, the total area covered by the net increases, while the projected area keeps its value. This reduces S_n compared to the unloaded case. This effect is not accounted for in the numerical results, thus, the total projected area is larger in the numerical model when compared to the experimental net, and consequently a higher drag force is expected. The difference in projected area between numerical and experimental net becomes more significant as ballast mass increases, explaining the large values for relative error as heavier ballast is applied. The final dimensions of the net pen for the different ballast conditions are not described by Lader and Enerhaug (2005); however it is mentioned that the length of the thread attached to the upper ring stretches up to 12 % when compared to the unloaded case.

The next set of results evaluates the deformation of the cage in terms of volume and area reduction when exposed to current loading.

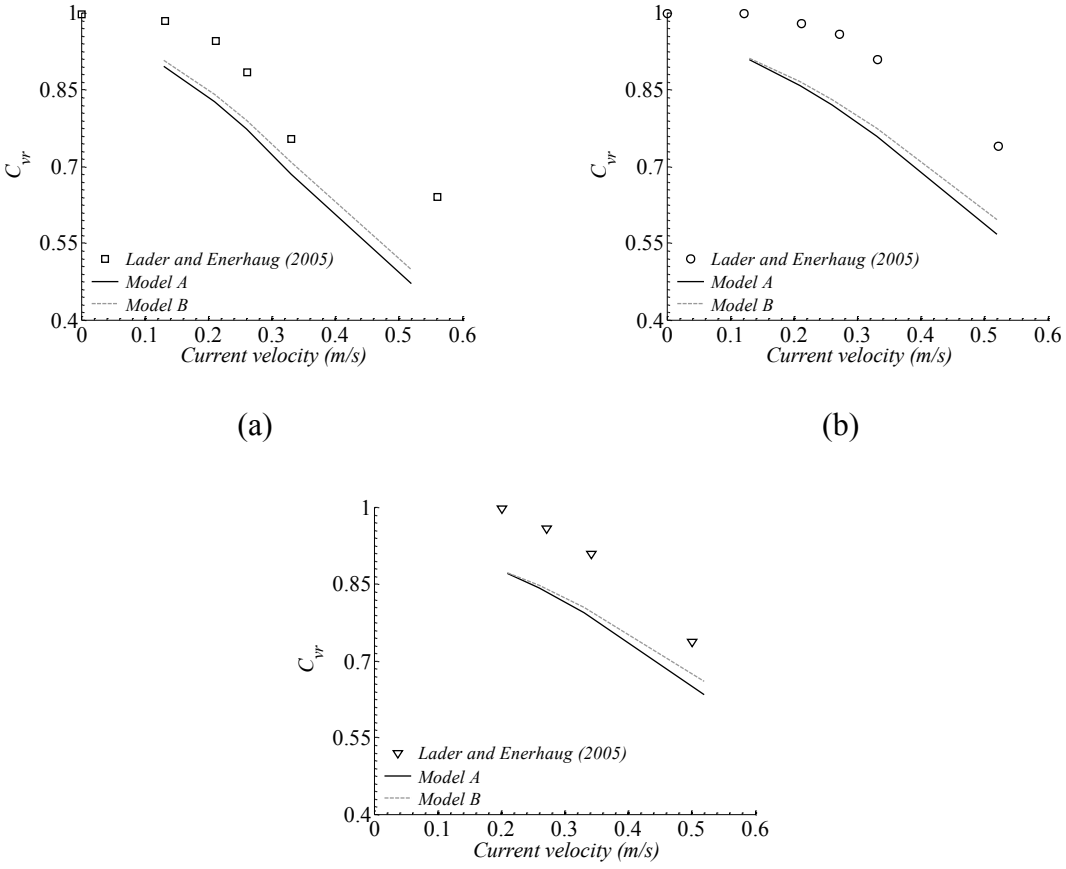

Figure 4.10 Volume reduction coefficient C_{vr} comparison (a) C_1, (b) C_2, (c) C_3

Internal volume of the net is a critical concern for fish farmers since the health of the fish depends on the available space, among other factors. A close estimation of this effect will greatly help to improve the design of the ballast system to be installed, being this system a set of hanging masses as in the present case, or a ballast ring. From the plots of volume reduction coefficient the model over predicts the deformation of the net. Under all conditions, the available volume at the end of the simulated period is smaller to the one capture in experiments. The increase in the number of elements slightly

increases the accuracy of the calculations, particularly for high current speeds, though improvements are not larger than 4%.

The third parameter to analyze is the projected area of the net. In early works (Aarnes and Loland, 1990), drag forces were determined based on the projected area of the central vertical plane of the net. Thus, the determination of this area is useful for comparison of numerical and analytical methods when computing drag forces.

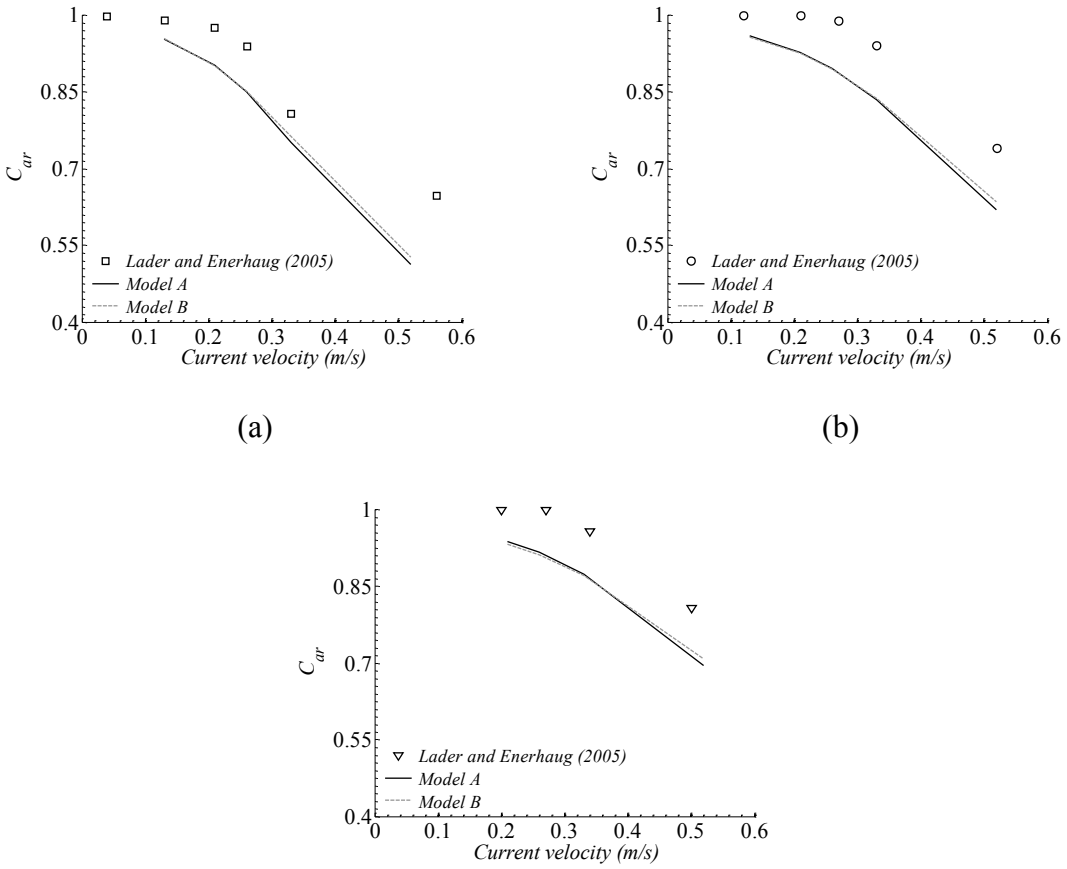

Figure 4.11 Area reduction coefficient C_{vr} comparison (a) C_1, (b) C_2, (c) C_3

The area reduction coefficient shows that the numerical model over predict the deformation of the central plane, which correlates with the volume reduction. The projected area at the end of the simulation period is smaller than the measure in experiments. As for the convergence of the results when a large number of elements is included, the effect over the results is negligible, thus it can be concluded that a small number of elements is enough to obtain close estimates of exposed area on a flexible cage.

4.5 Discussion

Based on the presented results, an equivalent net considering the same projected area, wet mass and axial stiffness as the physical net can closely capture forces and deformations over a wide range of current speed. Drag force is highly dependent on deformation of the cage which comes from the current speed as well as the extension in the vertical direction due to the ballast installed at the bottom. This extension has a direct implication on the solidity ratio of the netting which induces large errors for the results under the heaviest ballast set. Drag load increases with ballast since ballast controls the overall deformation of the cage and more area is exposed to the flow. Another important result comes from the fact that the relation between force and current speed does not follow the expected U^2 relation. For low current speed (U) drag is proportional to U^2; however for higher current speed the relation tends to be linear driven mainly by the deformation of the cage. In addition, at about 0.3 m/s, there is an inflection point in the

drag curves which suggest that changes on the projected area on the cage become significant at the region of higher current velocities.

When drag force calculations are compared to a similar numerical approach (FhSim), the current numerical method shows better agreement with respect to experimental data.

As for volume and area reduction coefficient, numerical results over predict deformation of the cage. The estimates show a larger reduction of internal volume. This can be considered a conservative result from a fish farm operational point of view. Results show a similar tendency as the experimental data where a linear tendency is seen for high current speeds. Considering that the uncertainty on experiments due to the technique used to measure deformation is ±10 %, numerical results can be considered valid for this range of current speed.

Across the spectra of analyses, the influence of the use of a large number of elements does not significantly affect the results, increasing confidence on the base numerical methodology. In terms of computational efficiency, while for Model A, a couple of minutes are needed to obtain the results, this time increases approximately 10 times when compared to Model B. This is mainly due to the complexity of the model when more lines are included. In OrcaFlex, lines are the most time consuming element on the model reason why is of relevance to find the equilibrium between element density and accuracy of results.

Several sources of uncertainty must be considered when judging the accuracy of the presented results. While on the numerical model, it is assumed that the flow direction

will not change due to the presence of the net, it has been shown that flow, especially at high speed, will change directions when crossing the upstream portion of the net (Gansel et al., 2012). In addition, current velocity is not constant over the depth of the tank in experimental conditions (Moe et al., 2010), while on the numerical model, current profile is always constant over the water column.

It is important to recall that shielding effect is not included in the calculations, thus an over prediction of loads is expected. Nevertheless, this analysis serves as the starting point for further development considering the close agreement with experimental data using the rational and computationally effective approach presented in this section.

Further analysis including shielding effect must be carried out in order to increase the accuracy of the presented numerical methodology.

5. NUMERICAL SIMULATION OF THE COUPLED DYNAMIC RESPONSE OF A SUBMERGED FLOATING TUNNEL[۞]

5.1 Introduction

As presented in section 4, a net can be represented as an array of slender cylinders which, when acting together, can be used to determine forces and deformations of a more complex structure such as a net pen. Other interesting analysis of the hydrodynamic response of slender structures using variable drag coefficient include the analysis of risers near touchdown and Submerged Floating Tunnels (SFT). In countries such as Norway and Italy where there are countless narrow fjords and straits, SFT is considered as an alternative for land connections. SFT is a simple structure that is installed underwater at a given depth, kept in place by the combination of positive buoyancy and tethers anchored to the sea bed (Di Pilato et al., 2008). The SFT concept was well understood at the end of the 19th century and the interest for this type of structure was revived in the 1960's with some minor research effort in Norway and Italy (Østlid, 2010).

Subsequently, further studies were completed to better understand the dynamic response of a SFT (Hong and Ge, 2010). Since then, although no such a structure has ever been built, the interest for the concept has grown in the engineering community. A

[۞] Part of this section is reprinted with permission from "Numerical simulation of the coupled dynamic response of a submerged floating tunnel with mooring lines in regular waves" by C. Cifuentes, SJ Kim, MH Kim and WS Park 2015. Ocean Systems Engineering, Vol. 5. No. 2 109-123.

complete guide for the design and characteristics of a SFT can be found in the work by Jakobsen (2010) summarizing several feasibility studies carried out in Norway.

In order to design and install a SFT structure, analyses under multiple load scenarios are necessary. For real design and construction, a rational global performance analysis procedure, including mooring lines, should be developed. By performing a global performance analysis, engineers can simulate the static/dynamic behavior of SFT under various environmental loading conditions and then observe important features of the system, such as motions, internal forces, anchor reactions, and structural stresses of the tunnel and tethers. In addition, structural safety, structural stability, fatigue damage and operational life can also be estimated.

Some of the critical loads and hazards include (a) hydrostatic pressure and self-weight, (b) environmental loads including waves, current, earthquakes and internal waves, (c) loads due to internal traffic and ballast, and (d) accidental loads such as internal explosions, collisions, and mooring system failure (Lu et al., 2011). In addition, fatigue of tethers due to Vortex Induced Vibration (VIV) is also of interest for design and operational stages (Hong and Ge, 2010).

Several researchers have performed analyses and experiments for SFT under mainly regular wave loading. Examples include global performance analysis focused on tether tension and tunnel displacements carried out by Kunisu et al. (1994) which revealed direct proportionality between wave height and mooring line tension. The direct relations between surge-heave amplitude and buoyancy to weight ratio (BWR) was presented by Hong and Ge (2010) based on a series of experiments. The experimental

findings include (i) as pretension increases with larger BWR, the translational displacements increase, and (ii) the submergence depth has a significant impact on the reduction of dynamic responses due to the reduction of pressure fluctuations over the submerged tunnel (Oh et al., 2013).

Wave directionality and wave-current interactions are also important factors to consider in the design of a SFT. Numerical tools, such as computational fluid dynamics (CFD), fluid structure interaction (FSI), finite element method (FEM), and stochastic dynamic methods need to be further developed for the detailed study of SFT dynamics. Analytical solutions have also been developed to estimate forces over submerged cylinders exposed to waves (Romolo et al., 2008). Each method can provide invaluable information at some steps into the design process. Nonlinearities such as drag loads and large displacements can be obtained in time domain using numerical procedures (Kunisu, 2010). The combined effects of hydrodynamic and seismic loads was reported in Di Pilato et al. (2008). For wave induced dynamic loadings, either Morison model or BEM can be used (Kunisu, 2010).

Other nonlinearities can also be included in time domain analysis. One example is the presence of snap loads over the tethers under slack condition. This situation is undesired since high tensions are induced for a short period of time prompting high stresses over the anchor and connection points to the submerged tunnel. Studies have shown that snap loads can be avoided using inclined tethers to anchor a SFT (Lu et al., 2013, 2011).

In the present study, the coupled dynamic response of a Submerged Floating Tunnel (SFT) and mooring lines under regular waves is solved by using two independent numerical simulation methods, OrcaFlex and CHARM3D, in time domain. Variations of Buoyancy to Weight Ratio (BWR), wave steepness/period, and water/submergence depth are considered as design and environmental parameters in the study. Two different mooring-line configurations, vertical and inclined, are studied to find an optimum design in terms of limiting tunnel motions and minimizing mooring-line tension. The numerical results are successfully validated by direct comparison against published experimental data. The results show that tunnel motions and tether tension grow with wave height and period and decrease with submergence depth. The inclined mooring system is more effective in restricting tunnel motions compared to the vertical mooring system. Overall, the present study demonstrates the feasibility of this type of structure as an alternative to traditional bridges or tunnels installed at seabed.

5.2 Numerical simulation of SFT under regular wave loading

Based on previous findings, the present work looks into the global performance and coupled dynamic response of the submerged floating tunnel and mooring system by using two different numerical approaches, OrcaFlex (Orcina, 2014) and CHARM3D (Bae and Kim, 2014; Eom et al., 2014; Kang and Kim, 2014; Kim et al., 2005; Yang, 2009). Differences in the numerical models arise in mooring-line treatment i.e. OrcaFlex uses a lumped mass model, while CHARM3D uses the FEM approach proposed by

Garrett (1982). In both cases, the tunnel is exposed to regular wave loading where crest lines are parallel to the axial direction of the tunnel as presented in Figure 5.1.

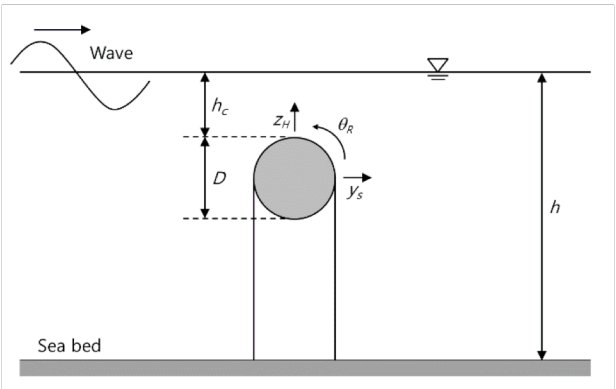

Figure 5.1 SFT under vertical mooring configuration

Conditions analyzed in this study include a wide range of wave steepness, BWR, water depth, and two mooring configurations. Numerical results for tether tensions and tunnel displacements are systematically compared with experimental results by Oh et al. (2013).

A couple of different approaches were taken when modeling the SFT depending on the capabilities of each numerical tool. In CHARM3D the SFT was modeled using a dummy underwater platform which considers all hydrodynamic coefficients equal to zero. This was done to connect the mooring lines to the platform. Viscous drag load was modeled by using a Morison element with constant C_d and C_M values equal to 1.2 and 2.0 respectively. In OrcaFlex the SFT is modeled as a line element connected to mooring lines by three degree of freedom buoys which do not add either inertial or viscous load to the system. The force is calculated using Morison equation as for the case of net

modeling. Inertia coefficient is constant and equal to 2.0, as for the drag coefficient, the variable formulation described in Equation (4.5) is applied. To analyze the effect of scale between prototype and model the full scale SFT was modeled in CHARM3D while in OrcaFlex, the model dimensions were used in the calculations. Later, results for both codes in full scale are compared against experimental results.

5.3 Physical experiments

The numerical analysis is compared with the experimental results presented in the work by Oh et al. (2013). In that study, the dynamic response of a single SFT section under wave loading is analyzed. The experiments were carried out in a two dimensional wave tank, 53 m. long, 1.25 m. high and 1 m. wide. Several parameters are varied in the experiment to reveal its effect over the dynamic response of the structure. Main results from this study are motions of the SFT and forces on mooring components. The configuration for vertical and inclined tethers used in the experiment is given in Figure 5.2.

The SFT is installed with its center at 50 cm. over the bottom of the tank. The experiment considers 1:100 scale factor. Mooring lines form a 30 degree angle with respect to a vertical plane in Figure 5.2b. BWR (buoyancy-weight ratio) variation is obtained by adding ballast to the tube. Motion tracking devices follow the displacements of two targets on the body to obtain accurate measurements of motions. Waves were generated for 60 seconds for each test condition presented in Table 5.1. Both

configurations, vertical and inclined mooring systems, were analyzed under the same wave conditions. More details of the experimental set up are given in Oh et al. (2013).

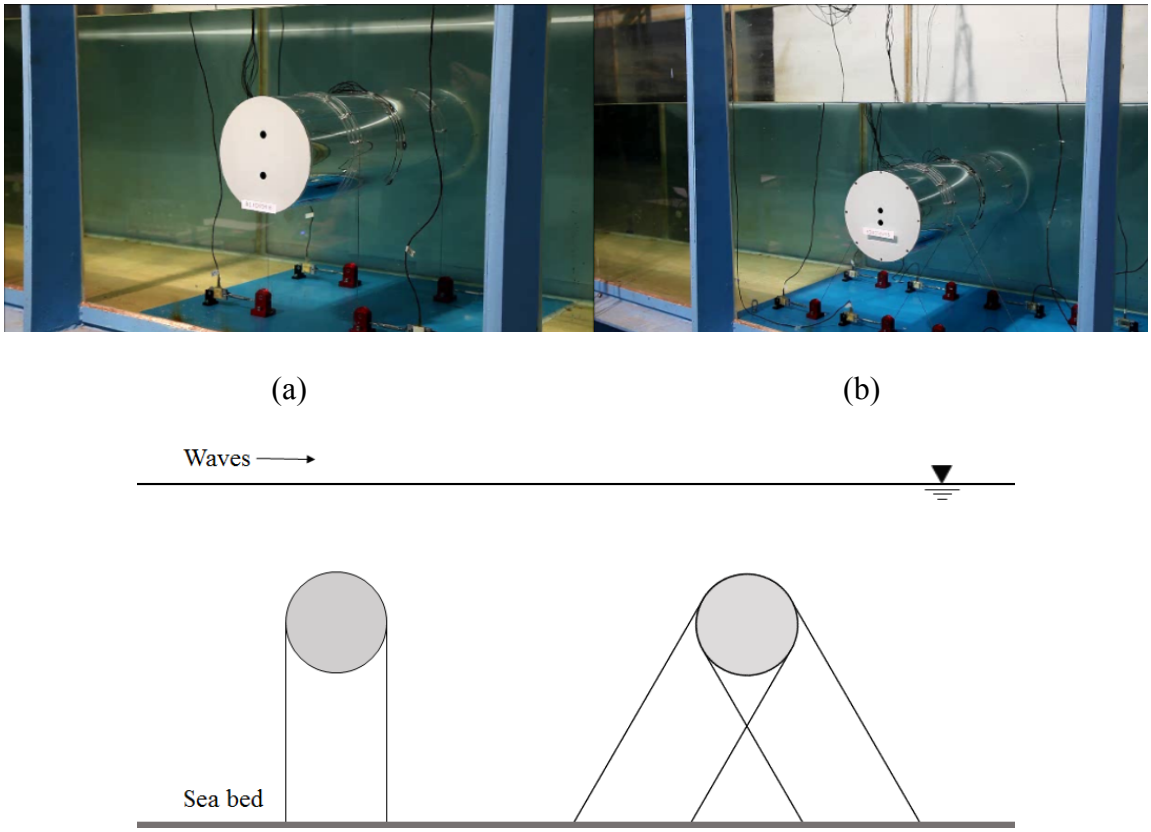

Figure 5.2 Experimental configuration (a) Vertical mooring (VM), (b) inclined mooring (IM)

Table 5.1 Prototype conditions

Parameter	Values
Diameter (m)	23
Water depth (m)	65 – 80 – 95
BWR VM	2.2 – 2.6 – 3.0
BWR IM	2.8 – 3.4 – 4.0
Wave period (seconds)	6.5 – 8.0 – 10.0 – 13.0
Wave steepness *s*	0.013 – 0.027 – 0.040 – 0.053

5.4 Results of coupled analysis

As presented in the previous section, the displacements of the SFT and forces on the tethers are the main focus of attention in this analysis. The variation of dynamic responses of the SFT under various wave conditions, water depth, and tether angles is investigated. In the case of CHARM3D, C_d is constant and equal to 1.2 while C_M is 2 considering a simple circular cylinder. In OrcaFlex, C_d is variable depending on flow conditions while C_M is equal to 2. Same values are used for the calculation of hydrodynamic loads on tethers. In both codes, incident waves were modeled using Airy's linear wave theory.

For VM (vertical-mooring) configuration, the relationship between wave elevation, tunnel surge, and mooring tension is presented in Figure 5.3. In this figure, the prototype condition is as follows: water depth is 80 m, wave period = 13 s, wave steepness = 0.04 and BWR = 2.6.

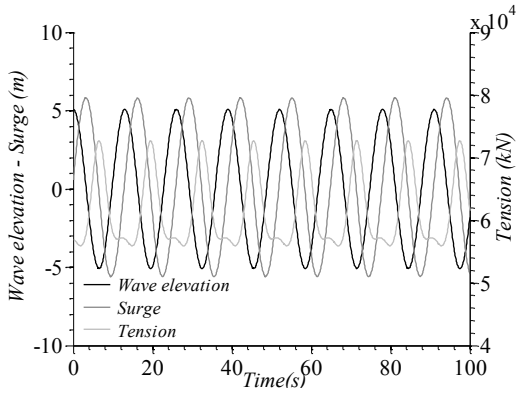

Figure 5.3 Wave elevation, surge and tension variation

From the figure, it can be observed that effective tension of mooring lines and wave elevation are 180 degrees out of phase meaning that tension reaches its maximum value at wave trough. At this instant in time, tethers are at vertical position since surge is zero. At the same time, the vertical acceleration of the SFT is at its maximum value pointing upwards. This combination generates the maximum tension on the tether. On the other hand, minimum tension is reached at the point where surge is maximum and vertical acceleration is minimum. At this point the SFT reaches its deepest position due to set-down effect, which is caused by an inverted-pendulum-like motion. We can also see some nonlinear behaviors on the line tension.

The variation of heave and surge motions of the vertically moored SFT over the wave conditions tested, was calculated considering a particular water depth of 80 m. and BWR equal to 2.6 for the vertically moored case. In Figure 5.4, the results from experimental and numerical data are presented to validate the numerical-simulation schemes. In the following figures, solid lines represent experimental data while solid

markers show the results obtained using CHARM3D and open markers represent the results obtained by OrcaFlex.

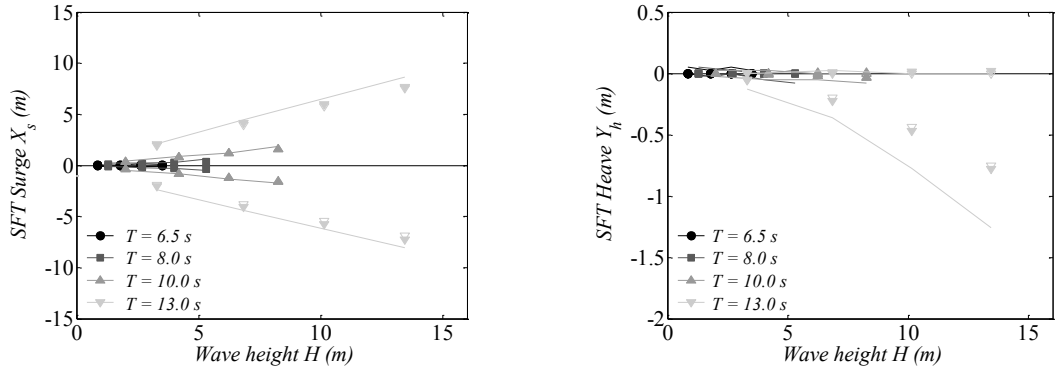

(a) (b)

Figure 5.4 (a) Surge and (b) Heave SFT motions as function of wave height/period.

In the plots, the origin for surge and heave is located at the center of the tunnel. From the results of Figure 5.4, numerical simulations agree well with experimental data. The trends in surge and heave motions are well captured validating the approach applied in both numerical schemes. Surge motion is directly related to wave height and wave period. For small and short waves, the response of the tunnel is small even considering the freedom of motion in this mode since the mooring lines do not restrict horizontal displacement.

As waves increase in height and period, the surge becomes significant. The particle kinematics of longer waves penetrates deeper inducing significant SFT motions. Due to the vertical restriction by vertical mooring system, heave motion is insignificant for most of the wave conditions. Heave motion only becomes significant in the negative

direction for large periods and high waves, which is caused by large surge through set-down effect.

The correlation shows that both codes underestimate the negative maximum heave amplitude for the 13 s. wave, which can be attributed to nonlinear effects associated with slack mooring, incident-wave deformation due to the presence of SFT, radiated waves caused by SFT motions, and typically larger unwanted reflected waves for larger-period waves in the wave tank. Secondary viscous effects may not be important but may also contribute to the differences. The correlation between CHARM3D and OrcaFlex is also reflected in Figure 5.4, where the results from both codes are similar.

A particularly interesting condition to study is the 100 year return period storm defined by the Society of Submerged Floating Technology. This condition corresponds to a 13 s. wave period and 0.04 wave steepness. The results for surge and heave under this particular condition as function of water depth and BWR are presented in Figure 5.5 for the vertically moored SFT. The 65 m., 80 m., and 95 m. water depths correspond to 15 m., 30 m., and 45 m. submergence depth.

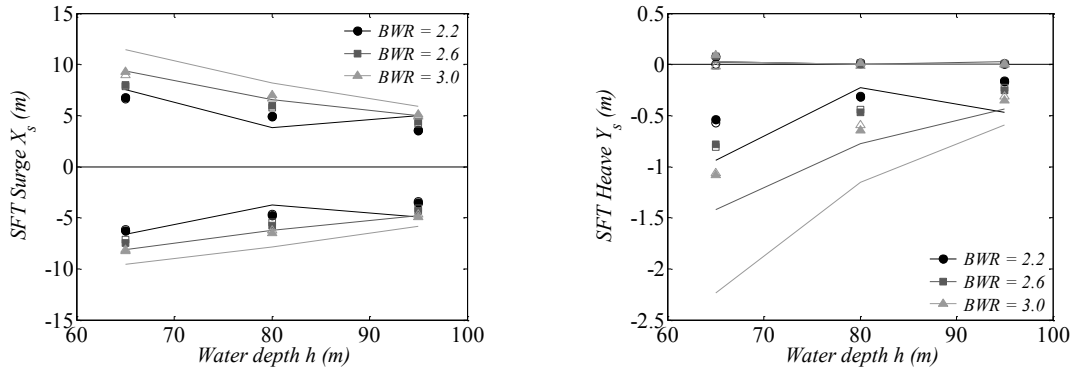

(a) (b)

Figure 5.5 (a) Surge and (b) Heave SFT motions as function of water depth.

As BWR increases, so does the dynamic response of the tunnel both in surge and heave. This is due to the increase of surge stiffness so that its natural frequency is moving closer to the incident wave period. Both codes generate a similar trend, which also agrees with experimental data. The dynamic response of the SFT increases as submergence depths decrease. In the case of 13 s. wave period with wave steepness = 0.04, the simulation results tend to underestimate the experimental values due to the reasons stated in regard to Figure 5.4. For 80 m. and 95 m. water depths, the wave field is minimally modified by the presence and motion of the structure, thus the numerical and experimental results tend to converge.

One important factor to consider when designing any floating offshore structure is the calculation of the maximum loading on the station-keeping system. In this regard, mooring line tension as function of wave period and steepness is presented in Figure 5.6. The case is for 80 m. water depth and BWR=2.6. The plot represents the tension on a single mooring line since the signals from the four vertical mooring components are

similar for any given wave condition. Horizontal line represents the value of pretension on mooring lines.

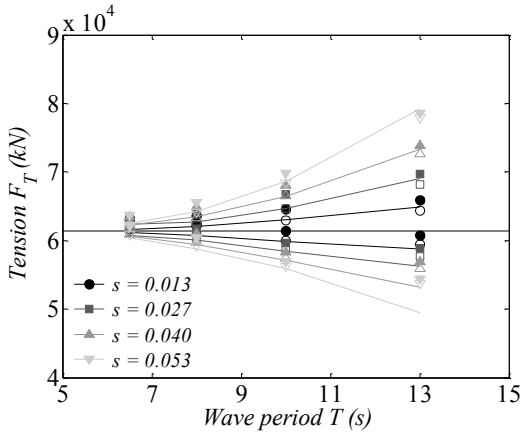

Figure 5.6 Tension force on vertically moored SFT

Tension forces grow with wave period and wave height. Maximum and minimum loads are not symmetrical with respect to the initial pretension. This difference comes from nonlinear and set-down effects. The numerical simulations recover the general trends of experimental data. The small differences between CHARM3D and OrcaFlex results can be attributed to different methods in generating incident wave kinematics. In OrcaFlex, Wheeler stretching method was used instead of vertical stretching used in CHARM3D. As a result, we can observe the asymmetry on the vertical acceleration of fluid at the given submergence depth, as shown in Figure 5.7 for the 100-yr storm condition. The positive vertical acceleration is larger inducing a higher upward load. In the OrcaFlex case, it also needs to be reminded that variable drag

coefficients are used for different flow conditions in calculating wave-induced drag forces.

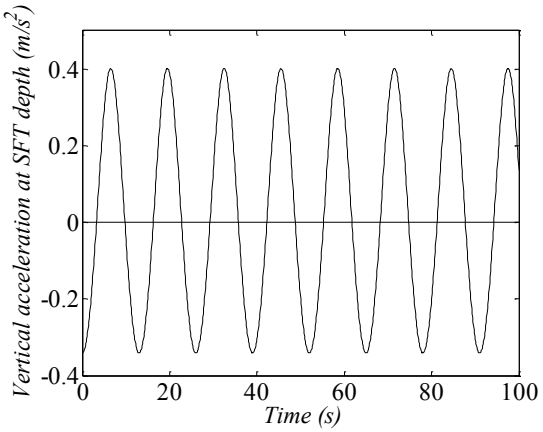

Figure 5.7 Fluid acceleration by OrcaFlex at SFT depth

The last set of data reveals the dynamic response of the submerged floating tunnel using the inclined mooring configuration as shown in Figure 5.2b. This is an interesting alternative since the surge and heave responses are significantly reduced compared to the vertical-mooring case. In addition, the load is now distributed in 8 tethers. This configuration is intended to reduce the linear motions of the tunnel.

Unfortunately, no experimental data for surge and heave motions are available from the experimental paper. However, from video recording, it was observed that the motions are greatly reduced compared to the vertical mooring case, which can also be confirmed by the present numerical simulations, as shown in Figure 5.8 (water depth=80 m., BWR=2.6). Even for high energy seas, the displacements of the structure are suppressed by the restriction of the inclined mooring (IM) system. It can be concluded

that the inclined mooring system is very effective in minimizing SFT motions. Given the distribution of mooring lines being symmetric with respect to each other, the load is equally distributed and, as in the case for vertically moored tunnel, the tension results for a single mooring line are also presented for the same case in Figure 5.9. The effective tension on each line is reduced but the total mooring tension force increases when compared to the VM case since the displacements are highly restricted.

In the next figure open markers represent OrcaFlex results for the VM configuration while solid markers represent the results for the IM configuration.

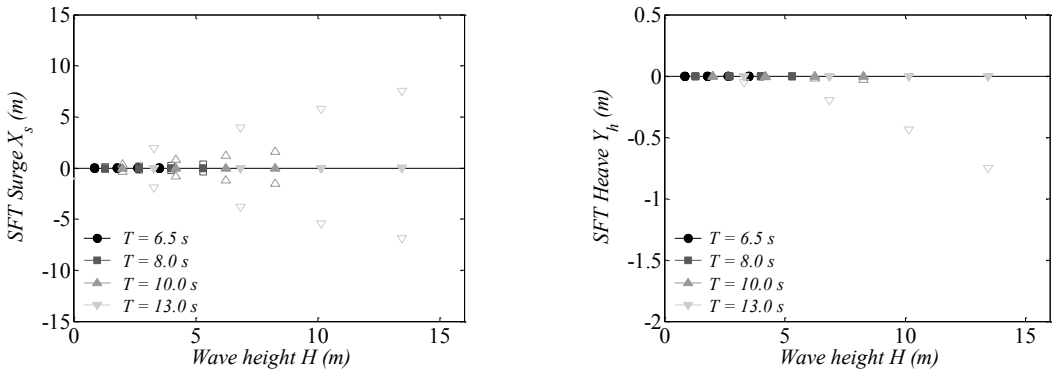

(a) (b)

Figure 5.8 (a) Surge and (b) Heave SFT motions for VM and IM as function of wave height and period

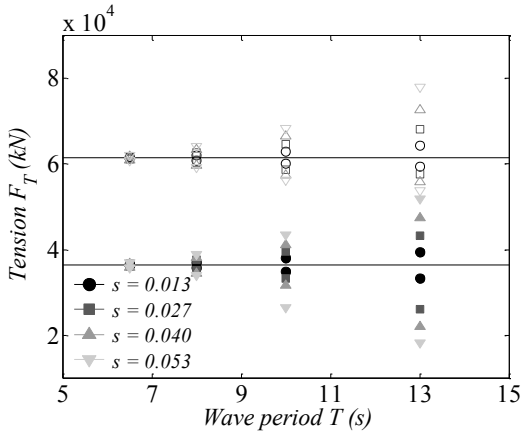

Figure 5.9 Numerical results for Tension for VM and IM as function of wave height and period.

Finally, the experimental results for mooring line tension including all wave periods for the IM system are available for the case of 80 m. water depth and BWR=3.4 and they are compared with OrcaFlex and CHARM3D numerical simulation results in Figure 5.10. A similar trend as for the case of vertically moored tunnel is observed in this case. Mooring tensions increase as wave period and wave steepness increase. The rate of increase is almost linear with wave periods and heights. Both numerical simulations agree well with experimental data and present similar trends. Their differences are generally small. From the above comparisons, it is clear that the inclined-mooring-line arrangement presents better performance in terms of tunnel displacements and accelerations.

In the next figure solid lines represent experiments, solid markers CHARM3D results and open markers OrcaFlex results. Horizontal line represents mooring lines pretention.

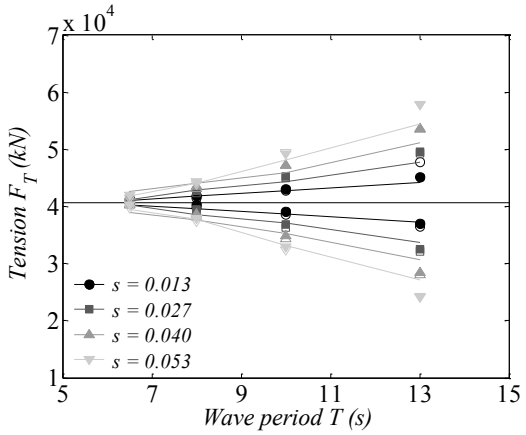

Figure 5.10 Tension force on inclined mooring

5.5 Discussion

The fully coupled dynamic analysis of a submerged floating tunnel under regular wave loading has been carried out. Main results obtained include translational (surge and heave) motions of the structure in addition to tension on the mooring system. Rotational motions are negligible for the given mooring system. The effect of several environmental factors was investigated including variation of water depth and wave conditions. The influence over the tunnel's responses due to structural parameters such as buoyancy to weight ratio and mooring line configuration was also included. Numerical results from two different software, OrcaFlex and CHARM3D, were compared against experimental data published by Oh et al. (2013) to validate the adopted approach. Overall, the numerical results show good agreement with measured data for a variety of wave conditions and structural parameters. Under high energy seas represented by long wave periods and large wave amplitudes, numerical results tend to

deviate from experiments due to various nonlinear effects as discussed in previous sections.

Based on the obtained results, the vertical mooring configuration presents a relatively large dynamic response especially for long wave periods. In this situation, the tunnel acts as an inverted pendulum causing set-down effects. If SFT is installed at deeper submergence depth, the dynamic response becomes smaller since wave action is reduced. At the same submergence depth, as BWR ratio increases so does the surge and heave of the structure. In terms of loading, for mild waves, the relation between wave period and force is almost linear while turning quadratic for high energy seas in case of vertically moored system.

In order to reduce the large translational response of the vertically moored configuration, an inclined mooring system, which can provide lateral stiffness to the SFT structure, was tested. Experimental and numerical results prove that the translational motions are significantly reduced for all the wave conditions considered under this mooring arrangement. In this case, tension at a single mooring line tends to follow a linear variation as wave period and height increase.

The variable C_d formulation depending on flow conditions can improve the simulation results especially for high energy waves, for which the velocity of the structure is significant, thus drag force plays an important role.

Overall, the submerged floating tunnel is a feasible concept and valuable information for the future development of this technology has been presented. Further analysis including hydro-elastic theory including fatigue, VIV in coexisting current and

snap loads in tethers is needed to provide a complete set of data for the successful design and construction of a SFT structure.

6. SHIELDING EFFECT ON NETS UNDER STEADY CURRENT[۞]

6.1 Introduction

As previously presented, the calculation of force and deformation over highly flexible structures is a challenging task. A simple representation using an array of cylinders can predict forces with high accuracy for small deformations occurring at low current speeds. As current speed increases, the reduction of speed inside the cage starts to play an important role in the computations. To be effective, a numerical scheme must be able to account for shielding effect, especially at higher current speeds (DeCew et al., 2013).

Early work on wake modeling proposed an empirical formulation to estimate velocity reduction on net panels, based on momentum considerations and experimental data (Aarnes and Loland, 1990). Recent work based on PIV and ADV laboratory tests, fully defined the velocity field around net panels, and shows that downstream velocity is up to 80 to 90 % of the upstream velocity, depending on solidity ratio (Bi et al., 2013). These findings have been confirmed using field data (DeCew et al., 2013).

In this study, wake models developed for riser interaction are applied to a single cage under steady current. The objective is to find an appropriate model to include

---

[۞] Part of this section is reprinted with permission from "Numerical simulation of wake effect in nets under steady current" by Cifuentes and Kim 2015. Proceeding of the ASME 2015 34th International Conference on Ocean, Offshore and Arctic Engineering OMAE2015, St. John's, Newfoundland, Canada. Copyright © 2015 by ASME.

shielding effect on the present numerical model and improve the actual calculations for force and deformations.

6.2 Wake models for riser interaction

Wake effect is also of interest in riser engineering. In FPSO and TLP platforms, interaction between risers can lead to clashing. Models have been developed to account for shielding effect and its influence on forces and deflection on risers. Thus, the application of these semi empirical formulations seems to fit the calculation of forces on nets, considering that the net itself is treated as an array of cylinder in the numerical model. In this study, three wake formulations are used. Even though developed for 2D application, their applicability in 3D has been validated through experiments (Wu et al., 2008). These wake models include the effect over drag force (Huse, 1993) as well as over the lift force which tends to pull the cylinder towards the center of the wake (Blevins, 2005). A previous study showed that Blevins model is well suited to the analysis of shielding effect on nets (Endresen et al., 2013).

The present work intends to evaluate the accuracy of wake formulations available for riser interaction, and compare their performance against experimental data obtained by Lader and Enerhaug (2005) presented in section 4.

In the present study two wake models are considered. Both are applied in riser arrays design and will be identified as Huse (Huse, 1993) and Blevins (Blevins, 2005) models. A third model is implemented by modifying the original parameters in Blevins model following the work by Huse.

6.2.1 Huse model

This analytical formulation is based on the theory of turbulent wakes together with momentum considerations. It was derived to calculate current forces on array of cylinders where the distance between them is significantly large compared to cylinder diameter (Huse, 1993). When considering the small diameter of the twines on the net compared to the distance between them from the upstream to the downstream portion of the net, the base assumption of this model is satisfied.

Velocity reduction is calculated, thus drag force calculation includes shielding effect; though, wake lift force is not included in the calculations (Orcina, 2014). The wake velocity at the downstream cylinders is determined by the RMS summation of all the cylinders at the upstream positions. This wake model is mathematically defined as follows.

$$\begin{aligned} v_d(x,y) &= v_{do}(x,y) - k_2 v_{uo}[C_{du} d_u / x_s]^{1/2} \exp[-k_3 (y/b)^2] \\ x_s &= x + 4d_u / C_{du} \\ b &= k_1 [C_{du} d_u x_s]^{1/2} \end{aligned} \tag{6.1}$$

Variables are defined: *(x,y)* represents the position of the downstream cylinder with respect to the upstream cylinder, v_d disturbed fluid velocity at downstream position *(x,y)*, v_{do} undisturbed fluid velocity at *(x,y)*, v_{uo} undisturbed fluid velocity at the upstream cylinder center, C_{du} drag coefficient for the upstream cylinder, d_u upstream cylinder diameter. Non-dimensional model parameters k_1, k_2 and k_3 have values of 0.25, 1.0 and 0.693[1] respectively (Huse, 1996).

[1] Parameter k_3 is misprinted in the original paper as 0.639 and was corrected on a later paper.

6.2.2 Blevins model

This semi empirical model determine the drag and lift coefficient of a downstream cylinder based on the spacing between cylinders, upstream cylinder drag coefficient and diameter (Blevins, 2005). As with Huse model, it was derived under the assumption that an upstream cylinder is not affected by a downstream cylinder when the distance between them is larger than 3 times the diameter. It was derived for 2D applications; nonetheless, it can be applied to 3D cylinder arrays (Wu et al., 2008). The details of the model for reduced velocity, disturbed drag and lift coefficients are presented.

$$U(x,y) = U_0\left(1 - 1.2\left(\frac{C_{Duo}d_u}{x}\right)^{1/2}\right)\exp\left[\frac{-13y^2}{C_{Duo}d_u x}\right] \tag{6.2}$$

$$C_{Dd}(x,y) = C_{Ddo}\left(1 - a_1\left(\frac{C_{Duo}d_u}{x}\right)^{1/2} m\right)^2 \tag{6.3}$$

$$\begin{aligned} C_{Ld} &= a_3\left(\frac{yC_{Ddo}d_d}{xC_{Duo}d_u}\right)\left(\frac{C_{Duo}d_u}{x}\right)^{1/2}\left(1 - a_1\left(\frac{C_{Duo}d_u}{x}\right)^{1/2} m\right)m \\ m &= \exp\left[-\frac{a_2 y^2}{C_{Duo}d_u x}\right] \end{aligned} \tag{6.4}$$

In the previous equations U_0 represents undisturbed velocity, U downstream velocity, C_{Dd} represents downstream cylinder drag coefficient calculated using undisturbed velocity, C_{Ddo} downstream cylinder drag coefficient based on reduced velocity, C_{Duo} upstream drag coefficient, C_{Ld} is the lift coefficient at the downstream cylinder, d_u and d_d are upstream and downstream cylinder diameters. Parameters a_1, a_2

and a_3 are constant values obtained after the formulation was fitted to experimental data. Their numerical values are 1.0, 4.5 and -10.6 respectively.

The structure of the wake behind a cylinder under current is defined in Figure 6.1.

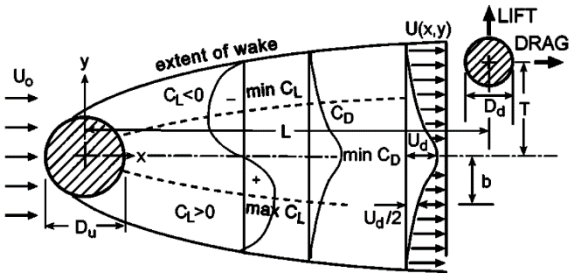

Figure 6.1 Blevins wake model (Blevins, 2005)

6.2.3 Modified Blevins model

A modification of Blevins model has also been considered in the calculations. Huse (1993) used a similar approach to Equation (6.2); however, he proposed a variation of the parameters as follows, $a_1=1.0$, $a_2=11.8$ and $a_3=-1.0$. This alternative has also been studied.

6.3 Numerical implementation of wake models

Numerical models for the reduction of velocity behind a cylinder were developed considering only a couple of long cylinders under flow normal to their axes. In real applications, a cylinder could be in the wake of more than one cylinder and move inside the fluid.

In order to apply these 2D models in OrcaFlex, and account for 3D effects, the following procedure is followed as described by Wu et al. (2008). First, a wake frame of reference is assigned to all the elements located at the wake generating zone. The origin is placed at the center of the element with the x axis parallel to the current velocity vector and y axis orthogonal to the plane formed by the element axial direction and current velocity vector. z is then assigned by considering a right-handed coordinate system. This coordinate system is illustrated in Figure 6.2. By using this coordinate system, the location (x,y,z) of each downstream element is calculated relative to all upstream net elements. The x and y components are then used as inputs for the selected wake model. The z coordinate is used to discriminate the extent of wake effects on downstream elements. A scale factor of 1 is applied to either C_{Dd} or v_d when z is small, this factor gradually goes to 0 as z becomes larger beyond the length of the upstream element.

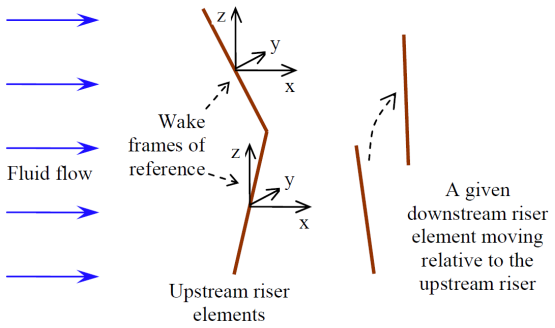

Figure 6.2 Wake frame of reference (Wu et al., 2008)

Once the wake effect from all the upstream elements over a particular downstream component has been calculated, only the largest scaled wake effect is then applied. The procedure is then repeated for each element. Experimental validation of this method can be found in the work by Blevins and Wu (2007).

6.3.1 Wake implementation in cages

In Figure 6.3, a top view of the net shows the sections generating and reacting to the wake effect. The net was divided through a vertical plane perpendicular to the direction of the current speed. The upstream section's elements at the left generate the wake while the elements on the downstream section react to the generated wake.

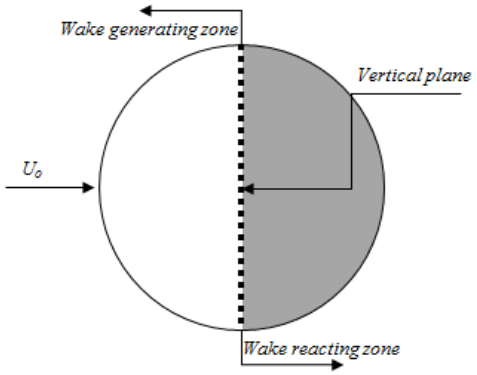

Figure 6.3 Wake zone and vertical plane definition U_o represents undisturbed current velocity.

6.4 Application of semi-empirical wake models to a cage under steady current

After the theory of wake models for riser analysis is complete, the next step is to apply these models on the calculation of drag force and deformation of nets under steady

current. To accomplish this task, the same numerical model created in section 4 is used this time applying shielding effect. The results for drag force will be compared against the experimental data by Lader and Enerhaug (2005), the base calculations without including shielding effect and the numerical calculations including shielding effect by Endresen et al. (2013) in FhSim.

Following the same methodology presented in section 4, the equivalent net element density effect is analyzed by using Model A and B and results for volume and area reduction coefficient are presented. At the end, relative values with respect to experimental data are presented to evaluate the accuracy of each wake model helping to establish the validity and accuracy of each model.

6.4.1 Results

Results for drag force, volume and area reduction coefficient are obtained from the numerical calculations once steady state is reached. In this case, this means that after the ramping period where current load is applied, the cage reaches a constant deformation and the drag load time series converges to a stable value. A time series plot is included in Figure 6.5 for model A under ballast condition C_1 at 0.33 m/s current speed using Blevins wake model. The ramping period is considered negative, thus the time series goes from -10 s. up to 50 s. where the value for drag force converges to a single value as expected from a steady current analysis.

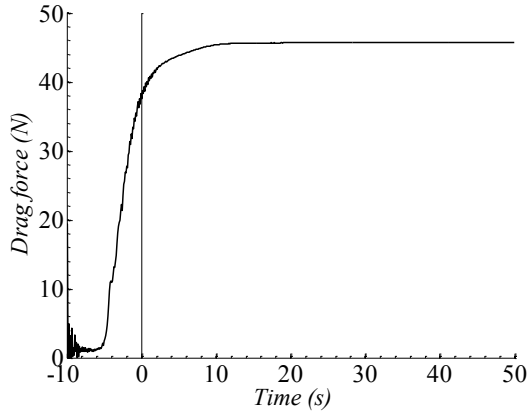

Figure 6.4 Time series of drag load under steady current.

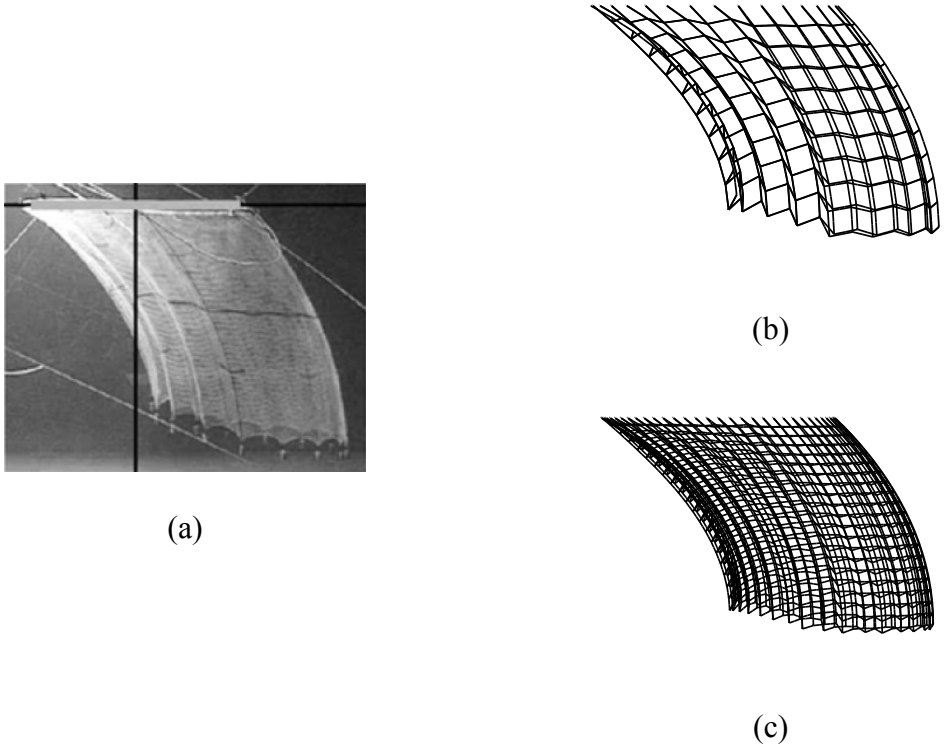

(a)

(b)

(c)

Figure 6.5 Deformation comparison between (a) Experiments (Lader and Enerhaug, 2005), (b) Model A and (c) Model B.

Under this steady state scenario, a direct comparison of deformation between numerical and experimental models is presented in Figure 6.5 for models A and B under C_I at 0.33 m/s current speed using Blevins wake model.

From the figure the effect of correctly modelling the axial stiffness on the global deformation of the cage can be seen. The ballast masses at the bottom of the cage exert a local tension which stretches the net and generates a discontinuity in the radial deformation of the net, particularly in the upstream portion. In the downstream portion, the deformation is less pronounced in the radial direction. This particular deformation pattern is well captured by the numerical model where localized ballast points vertically stretch the netting generating similar radial discontinuities.

The first set of results to be presented considers the drag force over the cage. The three wake models are presented to evaluate accuracy when compared to the base line established in the calculations without wake effect conducted in section 4. Plots are grouped based on ballast conditions to better understand the effect of shielding effect.

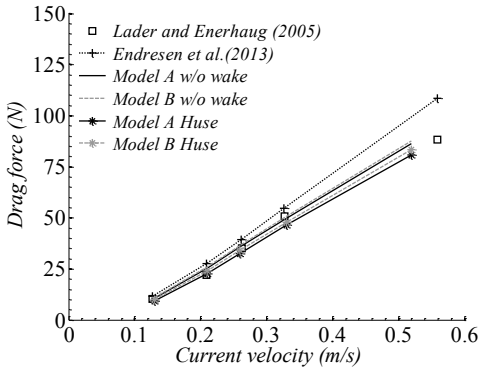

(a)

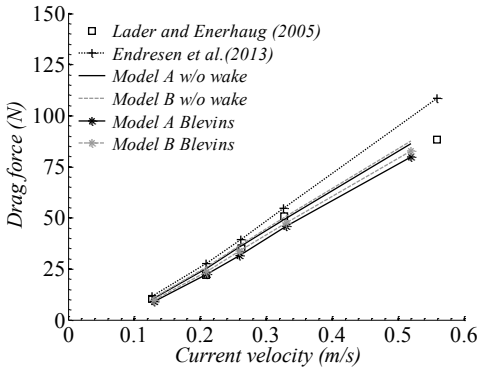

(b)

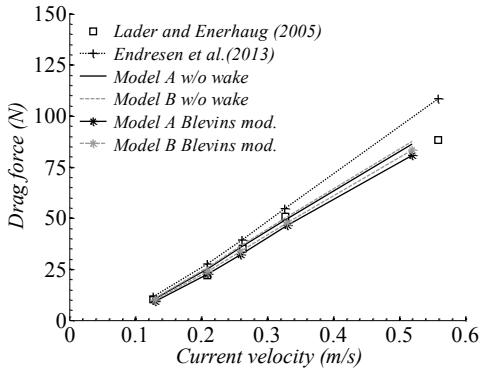

(c)

Figure 6.6 Drag force for C_1 using (a) Huse, (b) Blevins and (c) Blevins modified wake model.

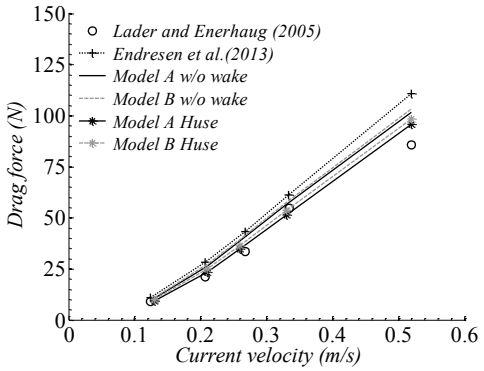

(a)

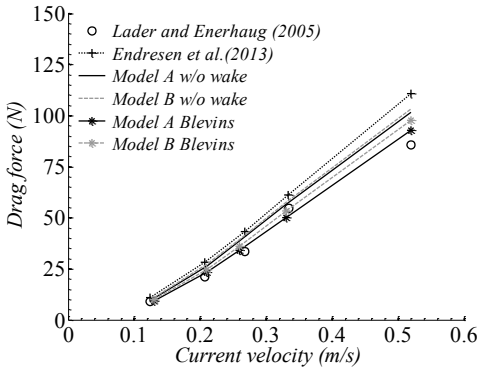

(b)

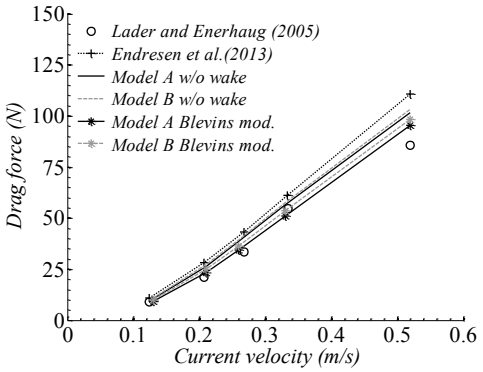

(c)

Figure 6.7 Drag force for C_2 using (a) Huse, (b) Blevins and (c) Blevins modified wake model.

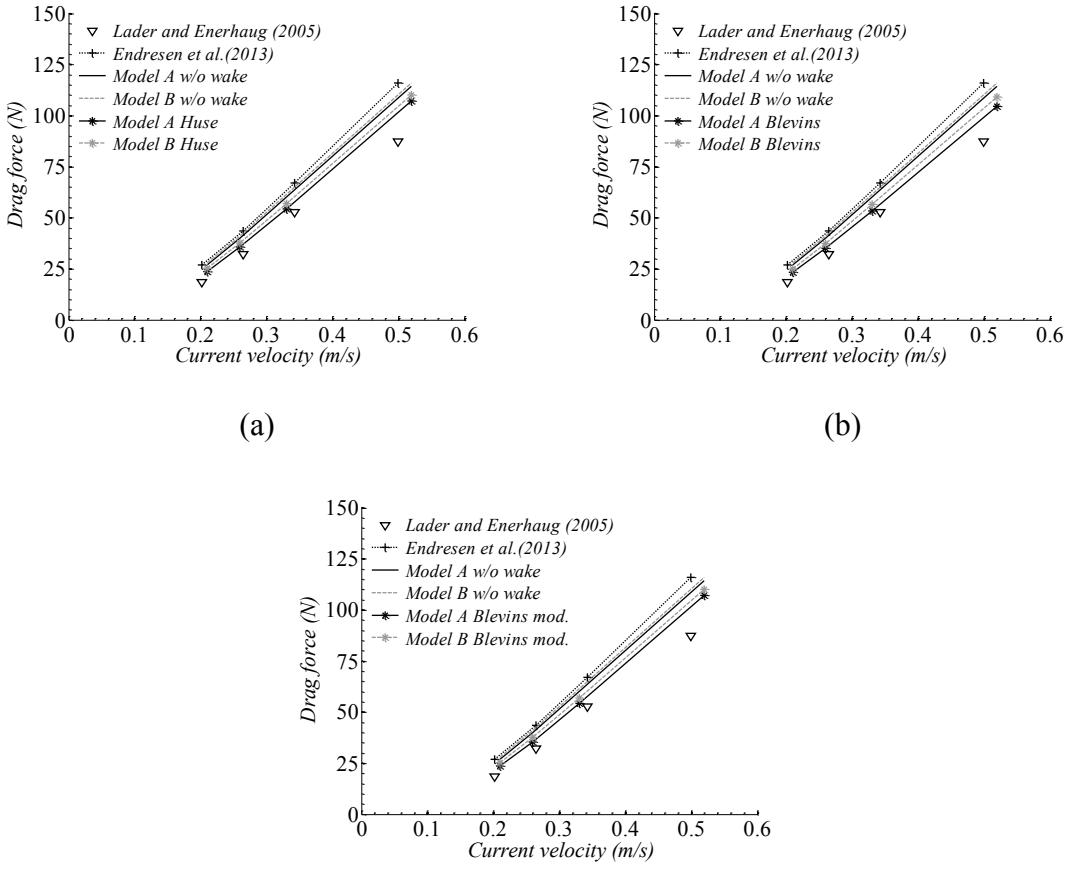

Figure 6.8 Drag force for C_3 using (a) Huse, (b) Blevins and (c) Blevins modified wake model.

Based on the results, the effect of shielding effect over the determination of drag forces is significant. In most cases, the results show a substantial improvement in drag force estimations when shielding effect is included. Further, results for Model B reveal that an increase in the number of elements improves the accuracy of the numerical estimations for C_1; however, its influence is not as significant compared to the effect of wake models. For the other ballast conditions, an increase on the number of elements

does not meaningfully alter the results. The next set of results considers the volume reduction coefficient C_{vr} as defined in Equation 4.7. An accurate prediction of internal available volume helps to identify possible stress induced on the fish when space is substantially reduced. In addition, a large deformation could lead to a clash of mooring elements with the cage leading to failure of components and likely fatigue over time.

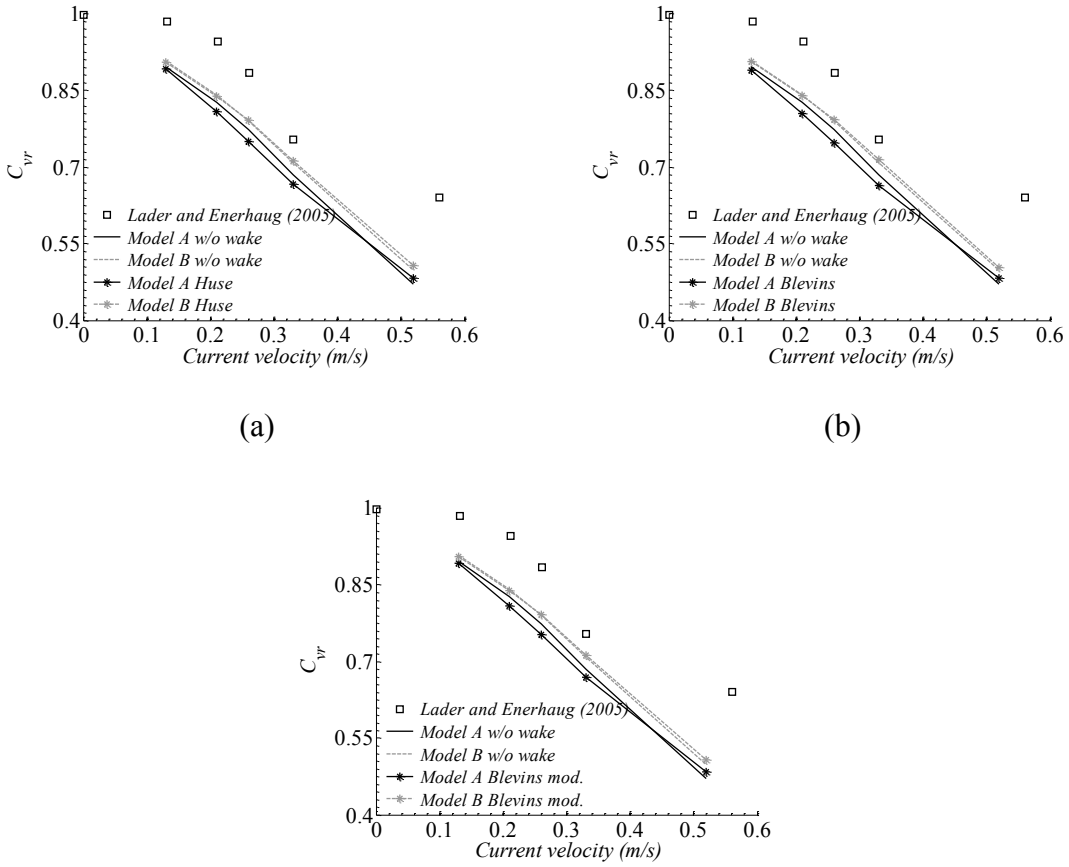

Figure 6.9 Volume reduction coefficient for C_1 using (a) Huse, (b) Blevins and (c) Blevins modified wake model.

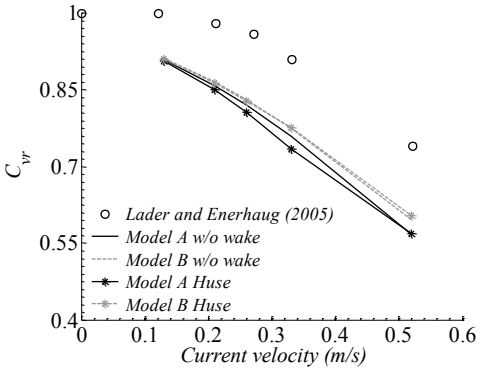

(a)

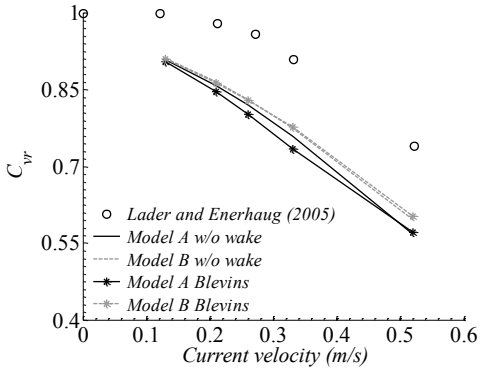

(b)

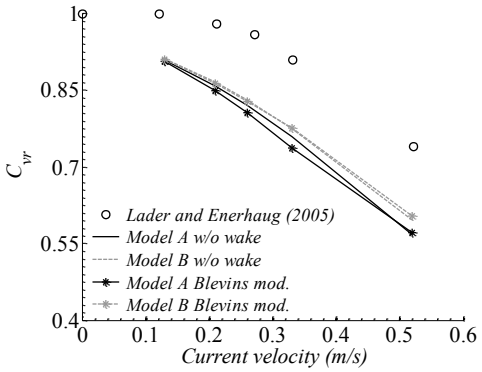

(c)

Figure 6.10 Volume reduction coefficient for C_2 using (a) Huse, (b) Blevins and (c) Blevins modified wake model.

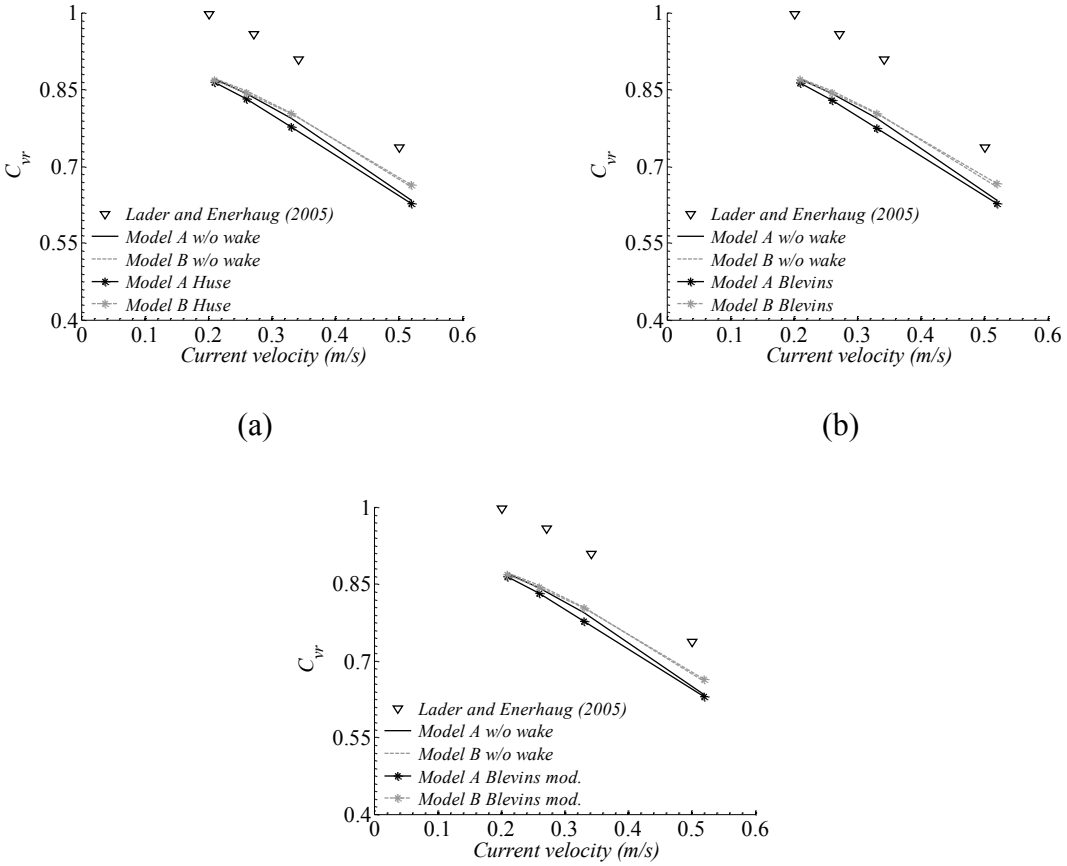

Figure 6.11 Volume reduction coefficient for C_3 using (a) Huse, (b) Blevins and (c) Blevins modified wake model.

For the case of volume reduction calculations, the results show that there is not significant difference when shielding effect is applied. The same holds true for models A and B.

Next the case of central plane area is analyzed. As mentioned before, some empirical formulas use this area to determine drag forces; therefore, its calculation can be useful to obtain a first approximation to drag loads.

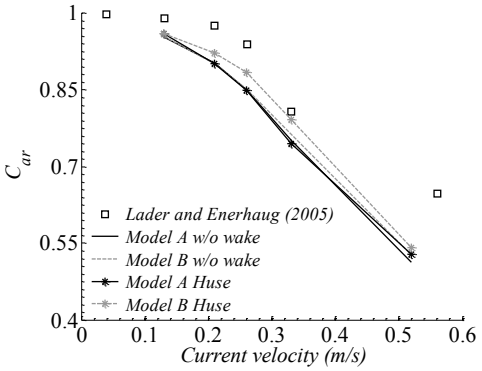

(a)

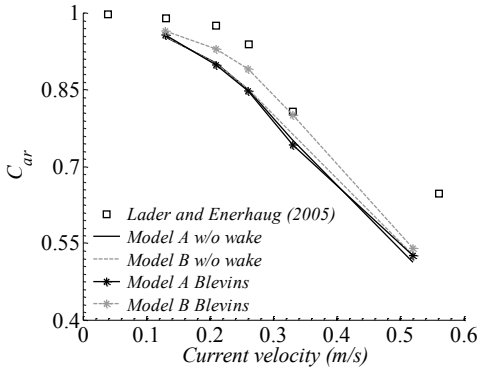

(b)

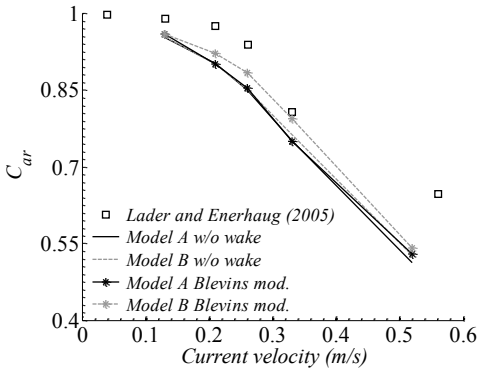

(c)

Figure 6.12 Area reduction coefficient for C_1 using (a) Huse, (b) Blevins and (c) Blevins modified wake model.

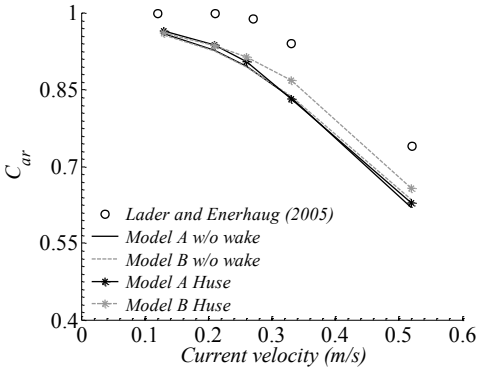

(a)

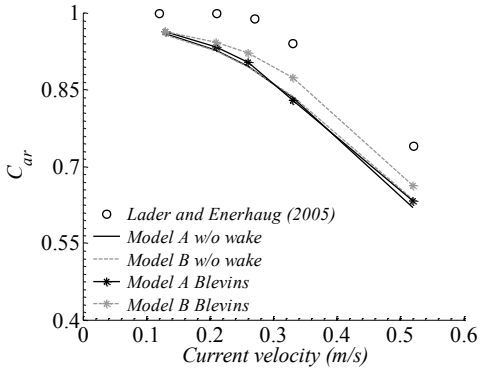

(b)

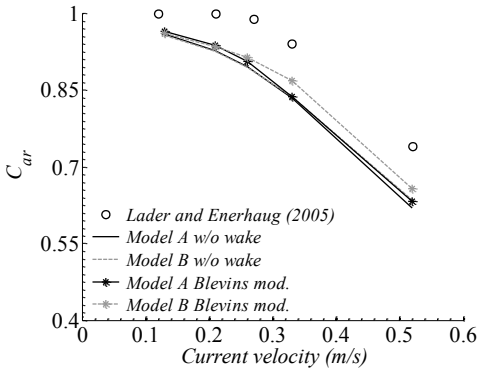

(c)

Figure 6.13 Area reduction coefficient for C_2 using (a) Huse, (b) Blevins and (c) Blevins modified wake model.

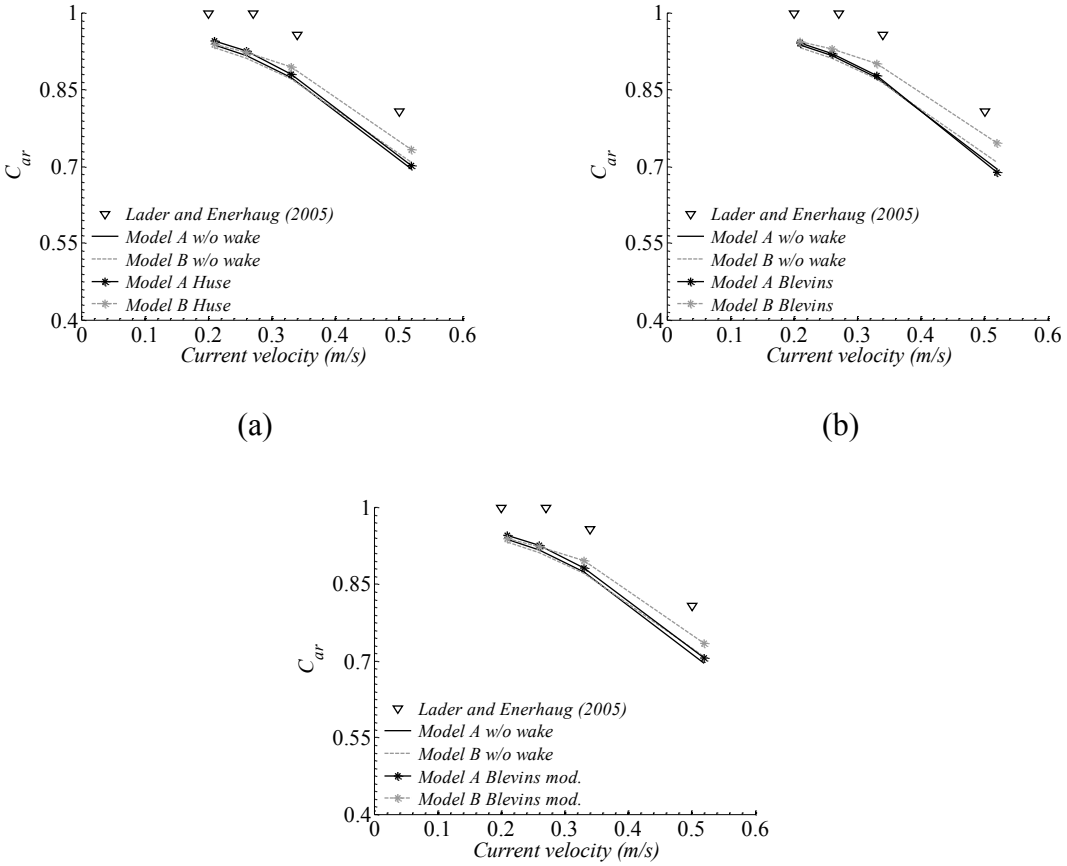

Figure 6.14 Area reduction coefficient for C_3 using (a) Huse, (b) Blevins and (c) Blevins modified wake model.

For the case of central plane area, minor improvements in accuracy can be seen across all models of wake. A 2-3% with respect to the base model without including shielding effect can be seen particularly for Model B.

Overall, the improvement on the results when compared to experimental data is not relevant when deformation is considered; however, higher accuracy is obtained in

drag loads, particularly for mild currents across all ballast conditions. An increase on the number of elements leads to higher accuracy on deformation calculations.

In order to evaluate the performance of each wake model, relative values of the numerical calculations with respect to the experimental data will be presented as described by Equation 6.5.

$$Relative\ error = \left(\frac{Numerical - Experimental}{Experimental} \right) * 100 \tag{6.5}$$

The relative error for drag forces is presented in the next figure. In the following figures, black markers represent Model A while gray markers represent Model B results.

From the relative plots for drag force, it is clear how the addition of shielding effect on the numerical model improves the accuracy of the results. Across all ballast conditions, the relative error gets reduced. Further, the model that shows the best fit when compared to experimental data is Blevins interference model. However, the differences between models are small as seen in the following table.

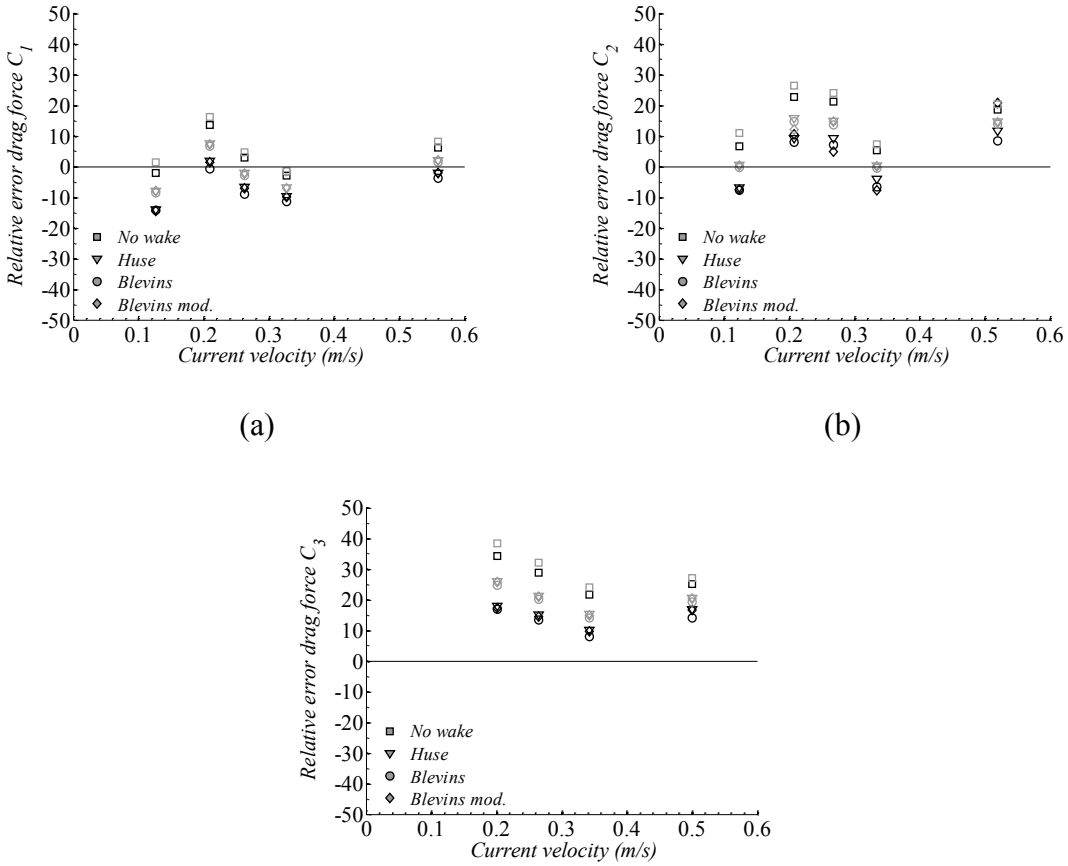

Figure 6.15 Relative error for drag forces (a) C_1, (b) C_2 and (c) C_3.

The complex response of the netting to the current loading can be observed from the differences on results across ballast conditions. It is important to notice that a linear axial stiffness is considered in the simulations. Simulations are focused on the effect of flow velocity reduction inside the cage and current speed over total drag load.

Table 6.1 Average error for drag force

	No wake		Huse		Blevins		Blevins mod.	
	A	**B**	**A**	**B**	**A**	**B**	**A**	**B**
C_1	3.57	5.77	-6.08	-1.46	-7.80	-1.06	-6.45	-1.62
C_2	14.93	17.79	3.86	9.21	1.83	8.25	4.24	8.29
C_3	27.43	30.40	15.02	20.75	13.03	19.57	14.43	20.52

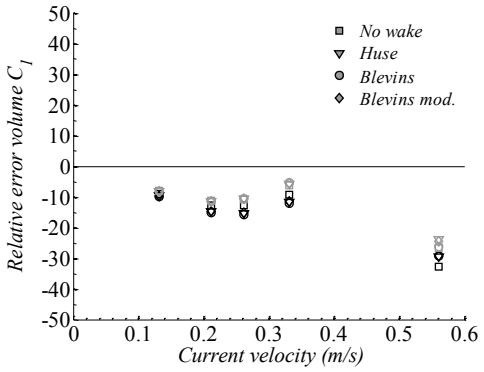

(a)

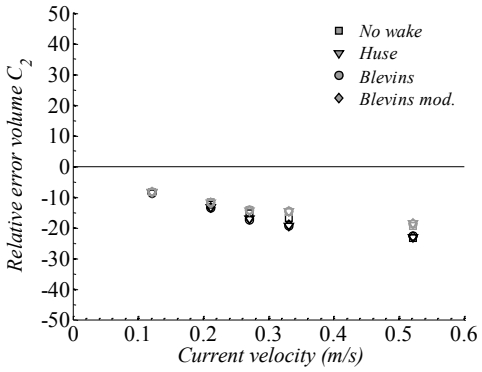

(b)

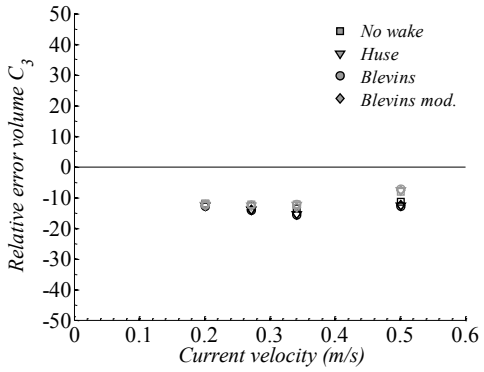

(c)

Figure 6.16 Relative error for volume (a) C_1, (b) C_2 and (c) C_3.

Axial stiffness of the material also plays a role on drag force. For small strains, the stress-strain relation is linear; yet, for large strain, the relation can be fitted to a third order polynomial (Moe et al., 2007). This variation of Young modulus induces uncertainty in the model, particularly for the heaviest ballast condition.

In terms of volume reduction, shielding effect does not significantly change the results. In fact, the results simply confirm that by using more elements to model the cage, closer agreement is reached.

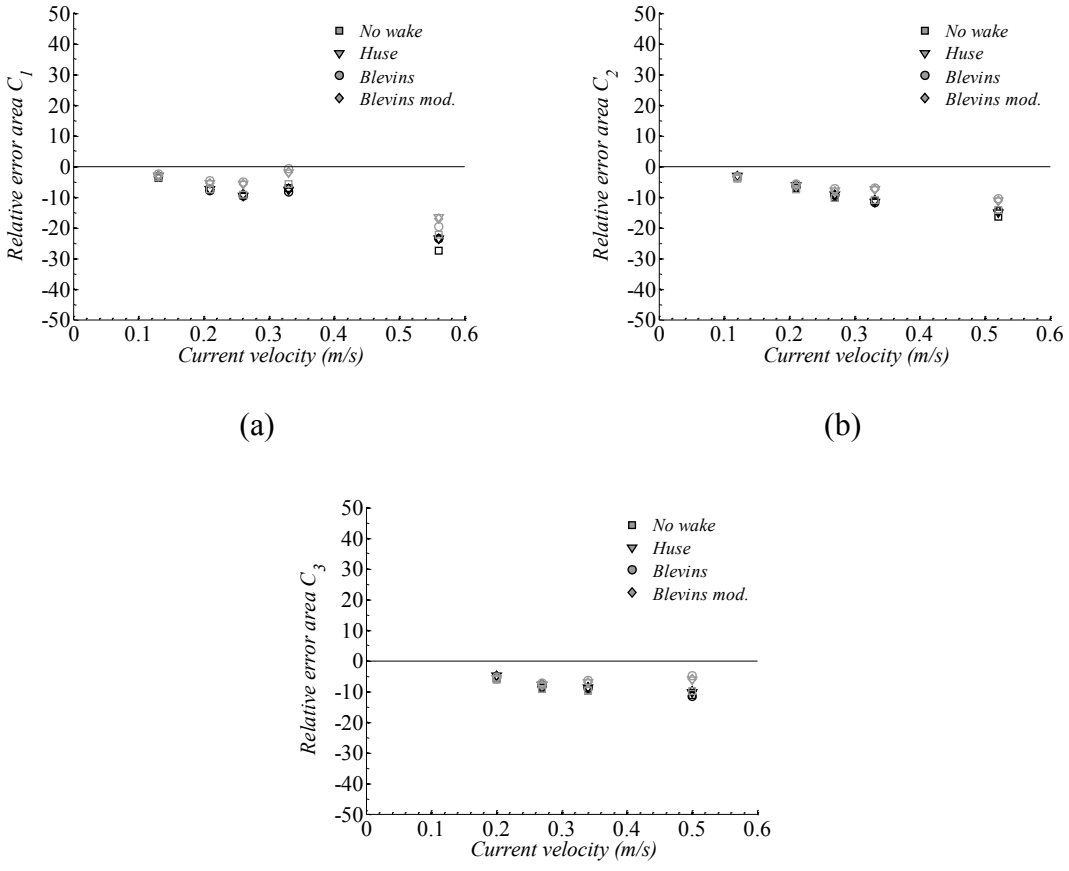

Figure 6.17 Relative error for area (a) C_1, (b) C_2 and (c) C_3.

The area reduction of the central plane results do not change as shielding effect is included. This can be explained by the fact that this plane is the division between the wake generating and reacting zone, thus this boundary is not directly impacted by shielding effect.

6.5 Discussion

Considering the base results for the drag load and deformation over a cage structure, it was evident that the reduction of the velocity inside the cage due to the interaction of the flow with the net needs to be included. This effect was accounted for using interaction models developed for risers, which have given good results when the distance between cylinders is larger than 2 to 3 times the diameter of the cylinders. Being this the case for the numerical model of the cage, it is considered appropriate to use these models to evaluate its effect over the load and deformations of the cage.

The influence of shielding effect over viscous drag is significant and can clearly be seen in the plots using the relative error based on lab measurements. Improvement of up to a 12% is reached compared to the base model without shielding effect. As for volume and area reduction, the improvement is smaller and reached up to a 4%.

Based on the analysis of the different wake models applied on this research, the minimum error was achieved by using Blevins formulation. Overall, by using this interference model, the results for drag force, volume and area reduction show the smaller deviation from experiments among the three studied models. However, the differences between wake models are not significant and it is evident that, using this

particular lumped mass scheme, either Blevins or Huse wake models can be used when calculating forces and deformations over nets. In fact, based on the results, we can conclude that the lift effect described by Blevins model is not important in the wake of a net structure. This can be explained given that the span of the threads of a net are short and connected to buoys at its ends, which restricts its displacement, thus the line elements do not have a high deformation towards the center of the opening enclosed by four threads. In terms of computational time, Huse model is more efficient and its reliability is proven based on the results. Still, the time step required when wake models are used is small, especially when the number of elements is increased.

Considering the previous results, there are still uncertainties in the numerical model. One of them is the effect of the nonlinear structural behavior of the netting material which is not included. Another effect deals with the variation of flow direction around and below the cage. This change of direction cannot be included in a simple Morison force model, and its effect is yet to be fully understood based on current literature. In order to improve the accuracy of the numerical results, more details about the characteristics of the flow inside and outside the cage are needed, particularly for high current speed and high deformation of the cage.

7. DRAG COEFFICIENT FORMULATION FOR HIGH SOLITY RATIO NETS

7.1 Introduction

Up to this point, a single netting material under mild current conditions has been analyzed. Under the studied conditions, an effective numerical methodology has been implemented including a variable drag coefficient formulation and the addition of shielding effect on the cage. Across all the studies, it is clear that for high energy flows that generate large deformations on the net, numerical results tend to deviate from experimental data even when shielding effect is included. This leads to the conclusion that another effect must be included in the analysis. This effect is defined as blockage of the flow. At high current speed, the deformation of the cage is significant. The cage will react to the flow closer to a solid body than to a porous membrane. At this point the flow, instead of going through the netting, deviates and flows below and around the cage (Gansel et al., 2012). At the same time, a reduction of the drag force when compared to the same cage at undeformed condition is observed (Kristiansen et al., 2015). This blockage is even more significant for nets with high solidity ratios which experience changes on the direction of the flow even at mild current speeds (Moe-Føre et al., 2014).

Most common netting materials used in industry today have a solidity ratio that ranges between 0.20 and 0.30; yet even higher solidities can be found. In addition, biofouling naturally increases S_n values, therefore, a numerical model must be able to accurately describe forces when blockage is significant (Norway Standard, 2009).

Nowadays, numerical models for nets fail to accurately describe forces when blockage effect is significant, thus opportunities for further research exist.

In the present Morison force model using a lumped mass element, the changes on the direction of the flow are not included. In order to include this effect, the free parameter in the model, drag coefficient, can be tuned to represent blockage effect.

In this work a new formulation for C_d is presented based on published experimental work and numerical simulations carried out using OrcaFlex. The formulation is defined for Raschel nets due to its large application on installed fish farms. Nevertheless; a similar approach can be applied to other netting materials following the procedure introduced in this study. This hybrid model defines C_d as a function of Re and solidity ratio (S_n) of the net. Previously, C_d was defined only using flow and net threads characteristics, now net geometry is included. In this manner the blockage effect due to high solidities and high current speed can be accounted for when using a Morison force definition. This new methodology significantly improves the numerical results when compared to experimental published data considering a wide range of current velocity and S_n values.

7.2 Drag force calculations for high S_n nets using DeCew et al. (2010) formulation

Once the modeling of a single cage including a variable drag coefficient formulation and shielding effect was completed and validated, a more complete set of experiments was needed to cover a wider range of net characteristics and flow regimes. In addition to the experimental data presented by Lader and Enerhaug (2005), the results

presented by Moe-Føre et al. (2014) are used as the basis for the next analysis. In the later work, numerical end experimental data for large solidity ratios and current speed are presented. The objective of the study was to evaluate the accuracy of different numerical models. Overall, three methods were analyzed, triangle, truss and spring element models. All of them over predict loads at high current speeds. Constant C_d values were used in their study including wake effect. In order to evaluate the performance of the present numerical model, the same characteristics of the net, cage and flow were replicated.

7.2.1 Experiment conditions and net characteristics

In both experimental studies, Lader and Enerhaug (2005) and Moe-Føre et al. (2014), a Raschel type net was used to build a cylindrical cage open at top and bottom. A simple ballast system, including point masses at 16 points along the bottom of the cage was used. As previously mentioned, this type of experiments is suitable for validation of numerical models. In these experiments, the surface collar is treated as a rigid body. The drag over the net was isolated by extracting the drag force of the upper collar and ballast cylinders from the total drag force over the cage.

Figure 7.1 Raschel netting (Kristiansen and Faltinsen, 2012)

In the case of the experiment by Lader and Enerhaug (2005), the net pen has a diameter of 1.435 m. and a draft of 1.44 m. The density of the net is 1130 kg/m^3. For ballast, 16 point masses of 400 gr. each were hanging from the bottom of the net pen. On the experiments by Moe-Føre et al. (2014), the diameter of the cage is 1.75 m. and draft 1.5 m. The density of the net material is 1100 kg/m^3 and ballast is applied at 16 points along the circumference of the net bottom with a wet weight of 4.48 N. The description of the netting geometry is presented in Table 7.1. For S_n equal to 0.1904 and 0.3020, the diameter of the twine has been modified from the original physical value to account for the projected area of knots connecting twines. In both cases, the net geometry is the same as the intended full scale netting. This helps to avoid small *Re* values on the model and prevents differences between flow regimes at model and prototype scales.

Table 7.1 Netting characteristics

Solidity ratio S_n	Bar length (mm)	Twine diameter (mm)
0.1904	25.5	2.60
0.2250	16.0	1.80
0.3020	16.2	2.66
0.4340	5.8	1.35

Three cages tested in this analysis were subjected to a current speed ranging from 0.03 to 0.93 m/s. For each case the current speed is considered constant over water depth. For the case of S_n equal to 0.2250, the maximum current speed for calculations is 0.52 m/s.

7.2.2 Numerical models

The model considering a S_n value of 0.2250 corresponds to the same model used in the previous sections under ballast conditions C_1. In this case, and based on the conclusion that the increase on the number of elements used in the numerical model does not significantly improves drag force calculations, Model A is used (10 rings, 32 edges). For the cases corresponding to the experiment by Moe-Føre et al. (2014), the same discretization of the net was used meaning that the model consists of 320 three degree of freedom buoys and 672 lines in addition to 32 six degree of freedom buoys used for the surface collar. Figure 7.2 shows the numerical net including lines and buoys.

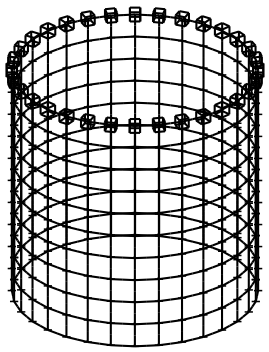

Figure 7.2 Numerical representation cage used by Moe-Føre et al. (2014)

In the numerical model, Blevins wake model was applied following the findings in the previous sections. As for the drag coefficient, the formulation presented by DeCew et al. (2010) is used which is described by Equation 4.5.

Figure 7.3 shows the high deformation of the net for S_n equal to 0.3020 under 0.5 m/s current speed.

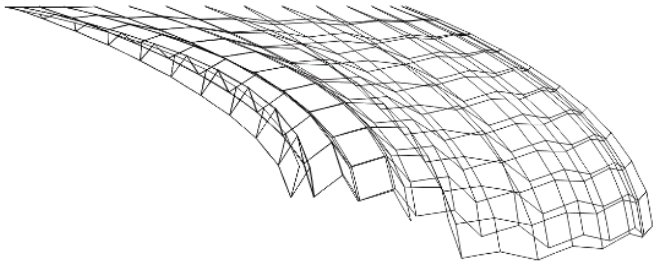

Figure 7.3 Net deformation

7.2.3 Drag force results using C_d formulation by DeCew et al. (2010)

In order to check the accuracy of the present numerical scheme, in addition to the experimental data presented in the work by Lader and Enerhaug (2005) and Moe-Føre et al. (2014), the numerical calculations performed by Kristiansen and Faltinsen (2012) using a screen force model are included for comparison. In the analysis using a screen model, the same cages were utilized to validate the model and complete a parametric analysis of the factors that could affect the accuracy on the determination of forces on the net. A drawback of this method is that the mass of the net is not included in the model, meaning that the netting is assumed to be neutrally buoyant which for the present case holds true, but for heavier nets this represents an issue which; on the other hand, can be taken into account in the OrcaFlex model.

In the following plots the label OrcaFlex-DeCew et al. (2010) represents the numerical results obtained using our current model and the drag coefficient definition given by Equation 4.5.

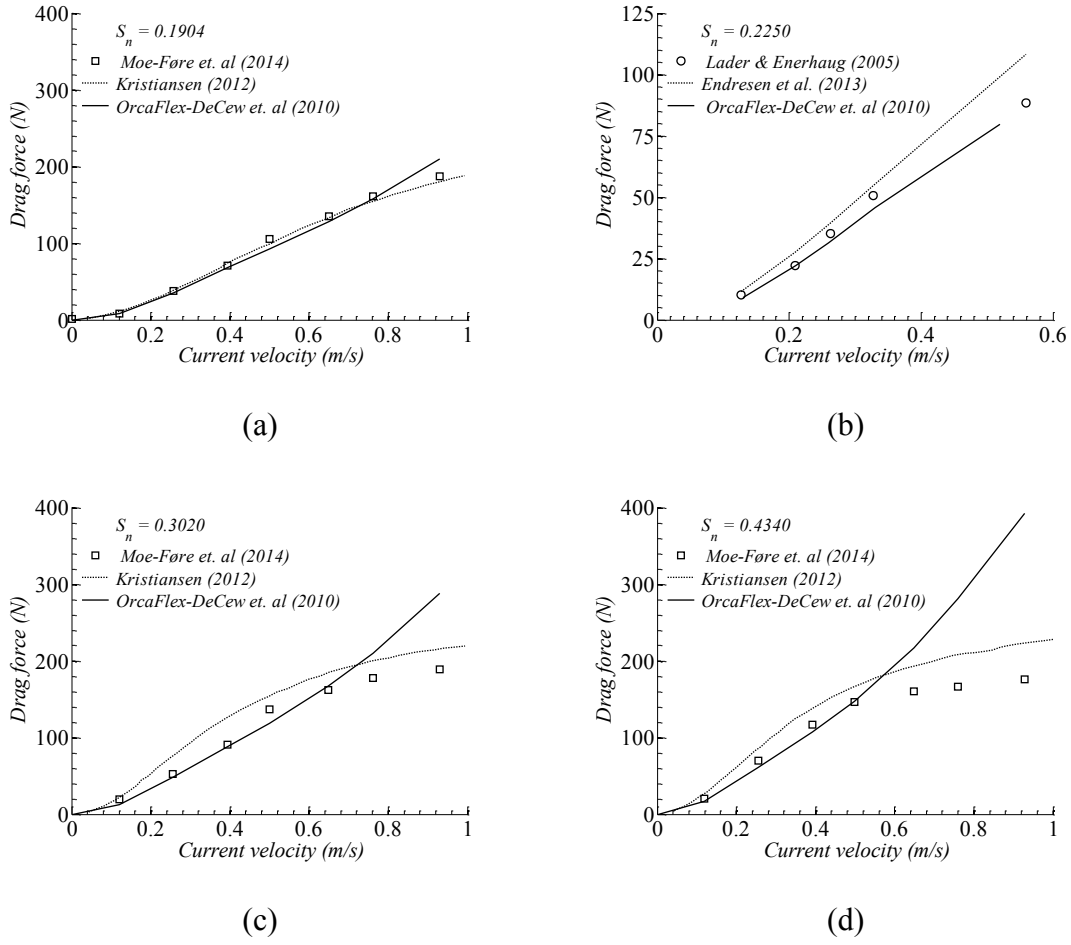

Figure 7.4 Comparison numerical and experimental results for drag force under steady current (a) S_n=0.1904, (a) S_n=0.2205, (a) S_n=0.3020 and (a) S_n=0.4340

By using the methodology previously presented, numerical calculations show a good agreement with experiments over a wide range of current speed especially for S_n values of 0.1904 and 0.225. For higher solidities, good agreement is reached for current speeds up to 0.5 m/s.

Based on the results, the screen model by Kristiansen and Faltinsen (2012) tends to follow the trend of the experimental data; nonetheless, still over predicts the drag load for high current speeds.

From Figure 7.4 it is clear that for high speed and high values of solidity ratio, the difference between the present numerical calculations and experimental data becomes significant. The main reason for this effect is the blockage experienced by the flow when the net is deformed. For high solidity nets, the flow goes around and below the net instead of flowing through it. This phenomenon is translated into the plateau of the drag force versus current speed curves. The deformation and exposed area do not significantly change for high current velocities, thus the slope on the drag force curve changes. This change on the direction of flow cannot be modeled in our numerical model. On the other hand, the blockage effect can be considered into the drag coefficient values for the constituent elements of the numerical net since this value acts as a free parameter in the actual numerical scheme.

Based on the results in Figure 7.4, the C_d formulation by DeCew et al. (2010) cannot directly be used under high current speeds for high values of solidity ratio; a new approach needs to be developed in order to improve the accuracy of the drag load predictions.

7.3 C_d formulation based on experimental and numerical data

By an iterative process, optimal C_d values were determined for the measurements that show the largest deviations from experimental data. Numerical calculations show

that the drag coefficient values for nets of high solidity ratios, under high current speed, must be significantly smaller than those used for nets with smaller S_n under similar current velocities. This drag coefficient reduction takes into account the reduction of flow velocity inside the cage. In the physical net, the current speed affecting the downstream portion of the net is greatly reduced by the blockage from the deformation of the upstream panel (Gansel et al., 2012). This effect can partially be captured by using a local wake model; however, at large deformations, the global wake by the upstream panel overtake the local wake due to the presence of line elements. This global wake effect can be included in our numerical model by the adequate definition of drag coefficient values corresponding to the type of net analyzed and flow conditions.

Since the determination of drag coefficient in this numerical scheme is based on twine diameter, a third source of experimental data can directly be added to the study. In the research performed by Tsukrov et al. (2011), several nets were characterized in terms of drag coefficient by experimental measurements. Net panels were exposed to current speed ranging from 0.1 to 1.0 m/s. In particular, two Raschel type nets were included in Tsukrov et al. (2011) considering S_n values of 0.172 and 0.208.

Reynolds numbers are defined as in Equation (7.1) with U_c equal to current speed, d_{twine} diameter of threads of the netting and ν kinematic viscosity.

$$Re = \frac{U_c d_{twine}}{\nu} \tag{7.1}$$

Drag coefficient as a function of Re for all the data, including experimental and numerical sources, is presented in Figure 7.5. Scatter is induced due to the blockage

effect and no clear trend is revealed as how the variation of drag coefficient can be used to account for the effect of high solidity ratios at high energy flows.

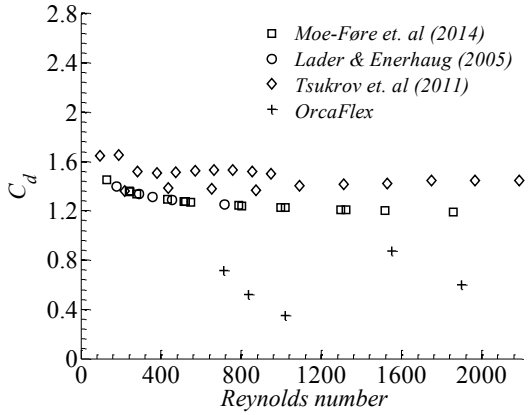

Figure 7.5 C_d as a function of Re based on experimental and numerical data.

Based on Figure 7.5 data from all sources was arranged on a new format. Instead of presenting drag coefficient as a function of Re, C_d now varies as a function of $Re*S_n^2$. By using this new definition, drag coefficient now considers the blockage effect at high solidity ratios and a trend can be observed from the plot in Figure 7.6. As the factor $Re*S_n^2$ increases, the drag coefficient value is almost constant with a mean value of 1.4 up to $Re*S_n^2$ equal to 110. For larger values of the factor $Re*S_n^2$, C_d decreases. This trend is interesting given that the plot is created using four different sources of data, covering a wide range of fluid velocity and solidity ratio. This approach is intended to be valid for nylon Raschel nets, while for other types of nets, a similar approach can be used to characterize the variation of C_d across different net opening geometries and fluid regimes.

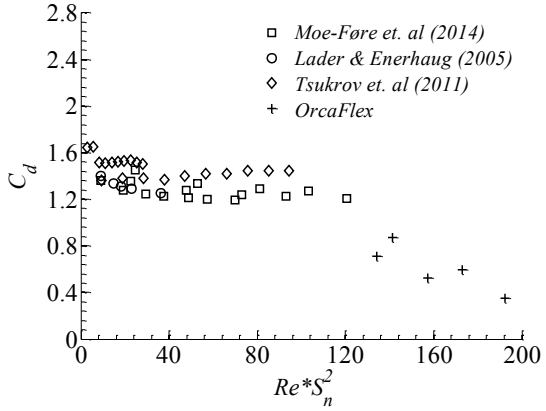

Figure 7.6 C_d as a function of Re and S_n

The data from Figure 7.6 can be described by means of a second order polynomial using a least square method technique. In this manner, a new formulation for C_d values is found, particular to Raschel nets. Reynolds number is calculated based on the twine diameter of the net while S_n values are taken from the experimental published data. This is shown in Figure 7.7.

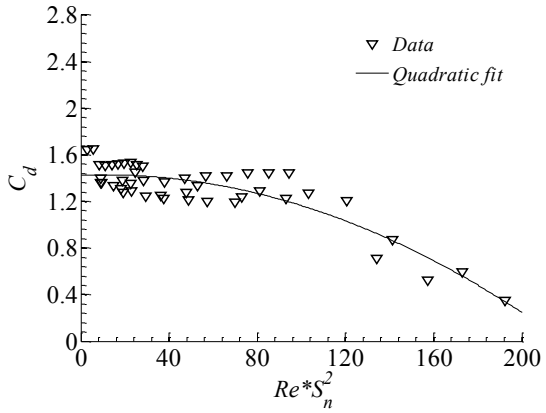

Figure 7.7 C_d as a function of factor $Re*S_n^2$

The new expression for C_d based on the factor $Re^*S_n^2$ is presented in Equation (7.2).

$$C_d = -3.2892x10^{-5}(Re^*S_n^{\,2})^2 + 0.00068^*(Re^*S_n^{\,2}) + 1.4253 \quad (7.2)$$

The R^2 value of the quadratic fit curve is 0.8. This new formulation is implemented into OrcaFlex and the drag force calculations in Figure 7.4 are revised.

7.4 Drag force calculations based on semi-empirical model

In order to evaluate the improvement on the results by applying the formulation based on numerical and experimental data, the results previously presented are updated using the new C_d values obtained by using Equation (7.2).

The results using the upgraded formulation (OrcaFlex-Quad. fit) are presented in Figure 7.8. In these plots the results from Figure 7.4 are included to directly evaluate the level of improvement achieved by characterizing the net using the new expression in Equation (7.2) based on the factor $Re^*S_n^2$.

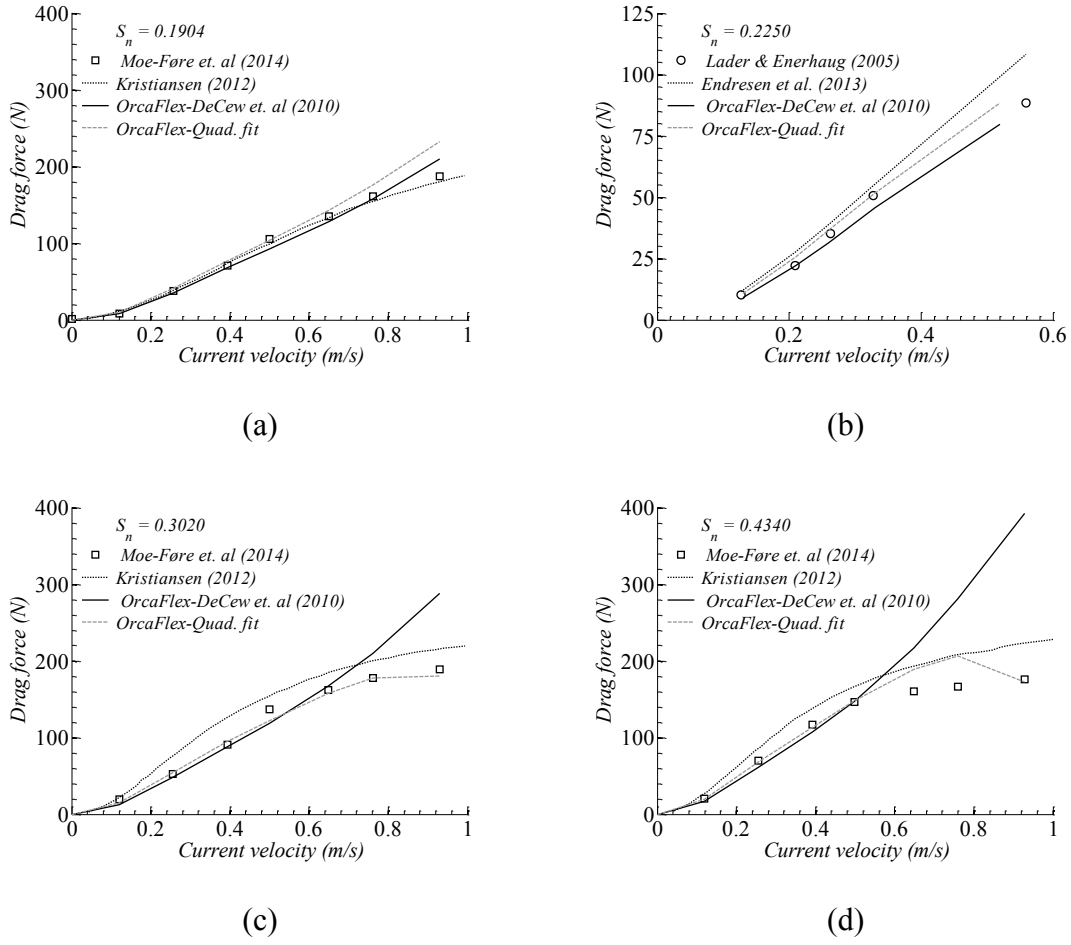

Figure 7.8 Comparison numerical and experimental results for drag force under steady current using new C_d definition (a) S_n=0.1904, (a) S_n=0.2205, (a) S_n=0.3020 and (a) S_n=0.4340

From the previous figure, the accuracy improvement of the numerical results using Equation (7.2) is proven. As a comparison, plots include experimental as well as numerical data using the formulation in Equation (4.5) and the proposed new C_d expression for Raschel nets presented in Equation (7.2), in addition to the numerical results using the screen model. There are small differences for low S_n nets since on these

nets the drag load was already calculated with high precision by using Equation (4.5) and Blevins wake model. On the other hand, for high S_n nets, the improvement on numerical prediction for drag force when compared to experimental data is significant. The results show that a modification of C_d values is a viable alternative to represent the complex blockage effect over a cage in a simple and efficient manner. The fact that experimental data from three different experiments was used in addition to the numerical data, justify the validity of the approach.

When compared to the screen force model, the results using the current method show better results across the spectra of nettings and flow regimes.

This analysis shows that for each particular net, a characterization in terms of drag coefficient is necessary when using a Morison force model. A simple definition of C_d able to cover the complete spectra of nets geometries and flow regimes is not an adequate alternative given the complexity of the hydroelastic response of flexible nets and the substantial differences on geometry and mechanical properties of the various nets in the market.

7.5 Discussion

Estimation of drag force and deformation for highly flexible structures such as nets is a complex hydroelastic problem. As seen from the calculations presented in this work, a Morison model using a traditional definition for drag coefficient is not able to accurately predict forces when flow is deflected due to the presence of the netting. Recent experimental data have confirmed the acceleration of the flow underneath and

around cylindrical cages as well as a significant reduction of flow velocity inside the cage for solidity ratios of 0.3 (Turner and Reid, 2015). This change of direction of the flow and the significant reduction of the current velocity inside the cage at high solidity ratios has not been described in current numerical models. Thus a new formulation to account for this phenomenon is developed.

CFD calculations have revealed the complex flow pattern in the wake of a single net panel (Bi et al., 2014a) as well as on a rigid porous cylinders (Gansel et al., 2012). Even for these simple net models, the computational time required to obtain the results is quite large and not practical for computation of large fish farm facilities compose of multiple cages. On the other hand, a simple model as the one presented in this analysis, is able to converge in a short time using a small number of elements to discretize the net. In addition, for further analysis including waves, the research done in cylinders under waves and current flows can be used to feed the model to include inertia effects particularly for the floating collar which contribution to the total drag force is significant depending on the floater diameter to wave length ratio (Kristiansen and Faltinsen, 2015).

Based on the results, a simple discretization of a net using an array of cylinders connected by buoys, is able to predict drag forces over a large range of current speed and solidity ratios using the new formulation for C_d. Results show that the original formulation using C_d values from DeCew et al. (2010) is suitable for mild current speed and relatively low solidity ratios. Differences are not significant for current speed up to 0.5 m/s across the four nets used in this analysis. Over such current speed, small deviations from experimental results can be observed for the case of S_n equal to 0.1904

and 0.2250. However, for the cases of S_n equal to 0.3020 and 0.4340, maximum differences between experimental and numerical data reach over a 50% and 100% respectively. This can be explained by the fact that in the numerical model the projected area of the model remains constant; all the line elements of the net are subjected to the same current load effect, while on the physical model, the projected area is reduced due to the deformation of the net as seen in Figure 7.3. Under this deformation, the elements on the downstream panel are subjected to a reduced current speed which is related to the blockage created by the deformed upstream panel, and is more significant than the reduction given by the presence of the upstream elements represented by the local wake. One method to include this reduction on projected area and current speed on the netting is to modify the free parameter in our model which corresponds to the drag coefficient. The new formulation in Equation (7.2) shows a significant improvement on accuracy on the determination of drag forces over a wide range of S_n values and flow velocities. The fact than three different sources of experimental data were used to derived the formulation for Raschel nets support the validity of the new method to characterize nets in terms of drag coefficient for large deformations.

The determination of drag forces over nets with high solidity ratios is particularly interesting for fish farms exposed to high levels of biofouling. Recent studies have shown that levels of biofouling can be parametrized in order to use the existent method of calculation of forces over nets (Gansel et al., 2015). By using the new formulation, calculations can be done to determine the drag loads over fish farms after being installed, and using this information, the cleaning or replacement of nets can be schedule,

facilitating the operations. This prediction of forces over biofouled nets can also help to avoid failures that are translated into escapes of farmed fish into the wilderness.

In addition, the current methodology can be used for other types of nets, e.g. cupper-nickel and Dyneema fibers; thus, increasing the accuracy on the determination of forces and improving the design of station keeping systems.

8. FORCES ON CAGES UNDER COMBINED CURRENT AND REGULAR WAVES

8.1 Introduction

Once the present numerical methodology was validated for a wide range of current speed and S_n values, the next step in the analysis is including wave loading. In previous cases, the netting was the solely focus of attention. The surface collar has been considered up to this point as a rigid body. In addition, its drag load has not been included in the calculation. Nevertheless, in waves, the surface collar stands most of the wave loading and its deformation is crucial when estimations of mooring tension are needed.

Under wave loading, a cage using a rigid collar will follow the wave elevation at low wave frequencies. Further, a linear relation can be seen between wave elevation, mooring line tension, surge and heave motion for frequencies up to 1.0 Hz (Dong et al., 2010). For high wave frequencies, negligible motion is observed and high damping is present in the system (Xu et al., 2011). Under wave excitation, studies regarding the dynamic response of the floating collar have shown the relevant effect of the flexural modes over the global response of the cage (Endresen, 2011; Faltinsen et al., 2011). For the whole cage system, mooring line forces are strongly dependent on wave elevation, while volume reduction is driven by current loading. As for the surface collar, large deformations are expected due to the low bending stiffness of the HDPE material typically used (Li et al., 2013a). Another component of the response of the floating collar is the variable buoyancy force due to the constant piercing of the floater on the

water surface (Li et al., 2013b). Modeling of bending and axial stiffness of floater and netting, in addition to the approximation of wave kinematics up to the instantaneous free surface are critical, given the significant effect of these parameters on the tension force on mooring lines (Kristiansen and Faltinsen, 2015).

In the present section, a single cage considering a flexible surface collar, netting, ballast and mooring system is exposed to a combination of current and regular waves. The cage is open at the top and bottom to simplify the dynamic analysis. Particular attention is given to the drag and inertia coefficient selection for the upper collar, which depends on the wave condition characterized by Keulegan-Carpenter *(KC)* and Reynolds *(Re)* numbers. The definition of drag coefficient for the net is based on the formulation developed in the previous section. An analysis of the different models for wave kinematics extrapolation over the sea surface is carried out since no information is available about the influence of these approximations on the total loads over the system.

The results obtained are contrasted with the experimental data presented by Kristiansen and Faltinsen (2015). Based on numerical results, mooring line tension can be well captured by the present Morison force model for a wide range of wave steepness and current speed. Overall, for regular wave loading, the predominant effect over tension is viscous drag over wave loading, except for steep waves where wave loading is of the same order of magnitude as current force.

8.2 Numerical model of cage and steady current calculation

To validate the present numerical model, experimental results presented by Kristiansen and Faltinsen (2015) were used. In their study, wave and current loads over a single cage were determined based on experimental and numerical calculations. In addition, a study was carried out to evaluate the influence of several parameters over the dynamic response of the cage. The cage is composed of a floating collar, netting, mooring lines and ballast represented by 16 point masses along the bottom circumference of the cage. The present validation was carried out using the experiment conditions to avoid scale effects. The particulars of the model are described in Table 8.1. The numerical model was built using 2624 lines, 1280 three degree of freedom buoys and 64 six degree of freedom buoys. Numerical model including cage and mooring lines is presented in Figure 8.1.

The simplest case considers only current load for velocities between 0.04 to 0.30 m/s. The current profile is idealized as constant over water depth. The results for this current only case are included for completeness of the analysis. In this case, Blevins wake model has been included and drag coefficient is defined using the new formulation presented in section 7 given that the model uses Raschel type netting.

Table 8.1 Cage characteristics

Parameter	Value	Unit
Diameter	1.5	(m)
Draft	1.3	(m)
Floater pipe diameter	0.03	(m)
Floater bending stiffness	0.136	(Nm^2)
Net type	Raschel knotless	~
Solidity ratio (S_n)	0.265	~
Bar length	6	(mm)
Twine diameter	0.6	(mm)
Net density	1100	(kg/m^3)
Ballast	16 x 0.075	(kg)
Water depth	1.5	(m)
Scale	1:25	~

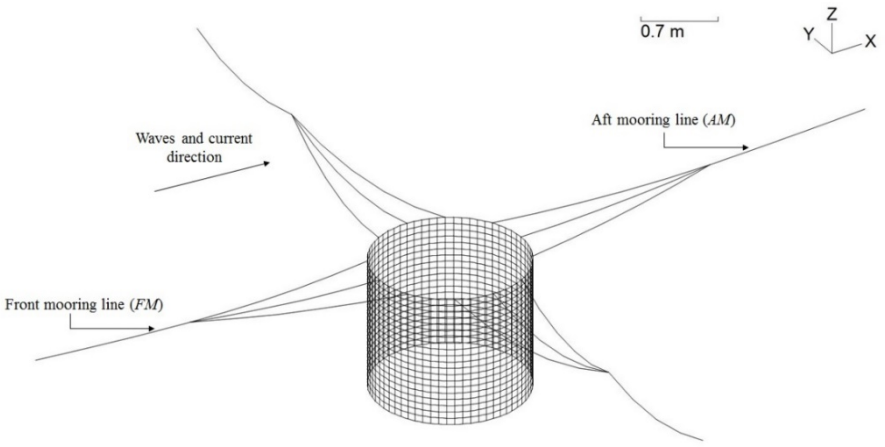

Figure 8.1 Numerical model including cage and mooring lines

From the results presented in Figure 8.2 it can be observed that the present numerical model is able to predict the drag force over the cage with a high level of accuracy.

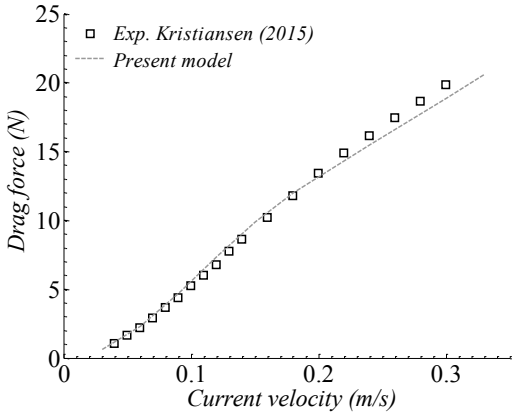

Figure 8.2 Drag force under current

Small differences arise in the region $U_C >$ 0.25 m/s where the model tends to slightly under predict the drag force. Nonetheless; overall the agreement between numerical and experimental data is satisfactory and follows the same trend as the results presented by Kristiansen and Faltinsen (2015) using a screen force model. As shown in Figure 8.3, the deformation of the cage also shows close agreement with experiments. The comparison is presented for the case of 0.1 m/s current. The local deformation on the upstream and bottom sections of the net is well captured in the numerical model. On the downstream section, shielding effect translates into a smooth net profile as shown in experimental and numerical results.

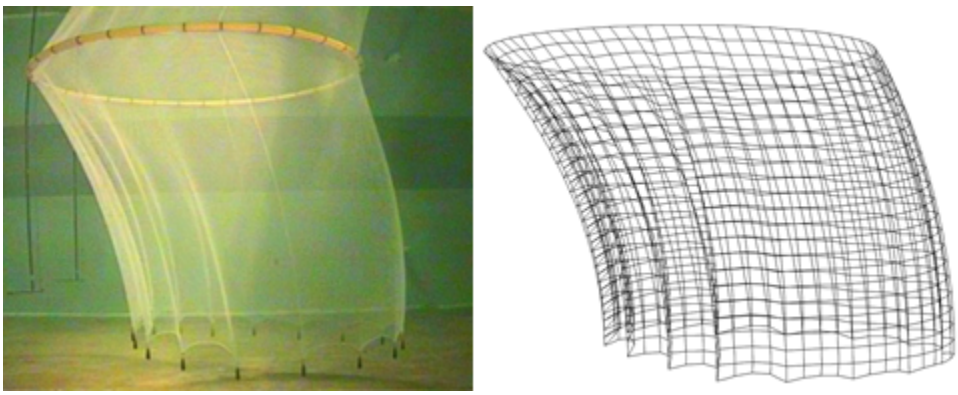

Figure 8.3 Cage deformation comparison for experimental and numerical model

8.3 Mooring line tension over cage under regular wave loading

The second set of results consider regular wave loading over the system presented in Figure 8.1. The cage mooring system was subjected to a series of regular waves moving along the *x* axis. Wave characteristics are presented in Table 8.2. These conditions correspond to the same ones applied to the experimental data used as a

reference in this work. This allows us to directly compare numerical and experimental results. In order to avoid a slack condition on the mooring lines, pretension at the front and aft mooring lines was applied in the numerical model following the experimental case. The actual value of the pretension load is 14 N.

Table 8.2 Regular wave load conditions

Current, U_C (m/s)	**Wave steepness, H/λ**		
	1/60	**1/30**	**1/15**
0.0	0.5 – 1.6 s	0.5 – 1.6 s	0.5 – 1.6 s

Considering the small diameter of net twines and the high *KC* numbers of the netting in the simulation, the flow can be treated as quasi steady and the model used for steady current can be applied to the present case. Thus, the same procedure described previously is applied to create the equivalent net model using the same inertia coefficient.

As for the surface collar, this can be represented exactly as in the physical model using the same geometry and mechanical properties. As for the hydrodynamic load, the same Morison force model applied to the netting is used. However, drag and inertia coefficients need to be defined according to each wave condition.

The inertia component on Morison equation is particularly important for the floating collar. In this case, C_M depends on *Re* and *KC* numbers. For a floating cylinder in oscillatory flow, inertia coefficient follows the same trend as for a fully immersed

cylinder, while C_d is about half of the value for a fully submerged cylinder (Fu et al., 2013a). Based on these findings, a conservative approach is applied in this study. For the floater, C_d is selected as 0.6 for all conditions considering that *Re* ranges between 10^4 to 10^5. In this region C_d is equal to 1.2 for a fully immersed cylinder. C_M is obtained for each wave condition based on *KC* and *Re* numbers considering maximum wave orbital velocity. Actual inertia coefficient values were obtained based on the work by Sarpkaya (1976). For the case of pure waves over the system, the definition of *Re* and *KC* numbers for the floating collar used in this analysis is given by Equation (8.1) and (8.2) where U_M is the maximum orbital wave velocity, d represents floater diameter, ν is kinematic viscosity and T is wave period.

$$Re_{Collar} = \frac{U_M d}{\nu} \tag{8.1}$$

$$KC_{Collar} = \frac{U_M T}{d} \tag{8.2}$$

Figure 8.4 shows the variation of C_M with *Re* and *KC* for a fully immersed cylinder in oscillatory flow. β is defined as the ratio between *Re* and *KC* numbers. In the actual cases, values were obtained interpolating the data on Figure 8.3.

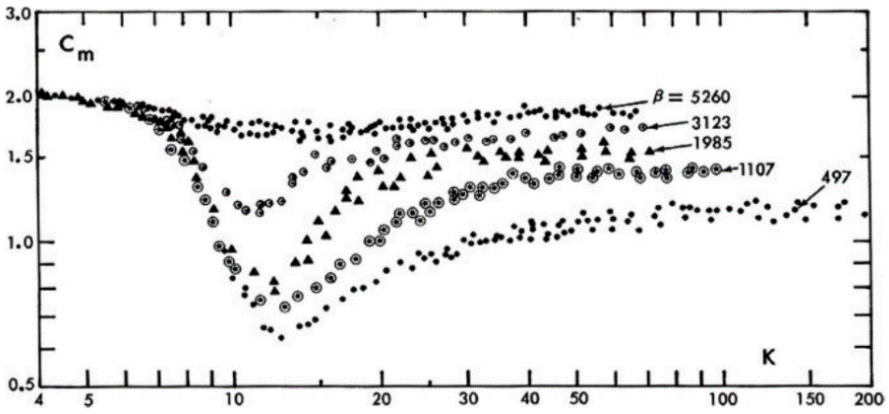

Figure 8.4 C_M values as function of Re and KC numbers from (Sarpkaya, 1976)

8.3.1 Influence of wave kinematics extrapolation models on mooring forces

Considering that when using linear wave theory, wave kinematics are defined up to the mean water level, adjustments need to be made to account for water particle velocity and acceleration at the instantaneous free surface. When diffraction effect is not significant a hyperbolic stretching can be applied to extend linear wave theory up to the free surface (Chakrabarti, 1987).

The effect of wave kinematic approximation above mean water level is analyzed using three different approaches, vertical and linear stretching in addition to Wheeler approximation. In the vertical stretching method, wave velocity above mean water level is considered constant and equal to the velocity at $z = 0$. Linear stretching takes the tangent to the wave velocity profile at $z = 0$, and linearly extrapolates this profile up to the free surface. Wheeler method takes the wave kinematics at $z = 0$ and applied them at the free surface, modifying the velocity profile over water depth accordingly.

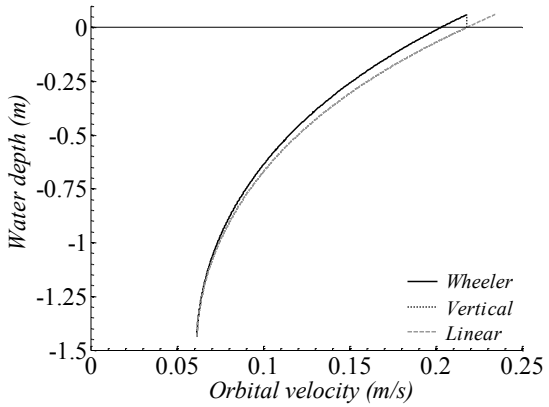

Figure 8.5 Wave kinematics extrapolation methods.

The previous figure illustrates the effect of these kinematic stretching methods over the wave velocity profile along water depth.

Wave kinematics is particularly important since forces over the floater depend on fluid velocity and acceleration, thus an adequate modelling of these properties needs to be considered.

The first set of results to be presented includes the maximum tension on the front mooring line using the three wave kinematics approximation methods described. In this analysis experimental conditions for wave only case are studied. The maximum load is obtained after the transient period. This information shows the largest tension on the upstream mooring line providing vital information for the design of the mooring system. Since no information is provided in the reference paper for tension time series from experiments, this portion of the analysis includes only numerical data. Results show the dynamic portion of the load since pretension has been subtracted.

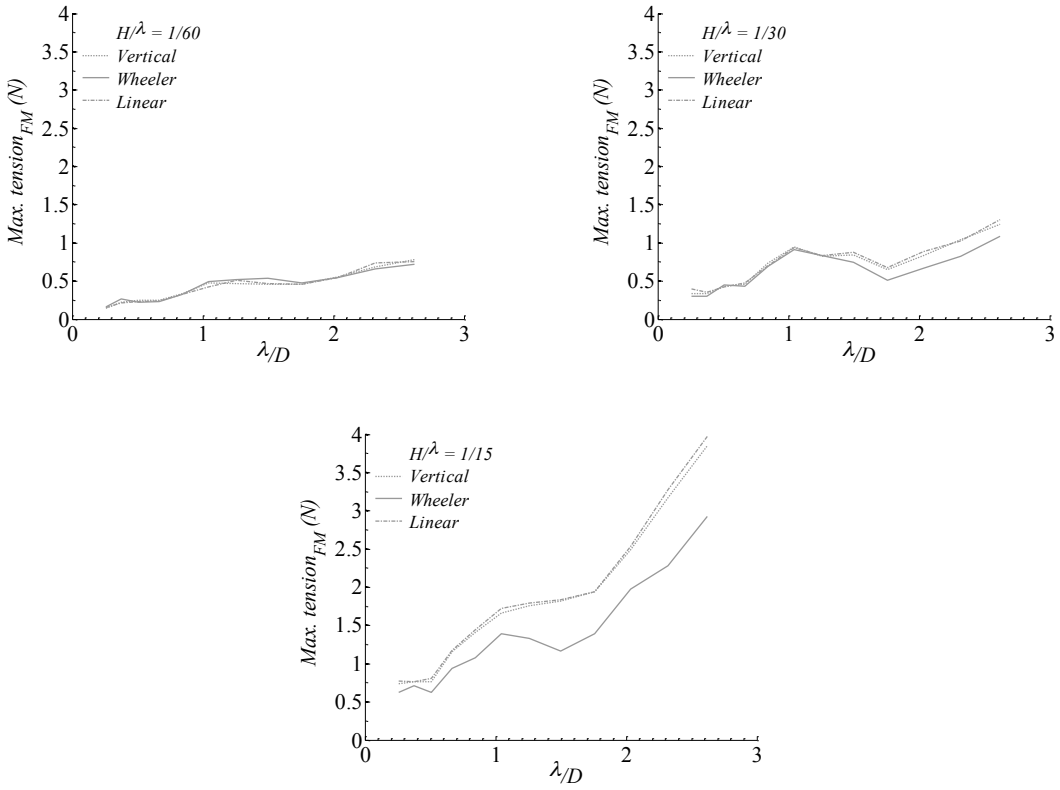

Figure 8.6 Maximum mooring line tension over front mooring line under regular wave loading.

The results show that for small waves, there are not significant differences between wave kinematic extrapolation models; however, as wave steepness increases, the results using Wheeler model deviate from Linear and Vertical methods. This preliminary analysis shows that differences of up to 50% on mooring tension are observed when using different wave kinematics approximation models, particularly for high energy waves. In order to justify the use of a particular model, comparison to experimental data is needed, which is presented in the next set of results.

Results are now presented for the experimental conditions previously described. Plots for mean and total force for the front and aft mooring lines are presented. The total force is defined as the sum of mean and amplitude of the tension on the mooring line. Amplitude is calculated as $F_a = \sqrt{2}\sigma_F$, where σ_F is taken as the standard deviation of the load signal over the same time window as the mean force. Pretension is subtracted from the actual time series obtained in the numerical simulations to isolate the tension coming exclusively from wave loading. Hence, absolute forces are presented. The same procedure was used to analyze the experimental results.

In this analysis, mean force is determined as the mean value of the tension load signal after the transient period. In the next plots, experimental data for the different wave conditions are represented by markers while numerical results from the current numerical method and the numerical results by Kristiansen and Faltinsen (2015) are represented by lines. Plots show the relation between tension forces on front and aft mooring lines on the *y* axis, and the ratio of wave length and cage diameter (λ/D) on the *x* axis.

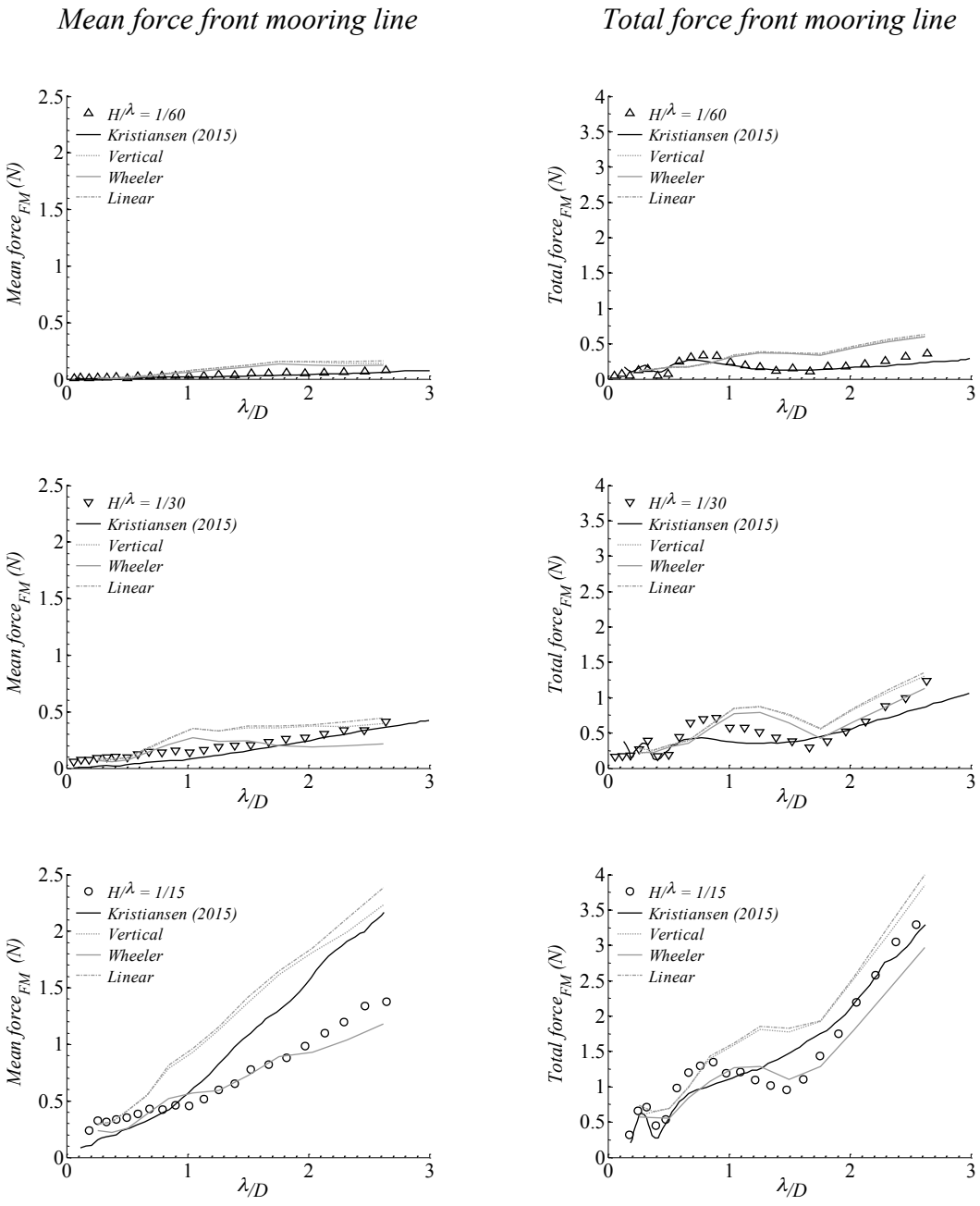

Figure 8.7 Mean and total tension on front mooring line under regular wave loading

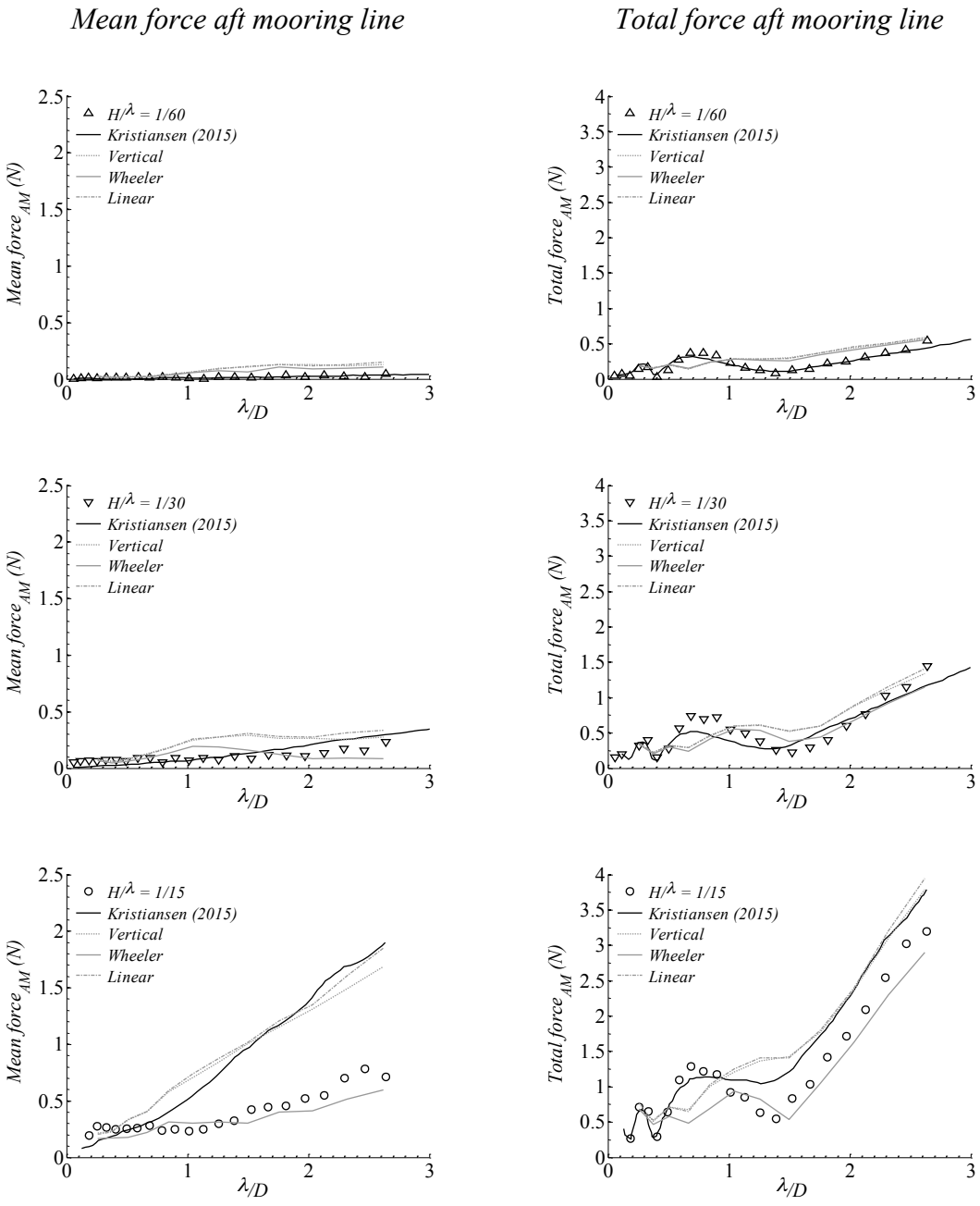

Figure 8.8 Mean and total tension on aft mooring line under regular wave loading

Numerical results from the current Morison force model tend to follow the trend of the experimental results especially for longer waves across all wave steepness

conditions, for front (*FM*) and aft (*AM*) mooring lines. From the plots in Figures 8.7 and 8.8 it can be seen that mooring line tension is small for *s* (wave steepness) 1/60 and 1/30 when compared to the steepest waves (*s* = 1/15). This shows that forces on the mooring lines are strongly influenced by wave height. This must be the main parameter to consider when designing station keeping systems for offshore fish farms. The present model shows close agreement with experimental data for the mean component of the load, for both front and aft mooring lines, for the steepest wave condition over the complete range of wave length. The correlation between experimental and the current numerical model is satisfactory, particularly for s = 1/60 and 1/15 while for s = 1/30 divergence exist over λ/D having an over prediction for $\lambda/D < 1.5$ and an under prediction for $\lambda/D > 1.5$.

As for the total tension for front and aft lines, there is a slight under estimation of the total load for long and steep waves, while for small amplitude waves, numerical results show high accuracy, especially for longer waves ($\lambda/D > 1.5$). For short waves, the divergence between numerical an experimental data comes from the fact that the deformation modes of the surface collar play an important role on the mooring line tension. This deformation is better described by a complete hydroelastic model, which takes into account the modes of vibration of the floater, as the one presented by Kristiansen and Faltinsen (2015). This phenomenon is not well capture by the Morison force model for the case H/λ = 1/15 being the zone of $\lambda/D < 1.0$ the one with the largest under estimation of tension force. This can also be observed on the numerical results by Kristiansen and Faltinsen (2015) showing the complexity of the dynamic response of

highly flexible structure under pure wave action. For $\lambda/D > 1.0$, the surface collar follows the wave and its motion is closer to the dynamic response of a rigid body for which numerical models, such as Morison and hydroelastic, show acceptable performance over the wave conditions analyzed in this study. From a practical perspective, when performing mooring and structural analysis, calculations are done for extreme conditions given by long and high waves. For those cases, the present numerical model is able to predict the loads with high accuracy validating the numerical approach. In addition, the fact that only one type of element is used to model both net and surface collar speeds up the calculations allowing the study of multiple cage configurations and environmental conditions in a short period of time. The rationale behind the selection of drag and inertia coefficients, based on the conclusions by Fu et al. (2013) that for a semi submerged pipe under wave loading, inertia coefficients are similar as for the case of a fully immersed pipe, proves to be accurate.

Based on the results, when using a Morison force model, selection of inertia coefficients must be based on *Re* and *KC* parameters considering the maximum orbital wave velocity and pipe diameters as main inputs.

As for the kinematic stretching model, Wheeler stretching seems to have the largest impact over the accuracy of the results. Even though this model is not physically correct, since this model does not satisfy Laplace's equation, its application generates the closest agreement with experimental data when compared to the performance of vertical and linear stretching techniques. Results show that there are no major differences between the results obtained when using vertical and linear techniques. On

the other hand, using Wheeler stretching significantly improves the accuracy of the numerical calculations when compared to the experimental data. In addition, since the numerical reference work used in this analysis uses Wheeler stretching, a direct comparison using similar assumptions seems appropriate to evaluate the accuracy of the present numerical scheme.

Overall, the results under wave only condition including multiple effects, such as local and global blockage of the flow over net and floater using Morison equation, proves to be a valuable tool for the evaluation of mooring line forces under a wide range of load scenarios.

8.4 Mooring line tension over cage under regular wave current interaction

After the validation of the numerical scheme for regular waves was complete, the next step is to include current on the system and compare present results against published experimental and numerical data. Wave current interaction effects are particularly important when calculating the hydrodynamic response of offshore structures, in which storm and operational scenarios consider a collinear combination of waves and current for design purposes. In addition, several studies have shown the relevance of current loading when calculating forces on cages/nets. Consequently, wave current interaction effects are relevant and it is necessary to further investigate them for future offshore fish farm applications.

The conditions analyzed in this section are described in Table 8.3. In this case, wave conditions for H/λ = 1/30; 1/15 are consider plus current speeds of 0.1 and 0.2

m/s. Given the scale of the reference experiments, these velocities correspond to 0.5 and 1.0 m/s in prototype scale. A 1 m/s current speed is characteristic of an exposed location according to Norway Standard (2009), hence, these conditions are of particular interest for offshore locations.

Table 8.3 Regular wave current interaction conditions

Current, U_C (m/s)	**Wave steepness, H/λ**	
	1/30	**1/15**
0.1	0.5 – 1.6 s	0.5 – 1.6 s
0.2	0.5 – 1.6 s	0.5 – 1.6 s

Mean, amplitude and total force are defined in the same manner as in the case of pure wave loading. The pretension on the front and aft mooring line is 14 N, and this pretension is subtracted from the time series of mooring line tension. In this case, the findings form the wave only conditions are applied and Wheeler stretching is applied to all wave/current conditions. As for the selection of inertia coefficients for the surface collar, the values for a fully immersed cylinder were selected. In the case of wave current interaction, the maximum velocity over the floater will increase. Hence, the definition of *Re* and *KC* numbers must account for this effect as described in Equations (8.3) and (8.4) where U_C represents current velocity.

$$Re_{Collar} = \frac{(U_M + U_C)d}{\nu} \tag{8.3}$$

$$KC_{Collar} = \frac{(U_M + U_C)T}{d} \tag{8.4}$$

Results are presented for front and aft mooring lines considering its mean and total force components. In the next plots, dots represent experimental data while solid lines represent numerical calculations by Kristiansen and Faltinsen (2015) using a screen force model. Gray lines account for the results using the present model. The first set of results consider U_C = 0.1 m/s.

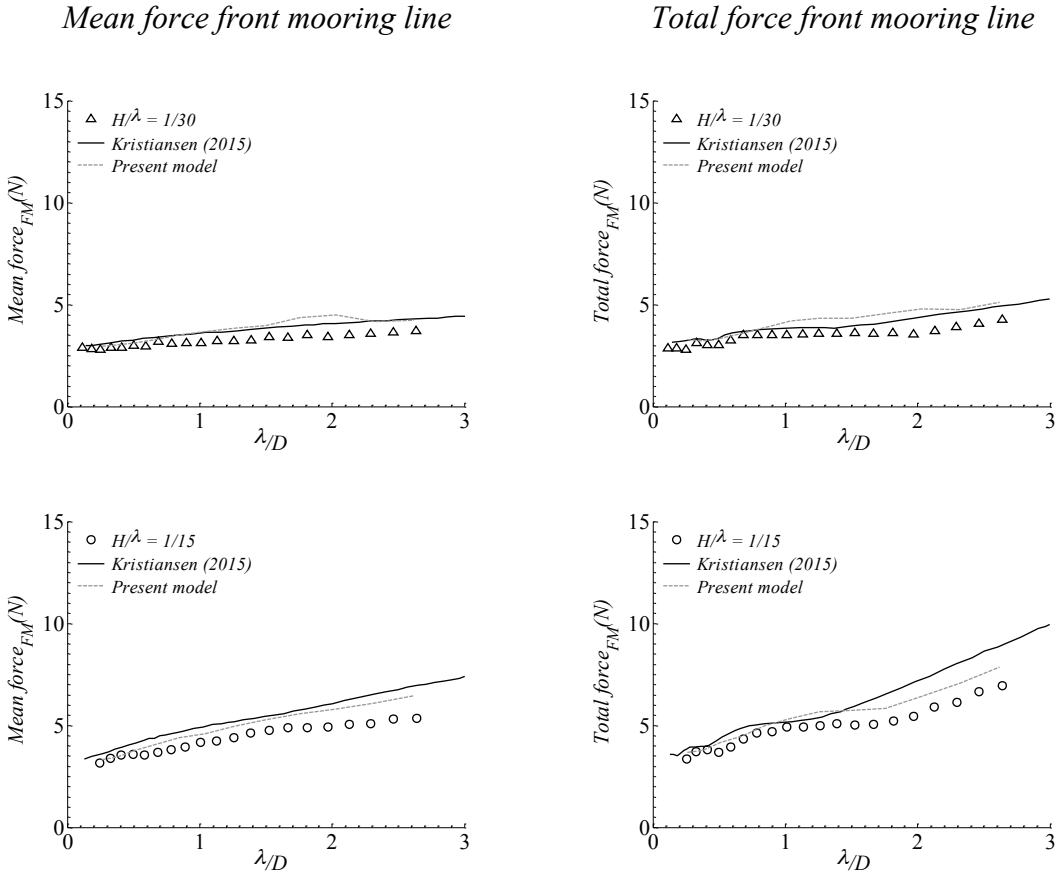

Figure 8.9 Comparison wave current interaction for U_C = *0.1* m/s, front mooring line

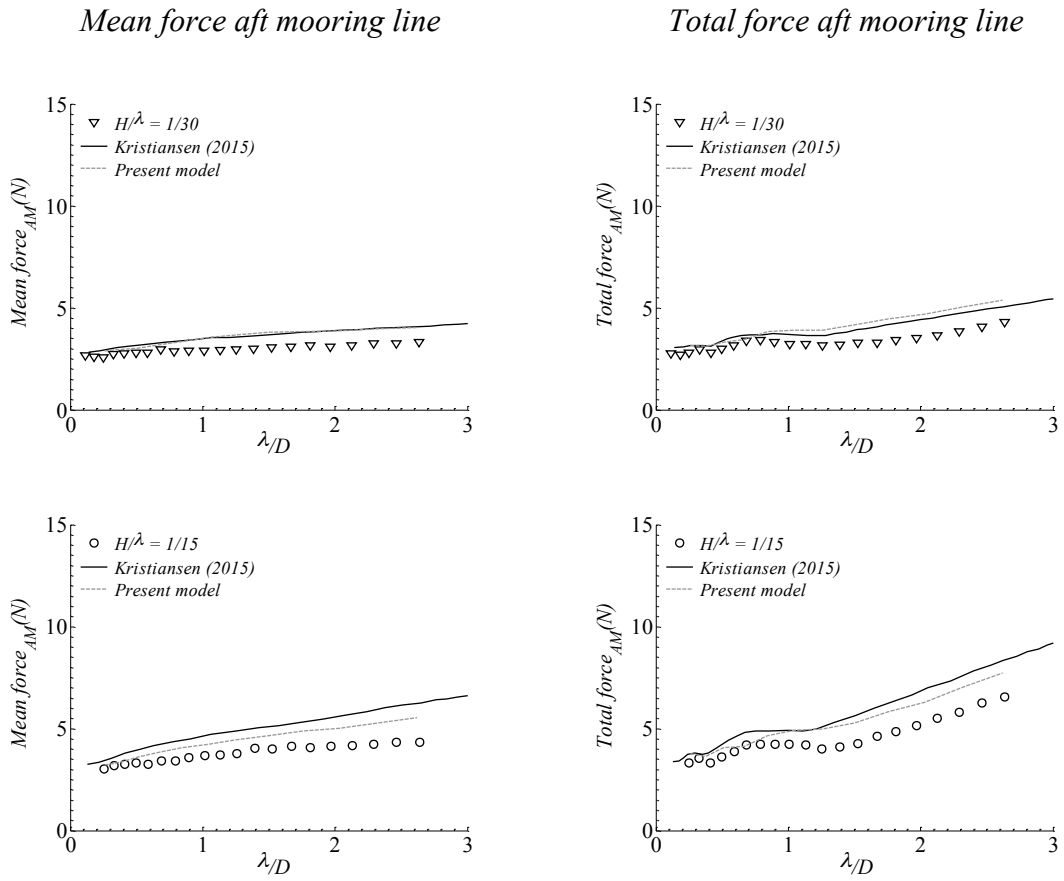

Figure 8.10 Comparison wave current interaction for $U_C = 0.1$ m/s, aft mooring line

The following set of results consider the case for U_C = 0.2 m/s for front and aft mooring line tension.

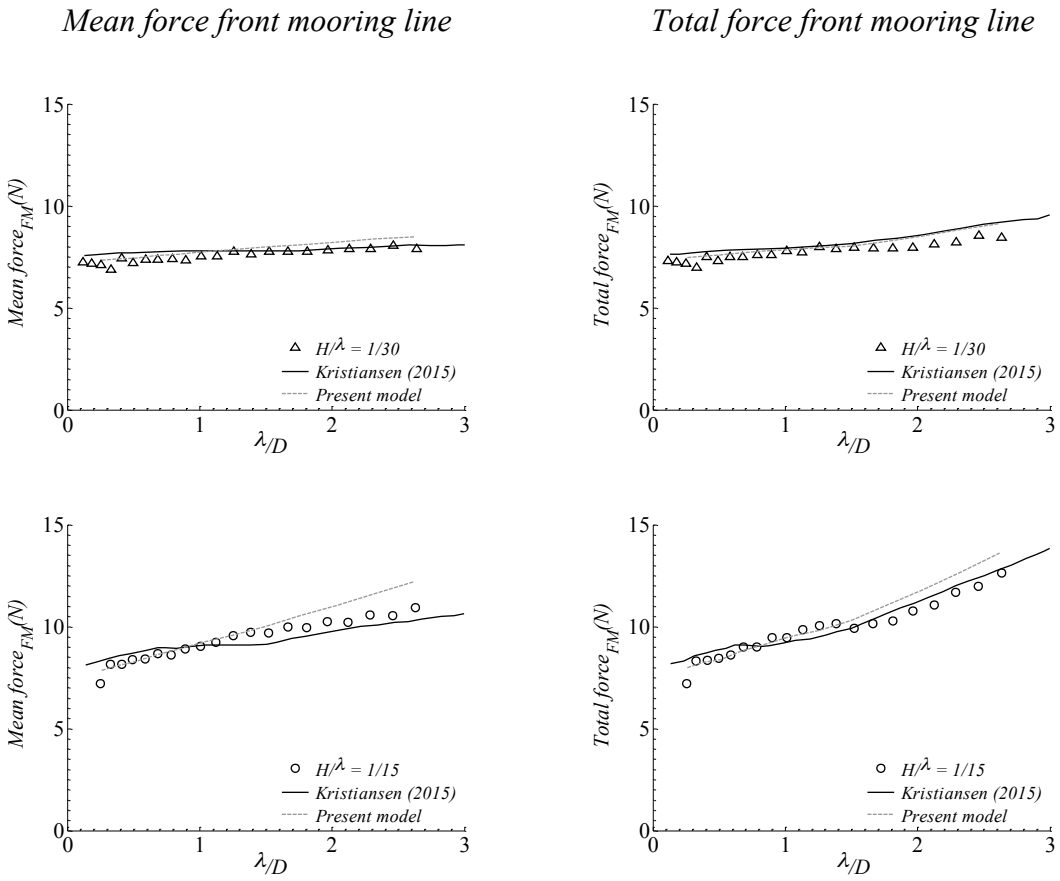

Figure 8.11 Comparison wave current interaction for $U_C = 0.2$ m/s front mooring line

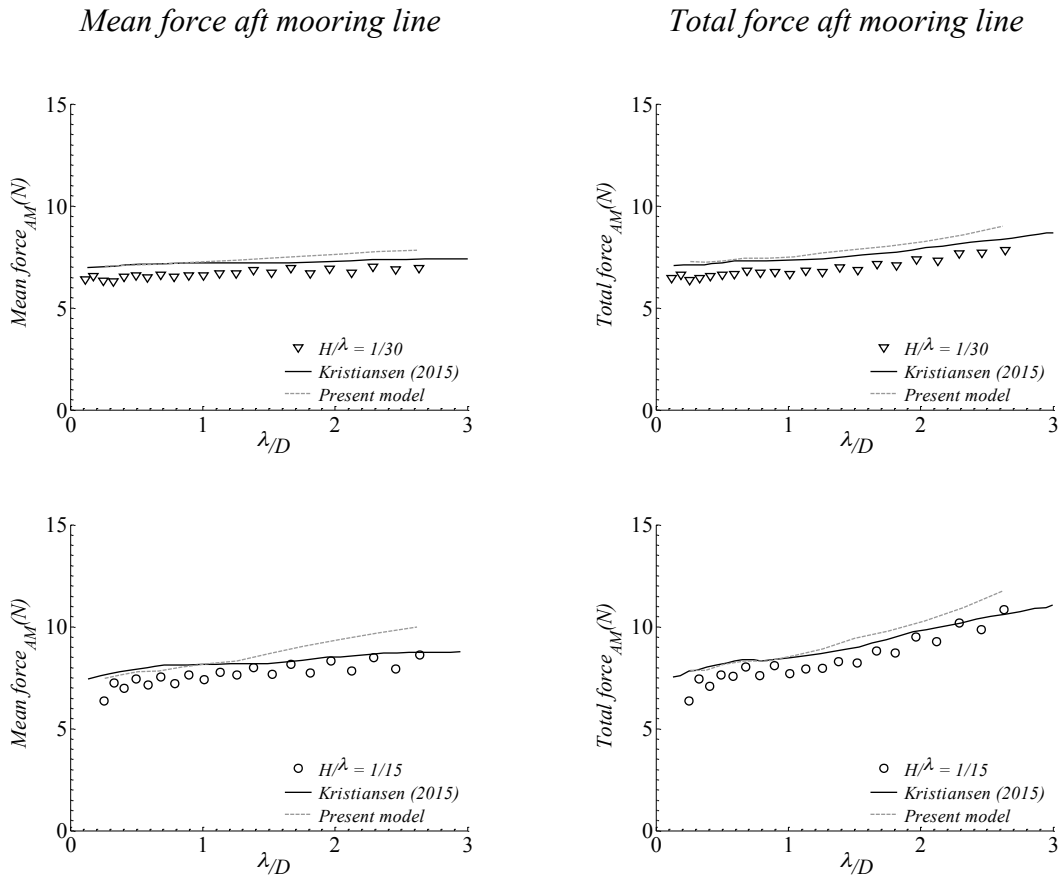

Figure 8.12 Comparison wave current interaction for $U_C = 0.2$ m/s, aft mooring line

From a fist look at the results, it can be seen the significant effect of current loading over the system. At the same time, the plots describe how both numerical models follow the trend of the experimental data. This is expected since both models were originally developed and validated for current loading, particularly for the netting portion of the cage.

In this case, the tendency of mooring line tension varies almost linearly with wave length with a small variability for the region of the shortest waves. The difference

between wave conditions $H/\lambda = 1/30$ and $H/\lambda = 1/15$ is a slight change on the slope of the curves for tension. The same observation is valid for front and aft mooring lines.

Numerical results consistently over predict tension loads on front *(FM)* and aft *(AM)* mooring lines; however, the differences are rather small. The divergence between numerical and experimental data grows as wave length increases; yet, screen and Morison force model show enough margin of confidence for the determination of mooring line tension under wave current loading. For short length waves ($\lambda/D < 1.0$), Morison model shows close agreement with experimental results across all conditions analyzed. In this area, the dominant load factor is the viscous drag load on the netting due to current loading. As for larger waves, the current model is still able to predict with high accuracy the loading over the mooring lines, especially for the case of weak current speeds. For high current velocity, screen model shows a higher accuracy when compared to Morison model, still, this is expected since at high current speeds, it has been shown that Morison model tends to over predicts drag forces (Moe-Føre et al., 2014). Nonetheless, the inclusion on the model of the semi empirical formulation for the net's drag coefficient, in addition to the modeling of shielding effect, proves to significantly impact the results making numerical results presented in this analysis equivalent to the ones from the screen plus hydroelastic model.

The largest tension is obtained for the longest and steepest waves under maximum current speed as expected. The increase in current speed is not directly correlated with the increase in mooring tension. This is predictable at high current speed where the stream does not flow across the net, but around and below the cage changing

the slope of the current speed/drag force curve which tends to plateau for current velocities over 0.5 m/s.

8.5 Discussion

A complete analysis of the hydrodynamic response of a single cage under current, regular waves and regular waves/current loading condition is presented. The main focus of the analysis was the mooring line tension response and the effect of the superposition of waves and current over the overall dynamic response of the cage. The analysis is based on previously published experiments in order to validate the current approach and evaluate its accuracy when compared to a screen netting model coupled with a hydroelastic collar description.

The present numerical model shows high accuracy across all conditions analyzed, when compared to the available experimental data. The model has been previously validated against current only condition; still, under wave current interaction, the numerical results are able to follow the trend of experimental data. For current only, there is excellent agreement between numerical and experimental data. When only regular waves are considered, good agreement is achieved for long waves. For short waves, the present model tends to under predict the tension. This is mainly due to the local deformation of the surface collar which cannot be completely described by using a Morison force model. For steep and long waves, which represent strong sea conditions used in design stages, the model proves to be reliable. In addition, the computation time is of the order of minutes for a time series of 50 seconds, therefore it is useful when

optimization of the mooring system is required. C_M values were selected based on experimental evidence and Wheeler stretching is applied after comparing against the results using vertical and linear extrapolation stretching methods.

When regular wave/current interaction is considered, the numerical results follow the experimental data and shows high precision for short waves for both wave steepness cases analyzed. The model tends to slightly over predict the tension load for long waves; yet, this error is on the same order of magnitude obtained by other numerical models. Overall, the results are satisfactory and show the relevance of both, waves and current effects, over the mooring line tension, particularly for long and steep waves.

When comparing the results of waves only and the collinear combination of regular waves and current loading, it is perceived that viscous drag force over the net is a relevant component of the total load on the system. Nonetheless, when considering current speed of 0.1 m/s and long waves, the significance of wave and current load is similar, highlighting the importance of the accurate prediction of both, wave and current effects, especially for long and steep waves.

The load significantly increases when current is present being the maximum load in the wave/current case almost 4 times the maximum value obtained for waves only. For short waves results do not have a clear trend when only waves are considered; on the other hand, this variability is missed in the combination of waves and currents due to the strong effect of the viscous drag on the net, even at steep and short waves. In waves only, the tension on the mooring lines is greatly influence by wave height. A significant increase in load in observed for the experimental measurements and numerical

calculations between $H/\lambda = 1/30$ and $H/\lambda = 1/15$ conditions. As for the combined wave/current case, the influence of wave height is not as pronounced and the slope of the tension curves does not have a steep increase as for the case of waves only.

Based on the results from both conditions, waves and wave/current, when designing mooring systems for fish farms, the effect from strong currents and large amplitude/long period waves must be taken into account since its influence can be equal over the global force on the cage. In addition, when using a Morison force model, the selection of inertia coefficients for surface collar is critical to achieve reliable results. The same holds true for the drag coefficient for the netting which needs to account for the blockage of the flow at high deformations on a flexible cage, in addition to including the local shielding effect due to the loss of momentum of the flow when crossing the upstream panel of the cage. The effective combination of numerical tools to describe the different effects in the present calculations shows high accuracy, even for combinations of wave amplitude and periods that generate nonlinear events such as breaking waves and overtopping at the surface collar.

9. FORCES AND MOTION ANALYSIS OF CAGE UNDER IRREGULAR WAVES/CURRENT INTERACTION

9.1 Introduction

In real sea conditions, a single cage or fish farm will be exposed to a combination of waves and current. As for waves, a classical representation of a sea state consists of a superposition of multiple regular waves with different frequencies. After the validation of the numerical technique is complete for regular waves, the next natural step is to analyze a system under irregular wave loading and collinear current.

In this case, the numerical model used in the previous section is used and exposed to irregular waves represented by a Jonswap spectrum and collinear current loading. Conditions are modeled for an exposed offshore site under a storm event. The novelty of this analysis relies on the fact that a flexible surface collar is used instead of considering this component as a rigid body. Up to this point most numerical, experimental and in situ studies have considered rigid cages exposed to irregular waves. In addition, shielding effect is included in the present calculation; this effect has not been applied in previous analysis by other authors when irregular wave loading is considered. Also, a rational selection of coefficients to be used in Morison equation is proposed based on wave and current conditions.

Based on published experiments and site measurements, heave RAO results reveal that a cage behaves as a highly damped system where minimum response at high frequency excitations is observed (DeCew et al., 2005). At the same time, resonance

responses are estimated to be at quite low frequencies, below 0.05 Hz. This feature has also been observed in the mooring line tension response for a SPM cage under irregular waves and current loading (Huang et al., 2010).

As for surge motion, the system is highly influence by the mooring line design which can completely restrict the horizontal motion of the cage overcoming the Stokes drift effect over the surface collar (Fredriksson et al., 2003b). Further analysis have shown that a linear relation exist between wave elevation, surge, heave and mooring line tension when a rigid surface collar is utilized in numerical simulations (Dong et al., 2010; Xu et al., 2011).When the bending stiffness of the surface collar is taken into account in numerical calculations, rigid body modes are more relevant in horizontal motions when exposed to waves, flexural modes occur at higher than wave frequency, thus its influence is not relevant on the analysis (Li et al., 2013a).

The accurate computation of loads and deformation of the net under wave current interaction is critical in the determination of the cage response under irregular waves. The interaction between netting and surface collar largely influence the horizontal motions of the cage (Li et al., 2013b). Snap loads can also occur between netting and surface collar inducing higher tension on the threads and connectors on the surface collar leading to potential failures and escapes (Bardestani and Faltinsen, 2013).

An important reason to analyze the response of cages under irregular waves is to further study the response of components such as surface collar and mooring line to fatigue over time. Low and wave excitation frequencies influence the fatigue life of

mooring components in a cage under wave loading. Low frequency can play a role when an increase on wave height is considered (Xu et al., 2014).

In the next sections, results for tension on mooring lines and motion of the cage will be presented and analyzed in time and frequency domain to correlate the response of the cage and mooring lines with the environmental conditions applied in each calculation case.

9.2 Description of numerical model and environmental conditions

The next set of results to be presented considers the cage subjected to a combination of irregular waves and collinear current. Conditions for an exposed location according to Norway Standard (2009) were selected and downscaled according to the geometric scale of the experimental model. The same model as analyzed in section 8 is used. For the prototype site, significant wave height and peak period are 3 m. and 9 s., while for the model, H_s is equal to 0.12 m. and T_p is 1.8 s. To represent this sea condition, a Jonswap spectrum is applied (Goda, 2010). The actual formulation is presented in Equations (9.1), (9.2), (9.3) and (9.4).

$$S(f) = \beta_J H_{1/3}^2 T_p^{-4} f^{-5} \exp[-1.25(T_p f)^{-4}] \gamma^{\exp\left[\frac{(T_p f - 1)^2}{2a^2}\right]} \tag{9.1}$$

$$\beta_J = \frac{0.0624}{0.230 + 0.0336\gamma - 0.185(1.9 + \gamma)^{-1}} [1.094 - 0.01915 \ln \gamma] \tag{9.2}$$

$$T_p \cong T_{1/3} / [1 - 0.132(\gamma + 0.2)^{-0.559}] \tag{9.3}$$

$$\sigma = \begin{cases} \sigma_a : f \le f_p \\ \sigma_b : f \ge f_p \end{cases}, \quad \sigma_a \cong 0.07,\ \sigma_b \cong 0.09 \tag{9.4}$$

Peak enhancement factor γ defines the peakedness of the spectrum, while σ describes the energy spreading over the frequency range selected. In Equations (9.1) and (9.3) $T_{1/3}$ and $H_{1/3}$ are significant wave period and height respectively. The sea states parameters, at model scale, used in Jonswap spectrum are presented in Table 9.1. The input spectrum and wave elevation time series is shown in Figure 9.1.

Table 9.1 Irregular wave load conditions

Current, U_C (m/s)	**Jonswap spectra parameters**		
	H_s (m)	**T_p (s)**	**γ**
0.0	0.12	1.8	3.3
0.1			
0.2			

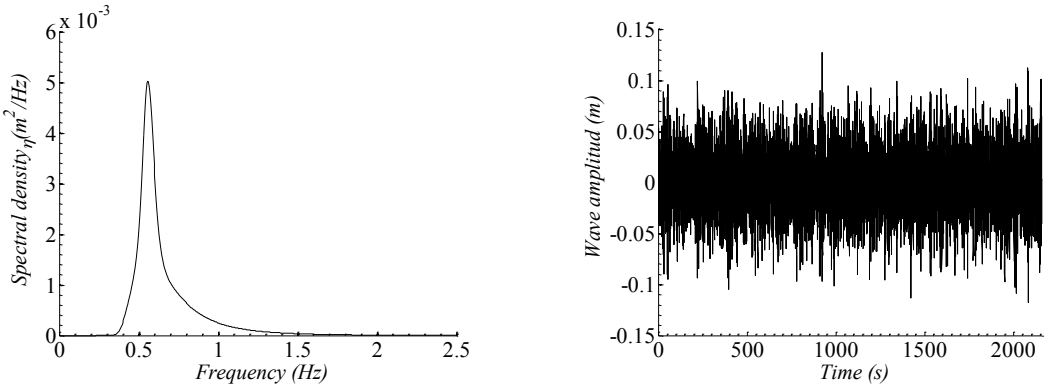

Figure 9.1 Input spectrum and wave time series

Same conditions for cage setup as in section 8 are used this time pretension is included in the tension results. As it was previously described, inertia coefficient values for surface collar must be defined in terms of wave conditions characterized by *Re* and *KC* numbers. In the case of a sea state composed of multiple wave components, a rational selection of C_M values must be done, since our current model does not include a time dependent C_M formulation. Considering that the given sea state is represented by the combination of a significant wave height and period, C_M values for the surface collar are selected based upon those parameters, in addition to the corresponding current speed. Therefore, *Re* and *KC* numbers are calculated using Equations (8.3) and (8.4) to obtain C_M based on the plots by Sarpkaya (1976). Wheeler stretching is used in these calculations based on the conclusions from the regular wave cases plus the drag coefficient formulation derived in section 7.

Considering the scale of the model, a fully developed sea state is reached after 2160 s., thus the set of simulations presented in this section considered this time scale.

9.3 Mooring line tension analysis

In this section, the tension over the front and aft mooring lines of the arrangement presented in Figure 8.1 is calculated and analyzed under regular/irregular wave loading and collinear current. For completeness of the study, a set of calculations using regular waves considering the same period and wave height as the significant wave height and peak periods for irregular waves are presented. In addition, cases considering current speed 0.1 and 0.2 m/s are superimposed to the waves to evaluate its effect.

Results will be correlated with wave height for all cases to understand the influence of waves and current speed over the tension loads. Statistics of tension are presented for each condition as well.

9.3.1 Regular wave cases

The first set of results considered regular waves and current. The steady portion of the calculations is presented. At the beginning of the simulation period a ramping function is used to steadily apply waves and current to the models and avoid transient effects reducing possibilities of numerical instability due to sudden peaks in tension or cage motion.

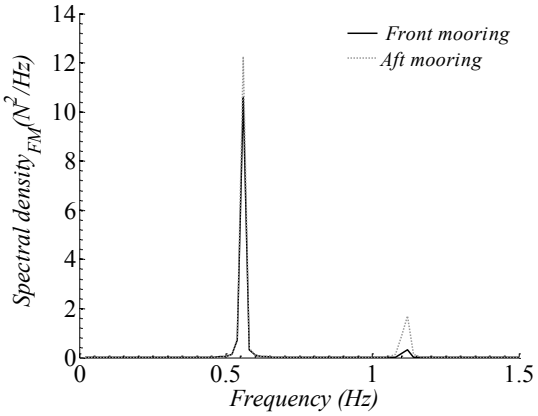

Figure 9.2 Mooring line tension response under waves only condition

Form the results in Figure 9.3, the effect of steady current can be observed. When only waves are included in the analysis, the tension response on the front mooring line is synchronized with the wave signal. Under this condition, the tension response shows

peaks at wave frequency as well as twice the wave frequency showing wave-wave interaction effects over the tension load, as presented in Figure 9.2.

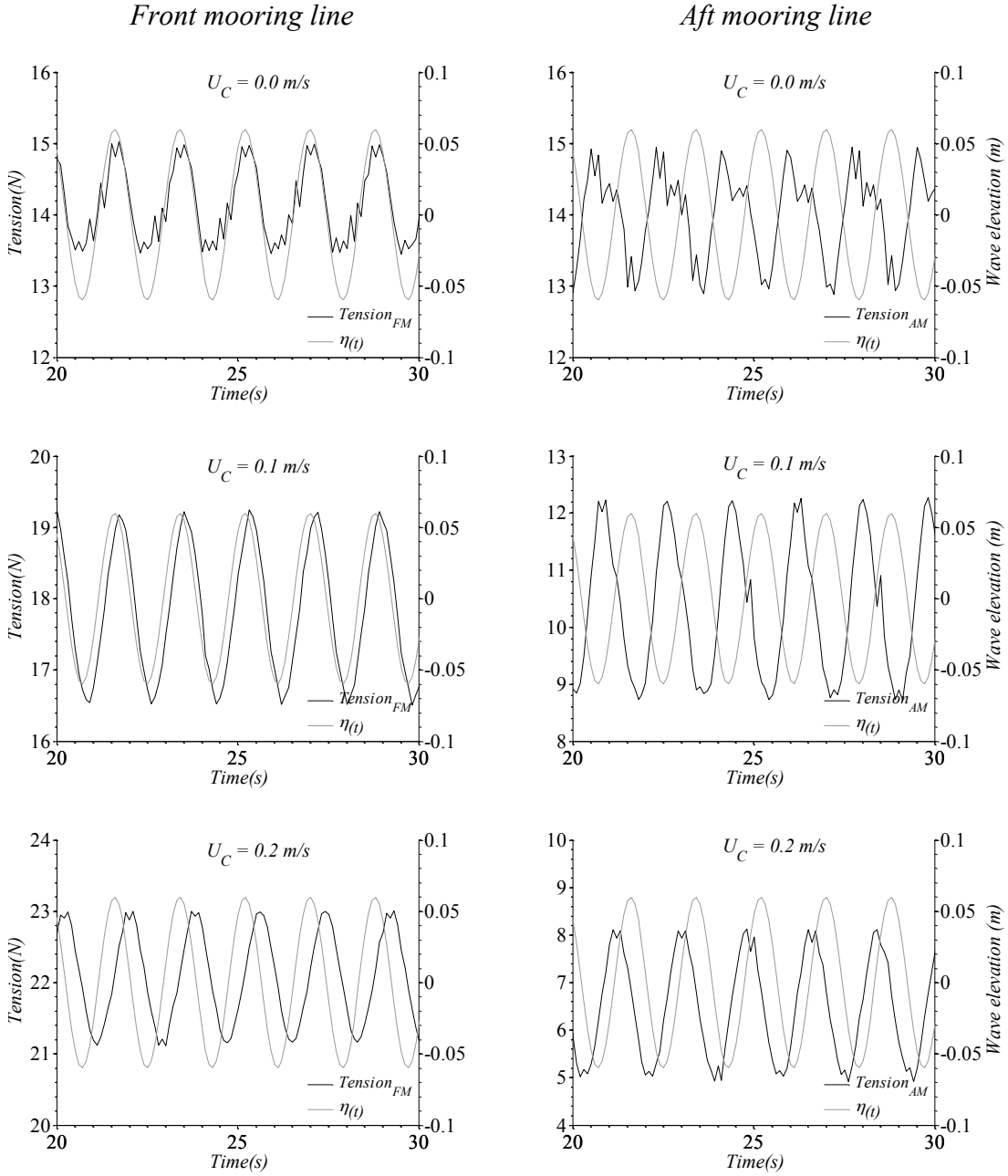

Figure 9.3 Mooring line tension under regular wave loading

For the cases considering regular waves and current, mooring line tension shows a shift on the response when compared to wave elevation. This shift is due to the presence of a collinear current. Differences between phases among front and aft mooring tension signals reveal the effect of the deformation of the surface collar when waves move from left to right. Another interesting feature of the system is the fact that wave current interaction does not represent a simple superposition of effects as could be expected. This is clearly seen by analyzing the statistics of each case.

Table 9.2 Statistics for front mooring line under regular waves

Current, U_C	**Wave parameters**		**Tension results front mooring line (N)**			
(m/s)	***$H_{1/3}$ (m)***	***T_p (s)***	**Mean**	**SD**	**Max**	**Min**
0.0	0.12	1.8	14.15	0.51	14.99	13.44
0.1			17.84	0.91	19.27	16.51
0.2			22.05	0.64	23.01	21.14

Table 9.3 Statistics for aft mooring line under regular waves

Current, U_C	**Wave parameters**		**Tension results aft mooring line (N)**			
(m/s)	***$H_{1/3}$ (m)***	***T_p (s)***	**Mean**	**SD**	**Max**	**Min**
0.0	0.12	1.8	13.98	0.59	14.98	12.88
0.1			10.34	1.20	12.28	8.67
0.2			6.51	1.10	8.19	4.83

Based on the steady current analysis previously performed, the drag load over the cage for current speeds of 0.1 and 0.2 m/s is 5.58 and 13.18 N respectively. Wave current interaction translates in a mean value smaller than the simple combination of current and wave effect. This leads to the conclusion that interaction must be taken into account when designing mooring lines for fish farms. Based on the results, the conclusion that current loading has a large impact on the mooring line tension is further confirmed.

9.3.2 Irregular wave cases

The next set of calculations considers the combined action of steady current and irregular waves as described in Table 9.1. As mentioned before, the wave parameters included in this analysis resemble the conditions for an exposed location according to Norwegian standards. This code is the only available for the design of fish farms and therefore, its guidance is considered in this analysis.

The next set of results shows the front and mooring line tension considering a variation of current speed. As before, C_M values for the surface collar are selected based on wave and current parameters.

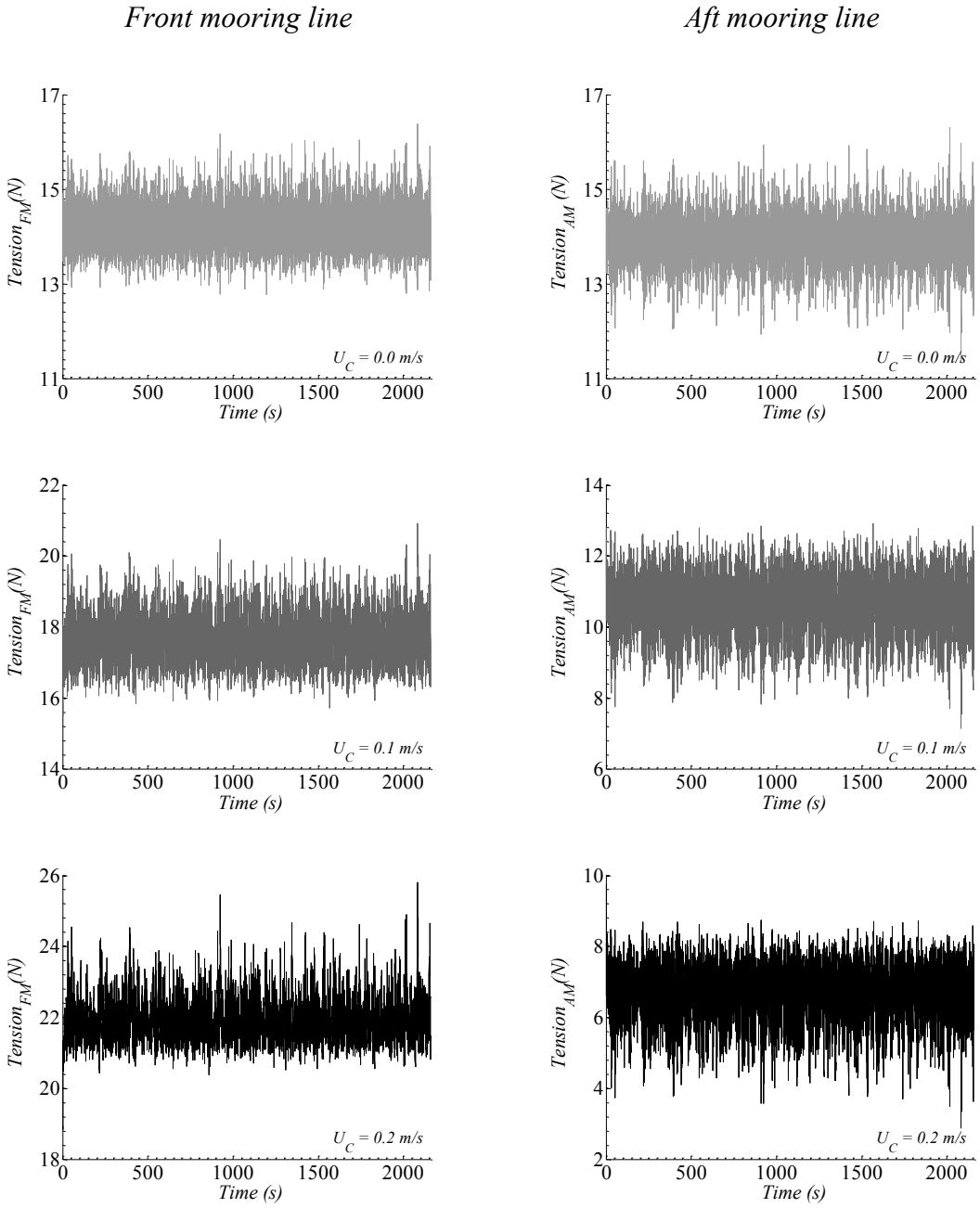

Figure 9.4 Mooring line tension under irregular wave loading

Tables 9.4 and 9.5 show the statistics of time series presenting the variation of mooring line tension when current load is included. From the results it can be seen that

the addition of a steady current shifts the mean value of the load and increases the amplitude of the tension load. An increase on current speed neither translate into a linear nor a quadratic increase in the mean values for mooring line tension, while standard deviation results are similar and unaffected by viscous drag forces.

Table 9.4 Statistics for front mooring line under irregular waves

Current, U_C	**Wave parameters**		**Tension results front mooring line (N)**			
(m/s)	***$H_{1/3}$ (m)***	***T_p (s)***	**Mean**	**SD**	**Max**	**Min**
0.0	0.12	1.8	14.21	0.44	16.37	12.77
0.1			17.72	0.66	20.90	15.71
0.2			21.96	0.59	25.79	20.38

Table 9.5 Statistics for aft mooring line under irregular waves

Current, U_C	**Wave parameters**		**Tension results aft mooring line (N)**			
(m/s)	***$H_{1/3}$ (m)***	***T_p (s)***	**Mean**	**SD**	**Max**	**Min**
0.0	0.12	1.8	13.94	0.47	16.29	11.32
0.1			10.50	0.79	12.90	7.13
0.2			6.60	0.77	8.72	2.88

Under irregular load, statistics are similar to the ones for regular waves. An increase on the maximum tension is observed, though no larger than a 10% compared to the regular wave current cases. This again shows the relevance of current wave loading

over the netting which drives the tension over the mooring system components for mild wave and current conditions.

As with the case of regular wave loading, the plots showing the phase correlation between wave elevation and mooring line tension are presented.

From the next figure, under irregular wave loafing there is a strong correlation between wave elevation and mooring line tension. Peaks occur at almost the same instant on time during the short realization presented, even when current is included. The mooring line tension signal shows high frequency response superimposed to the wave frequency component. This could be explained by the deformation of the surface collar which is highly flexible and able to deform as waves propagate along its diameter. This high frequency response can also be due to the interaction between the net and the surface collar. As mentioned earlier, this interaction could lead to snap impulse loads at certain frequencies. In addition, the axial deformation of the mooring lines could also contribute to the high frequency phenomenon. These ideas need further investigation; however, the hydroelastic response of the floater seems like a reasonable option considering the low bending stiffness of the material.

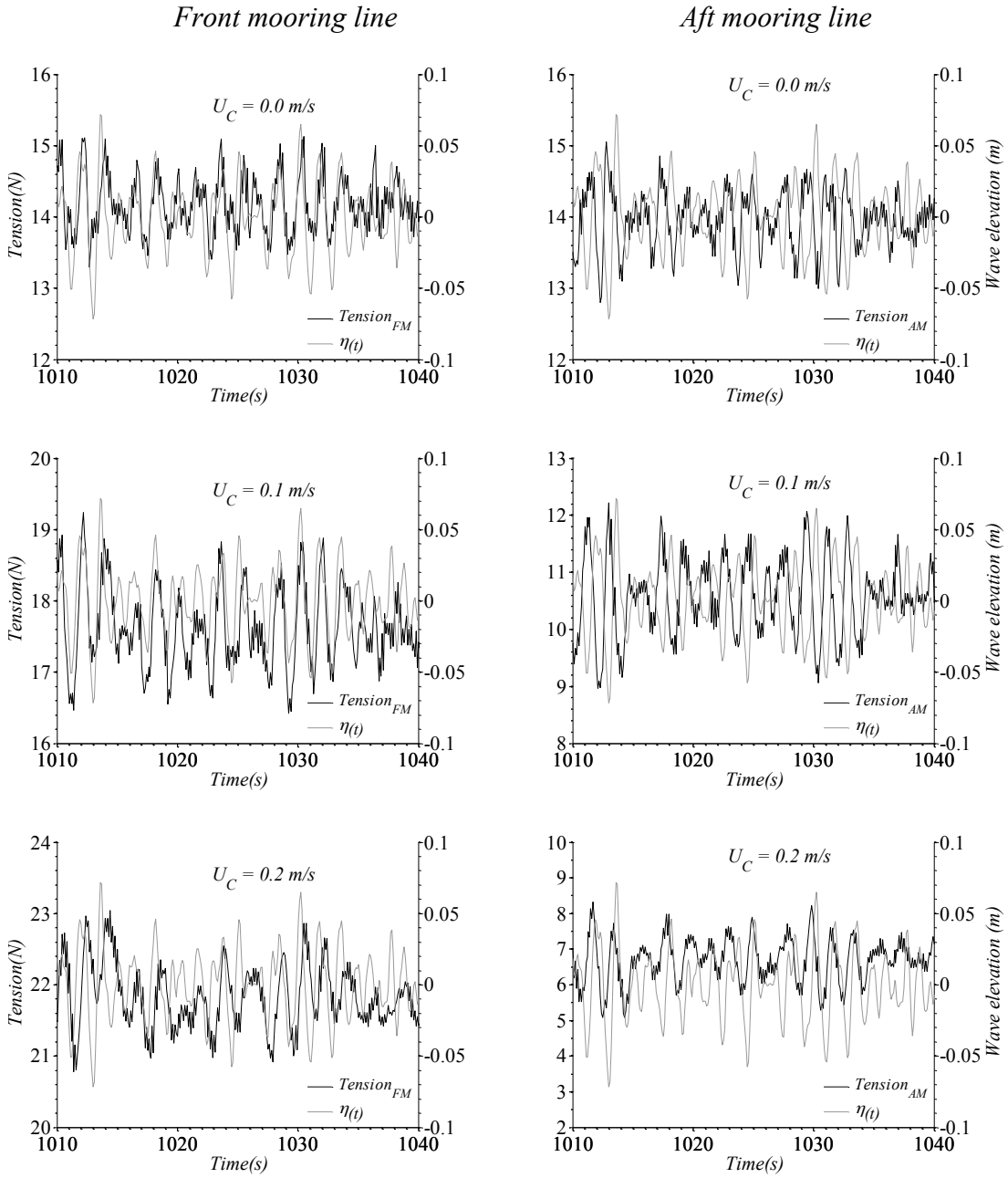

Figure 9.5 Wave elevation and mooring line tension under irregular wave loading

Another interesting manner to look at the mooring line response is to check the spectral density plots for each plot in Figure 9.4 in order to observe the wave current interaction effects over the overall response.

After analyzing the results, several aspects of the irregular wave/current interaction can be described. The fact that under zero current speed there exist a non-zero mean tension, shows the effect of the mean wave drift force over the cage. Forces on the mooring lines are dominated by wave frequency as can be observed in Figure 9.6. This means that the cage is primarily following the waves. The surface collar mainly reacts as a rigid body to the environmental loads. As the current speed increases, the spectral density plots reveal how current load becomes relevant on the mooring line tension. Current increases the peak of the spectral response for tension and induces a second peak on the low frequency region due to the viscous drag force over the netting. This effect can clearly be seen for the front mooring line, which bears most of the load given the direction of the wave/current loads. For a mild current, U_C = 0.1 m/s, wave effect over mooring line tension is still the dominant effect; nonetheless, the low frequency component is significant for front and aft mooring lines. For a strong current, U_C = 0.2 m/s, the influence of current and wave load is similar for the tension on the front mooring line. Differences between front and aft mooring line responses can be explained by the deformation of the surface collar as waves propagate.

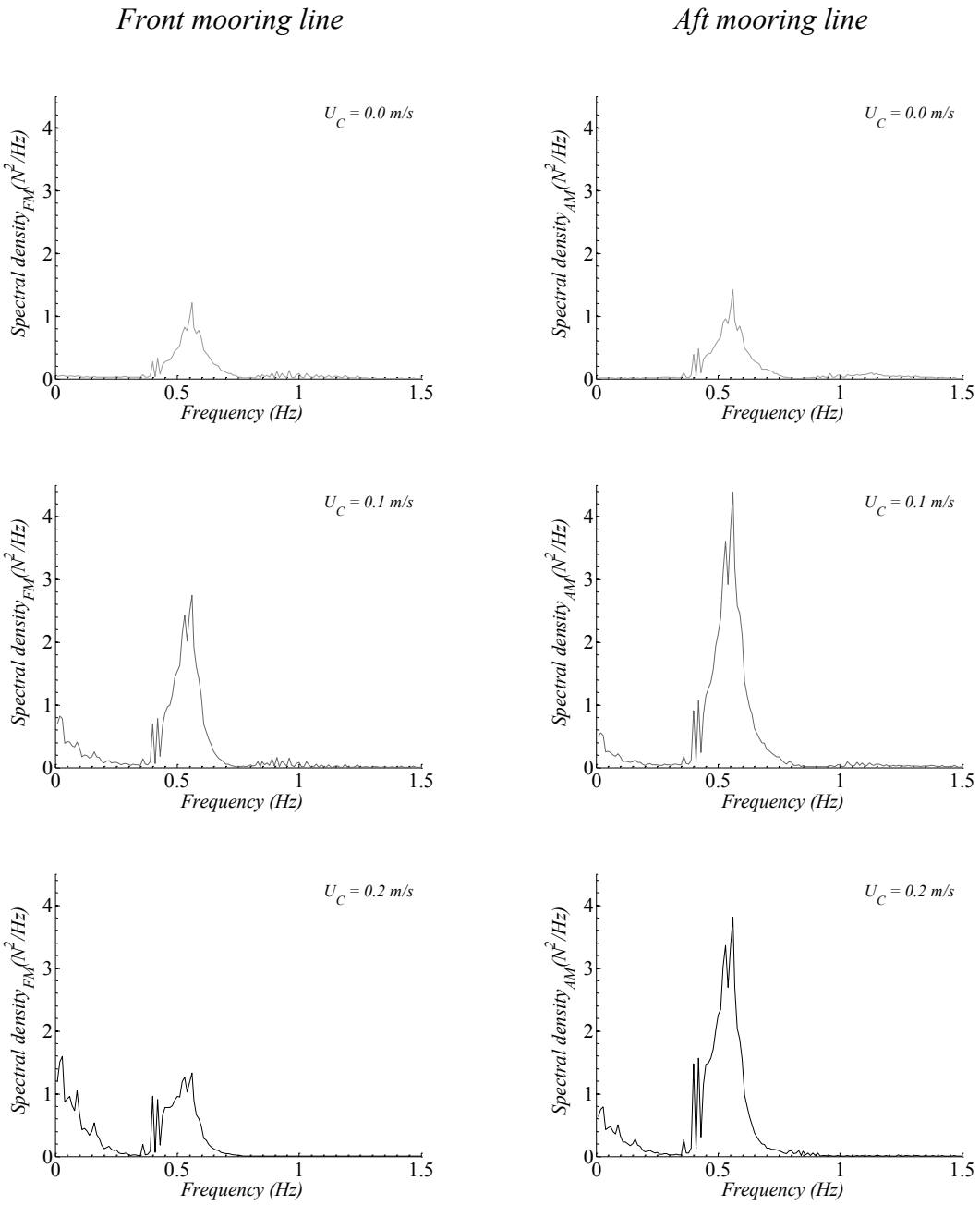

Figure 9.6 Spectral density of mooring tension under current and irregular wave loading

Given the irregular wave current interaction results, it seems evident that the correct numerical description of wave's effect is critical in the determination of the hydrodynamic response of cages. This is particularly important for strong current and steep waves where the effect of current and waves over mooring line tension is of similar significance. To complete the analysis, the transfer function is presented based on the wave spectra obtained from wave elevation time series at each particular current speed case. Transfer function is defined as follows.

$$\left|TF\right|_{Tension} = \sqrt{S_{TT} / S_{\eta\eta}} \tag{9.5}$$

where S_{TT} is defined as mooring tension spectra and $S_{\eta\eta}$ is input wave spectra.

The transfer function (TF) shows that for low frequencies, where there is no wave energy, a large peak in load is seen due to the low frequency loading given by current. Even for the case of wave only, there is energy at the low frequency area due to wave drift force over the cage. As for the wave frequency range between 0.4 and 1.5 Hz the TF flattens and decreases as frequency increases. This indicates that the tension on the mooring lines reacts linearly to the wave forcing. This response has been observed in numerical, experimental and in situ measurements (DeCew et al., 2005; Fredriksson et al., 2003b; Xu et al., 2011) confirming the findings in the present analysis.

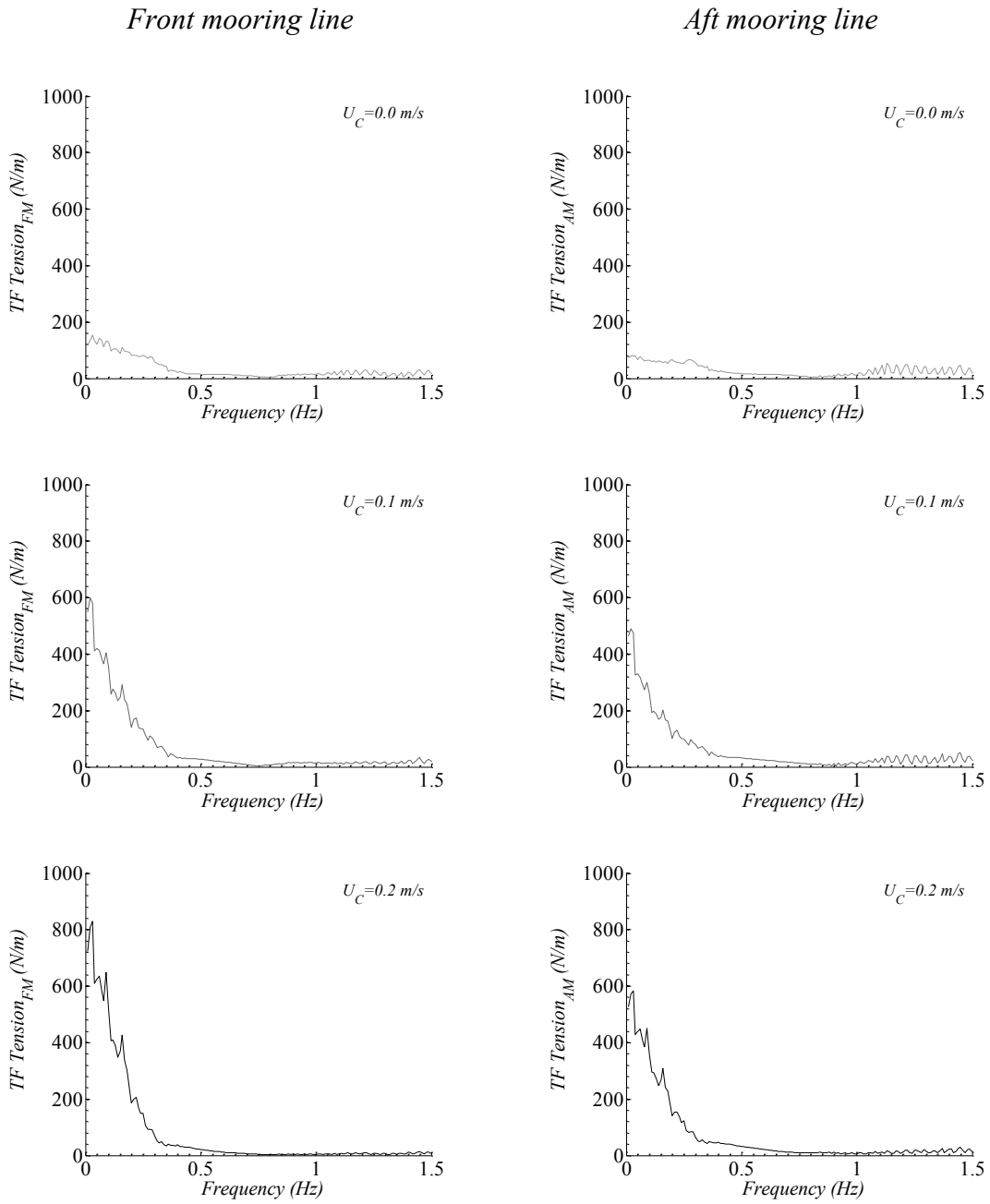

Figure 9.7 Transfer function of mooring tension under current and irregular wave loading

9.4 Cage motion analysis under irregular waves

Another interesting analysis for a floating structure deals with the motion of the platform when exposed to irregular waves and currents. This analysis helps to identify possible dangerous scenarios of operation as well as correlate motion and loads over the cage. For the case of a cage using a flexible surface collar, motion in the surge and heave direction are relevant since they are directly connected to tension on mooring lines. Pitch is not considered in the analysis since the surface collar deforms as waves propagates, thus upstream and downstream portions of the collar could be on different phases of motion. As an example pitch could be zero for a wave that deform the cage such as two points at the diameter, in the wave propagation direction, are at the same height while the collar is in sag condition.

A complete analysis considering the correlation between motion, mooring line tension and wave elevation is carried out to relate these components of the dynamic response of the cage. As mentioned earlier, few analysis have considered irregular waves and none of them has included a wake model for the net, thus the information provided in this section intends to be useful for the design of systems planned to operate in exposed locations. Important information can be extracted from the results since during operation; measurements of motion can directly be transferred to tension loads serving as a monitoring check for the health of mooring system. Calculation for time series of motion and frequency analysis are performed as well as statistics of the results are presented for the same exposed wave and current conditions used in the previous sections.

In order to describe the motion of the cage, a point located in the surface collar in the intersection of the wave propagation plane and a plane perpendicular to this direction is used. In the next figure, a representation of the surface collar and wave propagation direction helps to locate point *S* which will describe the motion of the cage in the following set of results.

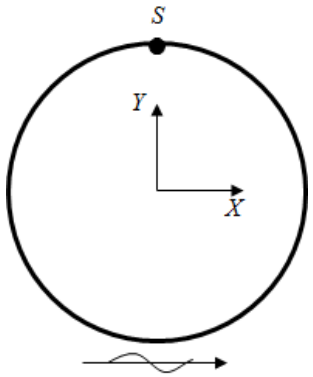

Figure 9.8 Coordinate describing cage motion

The simplest analysis of the effects of current loads and wave can be obtained by analyzing the time series of motion presented in Figure 9.9. As previously seen on the analysis of tension loads on mooring lines, the effect of steady current over the system is a shift of the mean values for surge motion. Surge motion is directly related to mooring line tension, thus its response to waves and current is similar. In the case of motion, the increase on surge is linear respect to the intensity of current speed. As for heave, current does not play a role in the variation of the response of the cage. Heave motion only depend on wave conditions which is confirmed by the analysis of the statistics on Table 9.7.

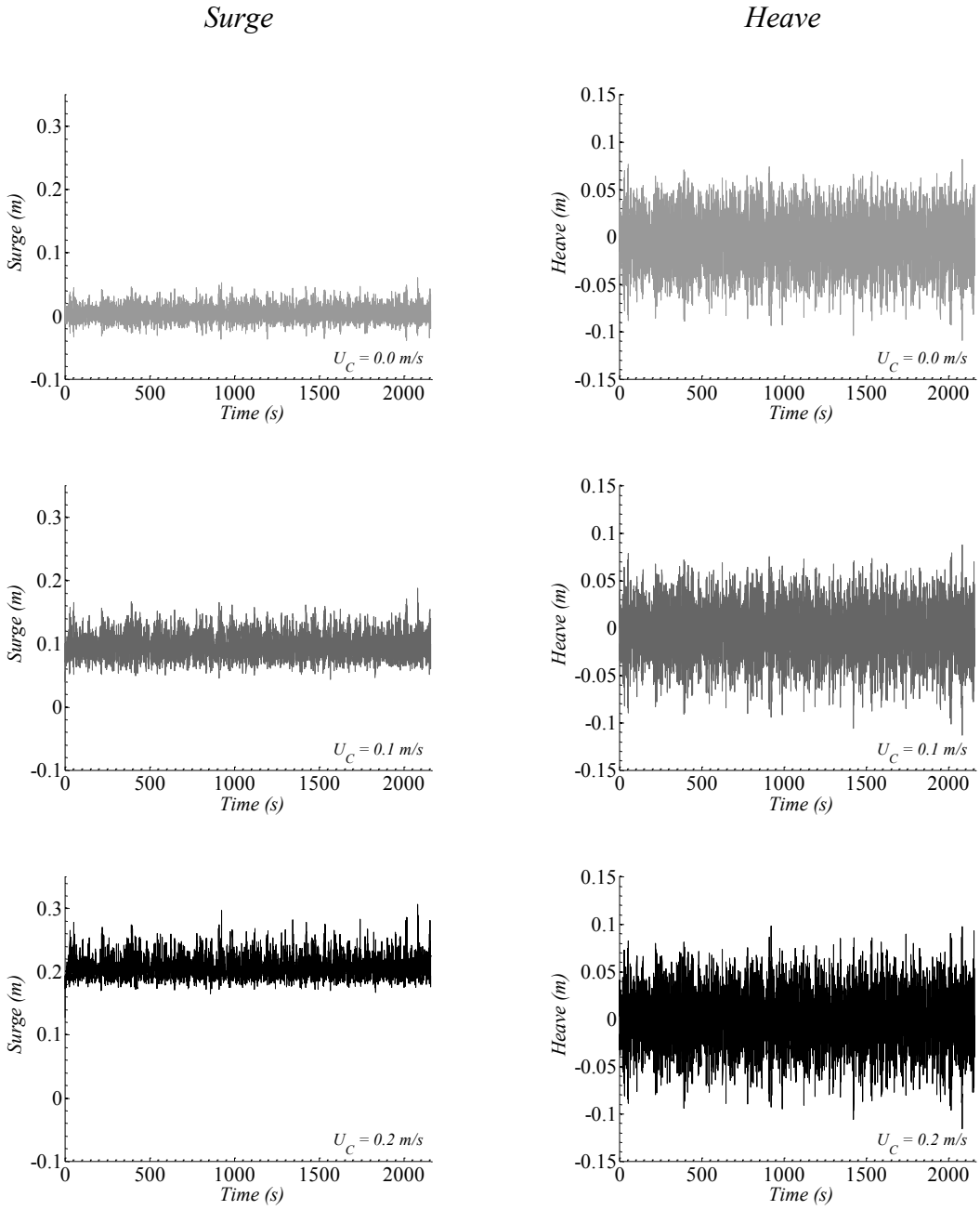

Figure 9.9 Cage motion under irregular wave loading

Table 9.6 Statistics for surge cage motion under irregular waves

Current, U_C (m/s)	Wave parameters		Surge (m)			
	$H_{1/3}$ (m)	T_p (s)	Mean	SD	Max	Min
0.0	0.12	1.8	0.003	0.01	0.06	-0.04
0.1			0.098	0.018	0.188	0.044
0.2			0.208	0.016	0.306	0.165

Table 9.7 Statistics for heave cage motion under irregular waves

Current, U_C (m/s)	Wave parameters		Heave (m)			
	$H_{1/3}$ (m)	T_p (s)	Mean	SD	Max	Min
0.0	0.12	1.8	-0.005	0.025	0.081	-0.11
0.1			-0.003	0.025	0.087	-0.11
0.2			0.0	0.027	0.098	-0.11

Based on the statistics and time series for surge and heave motion, the motion response of the cage is uncoupled, meaning there is no correlation between heave and surge motion. While surge is correlated to current speed, heave motion is only affected by wave motion. Its amplitude is unchanged when current speed increases.

Heave is highly correlated with wave elevation across current speed conditions. The cage basically follows the wave motion in the vertical direction. This phenomenon is described in the next figure where time series of heave motion and wave elevation are compared.

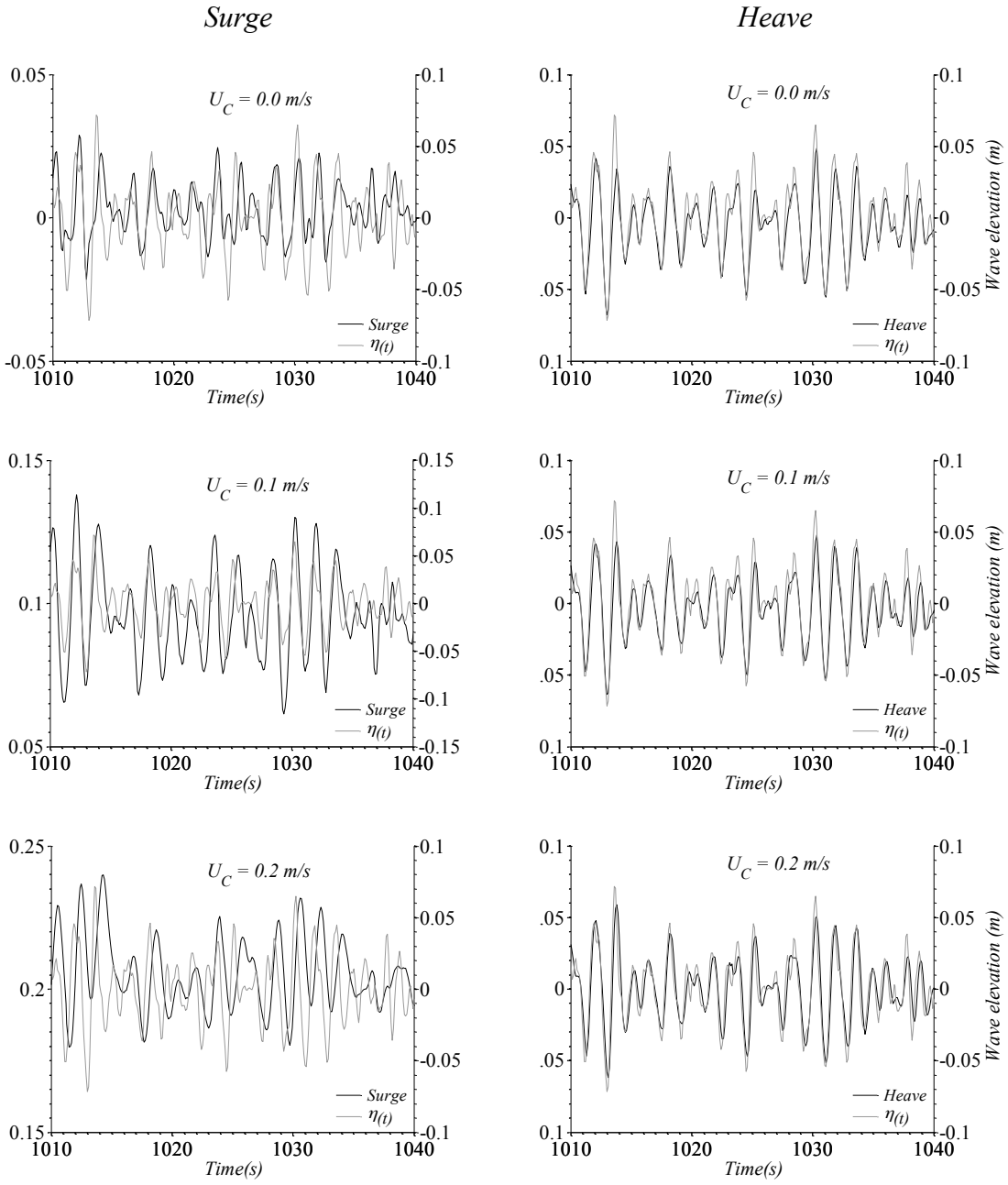

Figure 9.10 Wave elevation and cage motion under irregular wave loading

From the previous comparison, the phase of heave motion and wave elevation shows how the cage reacts immediately to wave elevation. As for surge motion, a lag becomes more evident as current speed increase. This effect is a combination of initial pretension on the mooting line as well as the mean displacement of the cage due to current loading.

To better analyze the response of the cage, the spectral density of the response is calculated. For surge and heave motion, the contribution from wave frequencies is predominant, except for the case with the strongest current speed, where the contribution is almost equal between wave and low frequency. At high frequencies, there is no response of the cage which confirms previous findings by other researchers whom catalogued a cage as a system with high damping since almost no motion can be observed outside wave frequencies.

The response in heave motion, as seen before, does not change as current speed increases.

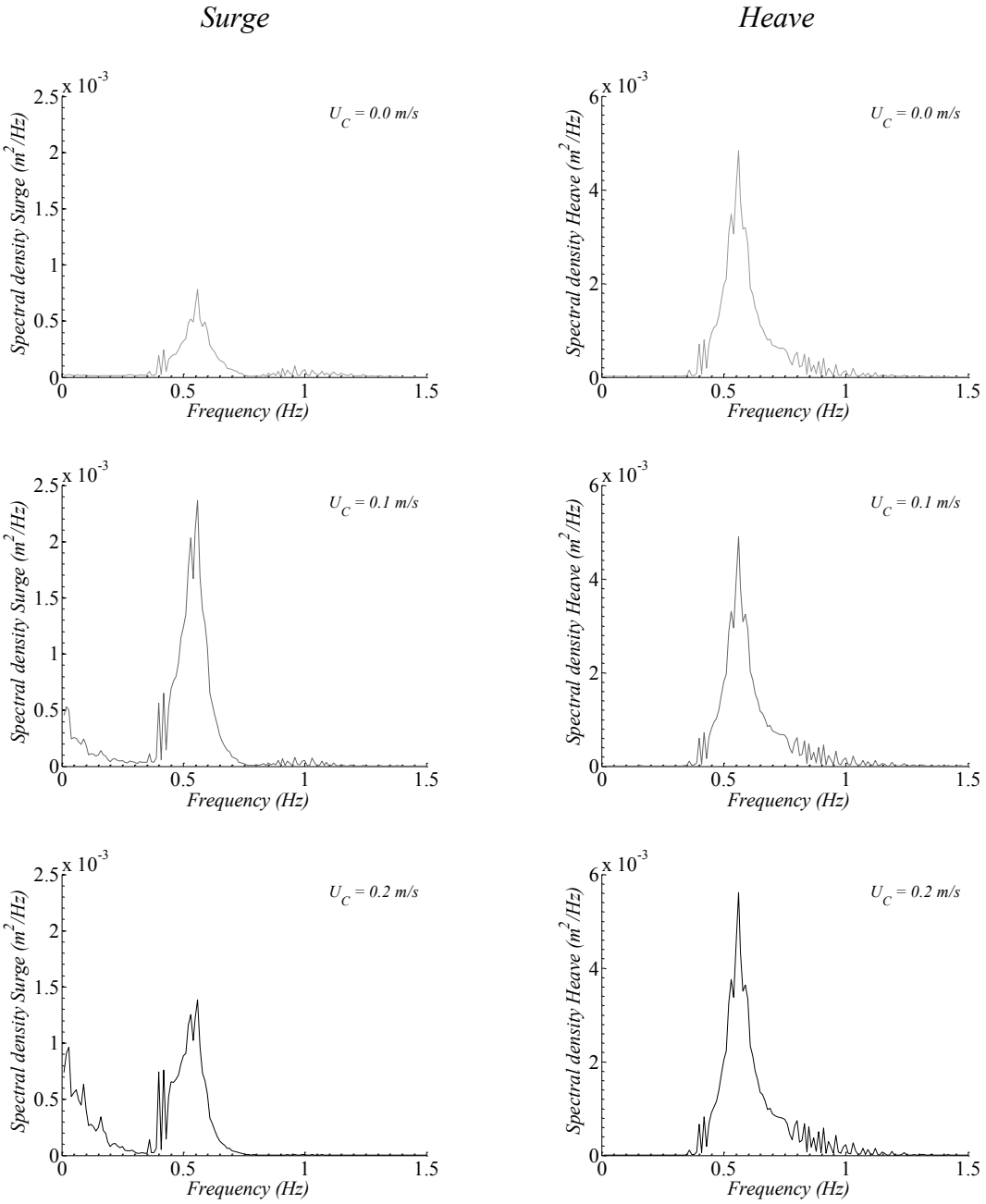

Figure 9.11 Spectral density of cage motion under current and irregular wave loading

The next step in the motion analysis considers the calculation of the transfer function which is defined as follows for surge and heave motion.

$$\left|TF\right|_{Surge} = \sqrt{S_{XX} / S_{\eta\eta}} \tag{9.6}$$

$$\left|TF\right|_{Heave} = \sqrt{S_{ZZ} / S_{\eta\eta}} \tag{9.7}$$

Surge shows a correlation in the wave frequency area where the curve flattens. For low frequency, the peak in surge is explained by the current effect which dominates the low frequency response of the cage. As for heave, in the wave frequency region a typical response is observed based on experimental and in situ analysis (Fredriksson et al., 2003b). In heave, a resonant response occurs at low frequencies. This response can be attributed to the heave damped natural frequency of the cage which was measured for a similar cage to be close to 0.045 Hz (Fredriksson et al., 2003a).

The heave response at the high frequency range corresponds to the noise on the spectra generated by the wave elevation time series for each case and it is considered to be a numerical issue since by increasing the length of the simulation the theoretical and wave elevation time series spectra will get closer. Another reason for the large response at high frequencies could be attributed to the low bending stiffness of the surface collar which can react at short oscillation periods. This needs further investigation using a structural analysis of the surface collar to be certain about this high frequency response.

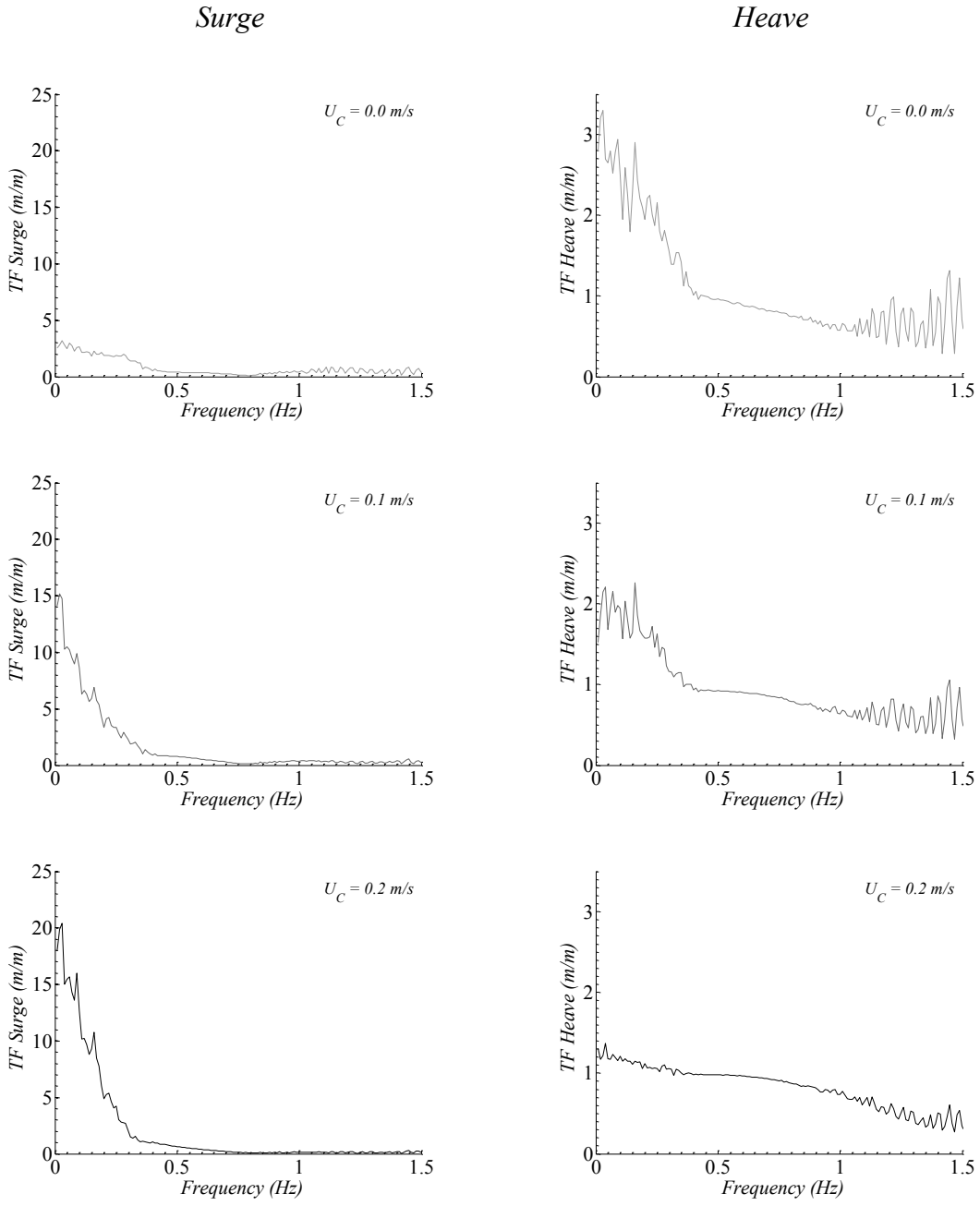

Figure 9.12 Transfer function of cage motion under current and irregular wave loading

The effect of the mean current load is presented in the transfer function plots. As the tension on the front mooring line increases, the cage is restricted to freely move in the vertical direction, reducing the heave response of the system significantly at low frequencies. This could be beneficial in the design of mooring systems where an increase in the pretension on the line could damp the heave resonant response of the cage.

9.5 Discussion

The complete analysis of forces and motion of a single cage under irregular waves and following current was carried out. The focus of the analysis was to find the relation between mooring line tension, motion and wave elevation. Results presented in frequency and time domain show the close correlation between surge and mooring line tension as well as the dominant effect of current loads over the system. The analysis shows that the effect of waves and current is not the result of a linear superposition of waves and current, but the effect is more complex and need to be addressed in a coupled analysis. As current speed increases, the tension on the mooting lines increases almost linearly which is similar to the results when considering only current loads. The combination of waves and current translates into a displacement of the mean values of tension in addition to an increase in the peak values. Spectral analysis reveals that there is response at low and wave frequencies. A double peak can be observed for the higher current speed showing same amplitude for low and wave frequency responses for some cases. No response is seen above wave frequency response in tension which correlates with previous findings of high damping levels at high frequencies. The transfer function

analysis shows the same trend on the wave frequency as seen from field data experiments, plus the contribution from the low frequency component which shows the response of the mooring lines at current speed loading.

As for motion analysis, an interesting feature is obtained in heave motion. Heave is highly correlated to wave elevation and it is not affected by current speed. Surge and heave motion are uncoupled. In addition, surge motion is highly correlated with mooring line tension. Similar trends can be observed in the spectral analysis of surge and tension on the front mooring line component. As current speed increase a low frequency response becomes more significant. For heave motion, the spectral response is almost the same across current speed regimes. On the other hand, when calculating TF for heave, a resonance is observed at low frequency which can possibly correspond to the heave natural frequency of the cage as reported by other researchers. This peak decreased as the tension on the mooring line increases due to the drag load over the netting. This could help in the design of mooring system which reduces the response of the cage at resonance frequencies.

Overall the results prove to follow the response in tension and motion of other analysis considering in situ measurements, experiments as well as numerical calculations which validates the current procedure. The novelty in the current analysis lies on the inclusion of multiple effects such as shielding and blockage effect in addition to a realistic bending stiffness of the surface collar.

Further analysis, considering the full cage using cover at the top and bottom as well as a ballast collar at the bottom, need to be addressed to complement the current

state of the knowledge of the hydrodynamic response of cages under irregular wave loading. However, this analysis shows the main features of the motion and mooring tension response, and serves as foundation for further discussions.

10. COUPLED ANALYSIS OF MOORING/PLATFORM/CAGE SYSTEM UNDER IRREGULAR WAVES AND CURRENT[۞]

10.1 Introduction

The final goal of this research is the determination of the hydrodynamic response of a fish farm installed in what is considered exposed locations for cages. For oil and gas platforms, water depth over 1000 m. can be considered deep water while for a fish farm this definition changes and water depth over 100 m. is considered deep since most of the development has been done in coastal shallow waters. The deepest installation of a fish farm is described in Cifuentes and Kim (2015b) at a water depth of 6000 ft. Future developments are being discussed in Norway for installations up to 300 m depth.

In offshore conditions, a fish farm will have a particular layout where the feeder platform and cages will share the same mooring system and would have to operate under minimum human interaction. In exposed areas, a single point mooring line arise as an adequate alternative for mooring since the cage will have the ability to move over a wide circle generating excellent growing conditions for the fish (DeCew et al., 2010; Shainee et al., 2014). In addition, the installation of such a system is simple and can be accomplished by the use of heavy ballast as anchor.

[۞] Part of this section is reprinted with permission from "Dynamic Analysis for the Global Performance of An SPM-Feeder-Cage System Under Waves and Currents" by C. Cifuentes and M. H. Kim 2015. China Ocean Engineering, vol. 29, no. 3, pp 415-430. Copyright © 2015 Chinese Ocean Engineering Society and Springer-Verlag Berlin Heidelberg.

In the present study, the dynamic response of a coupled SPM-feeder-cage system under irregular waves and shear currents is analyzed. A numerical model is developed using the commercial software Orcaflex. Hydrodynamics coefficients of the vessel are calculated by using a 3D diffraction/radiation panel program (WAMIT). First- and second-order wave forces are included in the calculations. The dynamic response of the coupled system was analyzed for various environments and net materials. The results of the study show the effects of solidity ratio of the net and vertical position of the cage on the overall dynamic response of the system, confirming the viability of this type of configuration for future development of offshore aquaculture in deep waters.

The target system is similar to the one used by Kampachi Farms LLC which operated from November 2013 until July 2014 at a site 6-km offshore Kona, Hawaii.

10.2 Description of components

A fish farm operation includes the mooring system, a feeder barge and cages. The dynamic response of this ensemble under strong current and waves is the main target of this study. In this section, we have studied the hydrodynamic response of a coupled SPM/Feeder vessel/Cage system installed at 1828 m. water depth.

10.2.1 Cage

In this case, a circular cage (PolarCirkel™) has been considered including a double pipe upper collar and a single pipe bottom collar. The upper collar is the main buoyancy element while the bottom collar houses the ballast necessary to fully extend

the net while exposed to current loading. Also, additional ballast allocated in the bottom collar allows the cage to go underwater avoiding wave loads over the structure. The main characteristics of the cage are included in Table 10.1.

Table 10.1 Cage characteristics

Parameter	Value	Unit
Cage model	PolarCirkel	~
Upper and lower collar material	HDPE	~
Material density (kg/m^3)	958	~
Upper collar pipe diameter (m)	0.315	(m)
Standard circumference (m)	94	(m)
Standard cage diameter (m)	30	(m)
Cage draft (m)	10.5	(m)
Distance between floating pipes (m)	0.66	(m)
Thickness of floating pipes (m)	0.017	(m)
Lower collar pipe diameter (m)	0.2	(m)

The selection of this type of cage was based on its flexibility, which dissipates energy when exposed to high-energy sea conditions. Plus, HDPE does not corrode while installed in seawater.

10.2.2 Netting materials

The net is the main source of viscous drag load in the system. In this case two different net materials are used. The first is a copper alloy mesh and the second is a combination of Dyneema® fibers and stainless steel wires. Table 10.2 describes the main particulars of each material.

There are significant differences between the two netting materials. A heavier net reduces the deformation of the cage under current. On the other hand, the higher solidity ratio increases the drag force augmenting the tension load over the mooring components. For the case of lighter net, the solidity ratio and mass are more representative of typical nets used in industry.

In this study, the net buoyancy of the cage/net arrangement is the same for the two types of mesh materials. This will serve to reveal the effect of S_n over the global response of the coupled model. The net buoyancy was adjusted by the use of ballast at the bottom collar considering an excessive buoyancy of the cage equal to 1 ton for underwater calculations. This ballast is uniformly distributed at the bottom collar to keep the cage in horizontal position. In addition, a surface buoy at the top of the cage compensates for the extra weight applied, keeping the cage at the target depth during the first stage of the computation.

Table 10.2 Netting characteristics

Parameter	UR-30	Predator-X
Material	Copper alloy	Dyneema® /stainless steel
Solidity ratio	0.18	0.14
Twine diameter (cm)	0.4	0.21
Thread length (cm)	4.45	2.82
Aperture form	Diamond	Square knotless
Density (kg/m^3)	8400	2590
Mass per unit area (kg/m^2)	5.08	0.653

10.2.3 Mooring lines and buoys

The mooring system consists of the SPM line connecting the surface gear to the seafloor, lines connecting the SPM to the vessel and the umbilical line connecting the vessel to the cage. The calculation of the maximum tension on these lines is the main concern at the design stage. For the main SPM line, a combination of chain and nylon rope has been employed. The SPM line segmentation is as follows: 219 m. chain at the seabed followed by a 3428 m. nylon section and a 10m. chain segment at the top connected to the main surface buoy. The properties of both materials are presented in Table 10.3. The chain section is a 2" stud link and the nylon portion is a 1 ½" 8 strand multiplait.

Table 10.3 Mooring lines material properties

Material	Dry mass (kg/m)	Minimum breaking load (kN)
Stud link chain	55	1370
Nylon rope	3.87	223

For simplicity of the study, the line from the SPM buoy to vessel and the umbilical line between the vessel and cage have been designed using the same properties as the nylon section of the SPM line.

The system includes two buoys at the sea surface. The main buoy is located at the top of the SPM line and helps to support its weight. This buoy has 2 m^3 net buoyancy. The second buoy is used when the cage is located at the underwater position. The buoy has 1.5 m^3 net buoyancy and helps to keep the cage balanced during underwater operation of the cage. Buoys do not generate significant drag or inertia loads due to its small size and mass compared to the cage and vessel. Therefore their detailed hydrodynamics is not accounted for in the simulations.

10.2.4 Feeder vessel

In the present study, we use a ship-shape platform as feeder. Its hydrodynamic responses have been derived using its hydrodynamic coefficients calculated from a 3D diffraction/radiation solver. These data are integrated into the time-domain simulation program to carry out a coupled dynamic analysis. Using the methodology described, we are able to calculate the effect of the cage over the vessel response as well as over the

mooring lines. Table 10.4 presents the geometry and inertia properties of the feeder vessel.

In Figure 10.1, the complete numerical model for the system including the cage at the surface position is presented.

Table 10.4 Feeder vessel characteristics

Parameter	Magnitude
Length between perpendiculars (m)	25
Breadth (m)	3.87
Draught (m)	1.61
Transverse GM (m)	0.44
Longitudinal GM (m)	27.67
Center of gravity[1] (m)	(0.61,0,-0.47)
Moment of inertia ($t*m^2$)	(209.67,4.93E3, 4.93E3)
Block coefficient	0.804
Displacement (t)	125.83

[1] Respect to amidships and sea surface

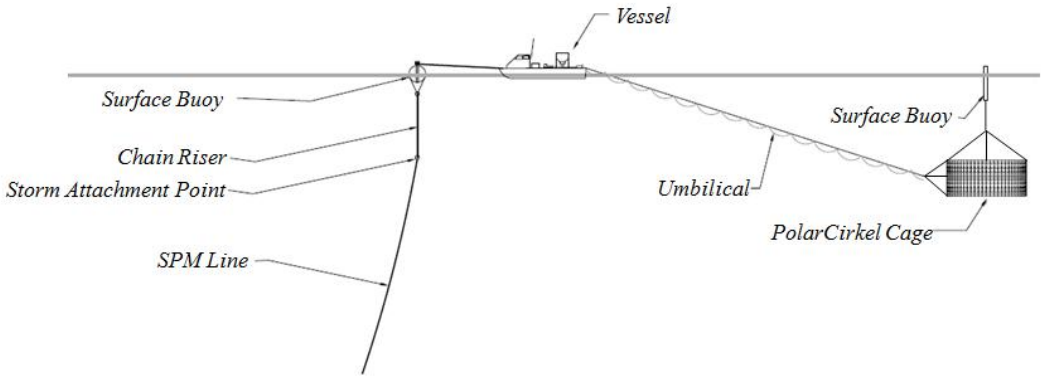

Figure 10.1 Mooring/vessel/cage system

10.3 Environmental conditions

Three environmental conditions were considered in this study. An operational condition is defined as the day-by-day load case in which cage and vessel must operate. Storm and survival conditions are more extreme events. It is important to mention that during storm and survival events, the vessel is not included in the simulation and the cage is connected to the storm attachment point to lessen overall loads. All conditions consider a collinear combination of waves and currents. Jonswap wave spectrum, as described in Goda (2010), was used to define the sea state of each condition.

Given that the target site is 6 km. offshore Kailua, Kona, HI, the environmental conditions were selected to represent an exposed site according to Norway Standard (2009). Under this condition, the system operates as described in Figure 10.1.

The environmental conditions used in the Gulf of Mexico (GOM) for storms with 10 and 100-year return periods were used to model the storm and survival scenarios. Under these sea states, the vessel will leave the site and the cage will be connected to the mooring line by the storm attachment point described in Figure 10.1. The characteristics

of each storm event were extracted from the API code applied to the central region of GOM. Table 10.5 presents the input data for Jonswap spectrum in each scenario.

Table 10.5 JONSWAP spectrum input data

Scenario	$H_{1/3}$ (m)	T_p (s)	γ	Max. current speed (m/s)
Operational condition	3	9	1	1
Storm condition	10	13	2.4	1.65
Survival condition	15.8	15.4	2.4	2.4

10.4 Results

Results will be presented for the vessel and cage motions as well as the tension over the mooring system. The first set of results considers the coupled analysis of the mooring /vessel/ cage system under the operational condition previously defined. The change on the response of the coupled arrangement when the position of the cage is modified in the water column is also investigated. It is of particular interest to look into the wave-current interaction effect on the cage when placed at the sea surface. In this case, a higher tension and larger surge is expected due to the wave drift over the upper collar. The dynamics of the vessel will also be presented for both net materials and cage positions to reveal the influence of the cage on the support platform's response.

10.4.1 Underwater cage results

Positioning the cage underwater protects the structure form wave loading. In this case, the upper collar of the cage is located at 10 meters below the water surface at the initial step of the calculation. Simulations were extended up to 3 hours, which is typical for offshore platforms. The tension time series of the SPM and umbilical lines are presented in Figures 10.2 and 10.3.

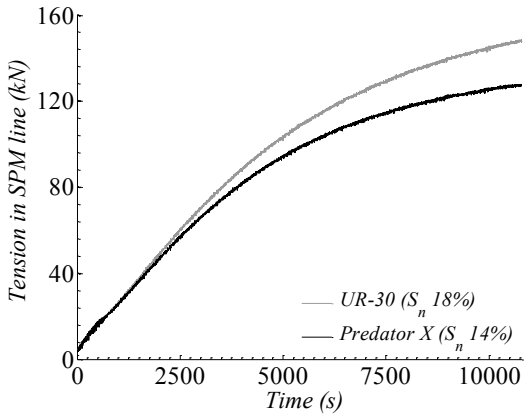

Figure 10.2 SPM line tension for underwater cage

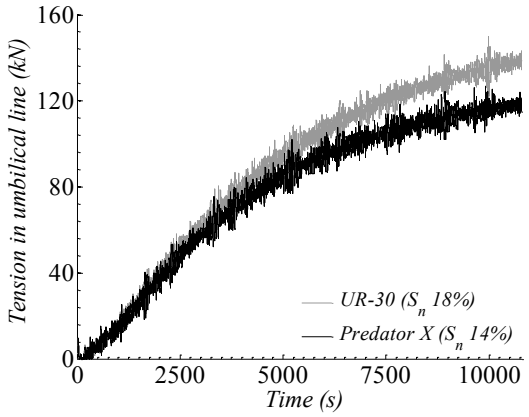

Figure 10.3 Umbilical line tension for underwater cage

Based on the results, the effect of S_n on the tension in the mooring lines is significant at the end of the simulation period. It can be observed that a mere 4% increase in S_n triggers an upsurge of 17% in SPM and umbilical-line tensions. This increase is explained by the fact that S_n is directly related to projected area. As we increase the projected area, the viscous drag from Morison equation is increased, and thus the tension. For the case of the umbilical line, the mean tension given mainly by viscous drag from the cage is superimposed by the wave-frequency component. The magnitudes of wave-frequency oscillations are small and the main contributors to the tension are the slow drift motion of the vessel and the viscous drag load from the cage. The effect of S_n over the response of the vessel is also analyzed in Figure 10.4.

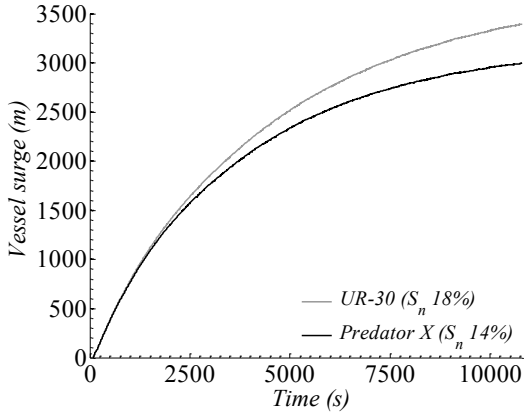

Figure 10.4 Vessel surge for underwater cage

For the case of heave and pitch of the feeder vessel, results are similar for both S_n conditions, given that these motions are dominated by wave frequency and slow drift

motion and nonlinear viscous load do not contribute. This can be observed in Figures 10.5 and 10.6

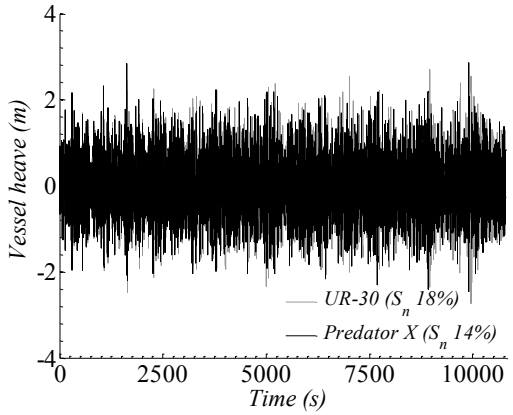

Figure 10.5 Vessel heave for underwater cage

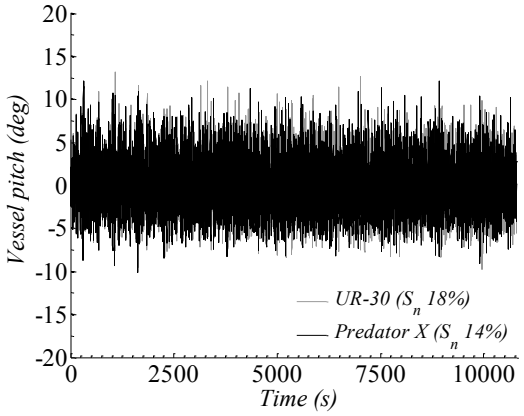

Figure 10.6 Vessel pitch for underwater cage

For both S_n cases, the cage is lifted at the end of the simulation due to the high tension from the umbilical line. This effect moves the upper collar of the cage up to a mean position of 2 m. underwater for the case of S_n =14% and 4 m. underwater for the

case of S_n=18%. This phenomenon observed in Figure 10.7, shows that S_n is also related to the vertical position of the cage due to the combination of viscous drag on the net, tension on the umbilical line, and net buoyancy of the cage structure.

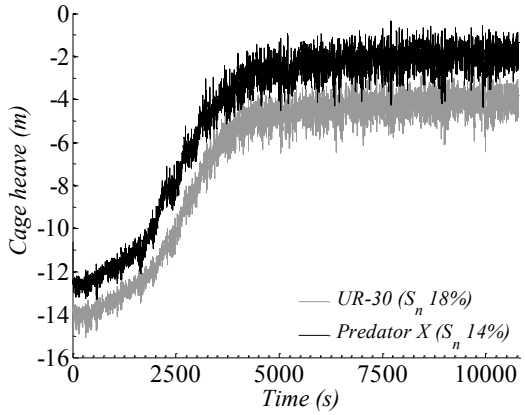

Figure 10.7 Cage heave for underwater cage

From the results, it can be concluded that an increase in S_n largely influences the surge of the platform. In this case, the increase of surge reaches 13% for a 4% increase in S_n. The increase in surge is directly related to the increase in drag force from the net pen. These results typically show the relevance of netting-material selection during the design stage of offshore fish farms. In 2013, a similar system was actually installed in 6000-ft water depth of Hawaii, and such a large horizontal excursion of the system with very long period has been observed by satellite monitoring, which indirectly shows that the present numerical results are reasonable. The actual GPS tracking of the cage in the field is presented as well as the plot for the cage's surge showing that such large

excursion driven by strong surface current is one of the features of a SPM mooring system.

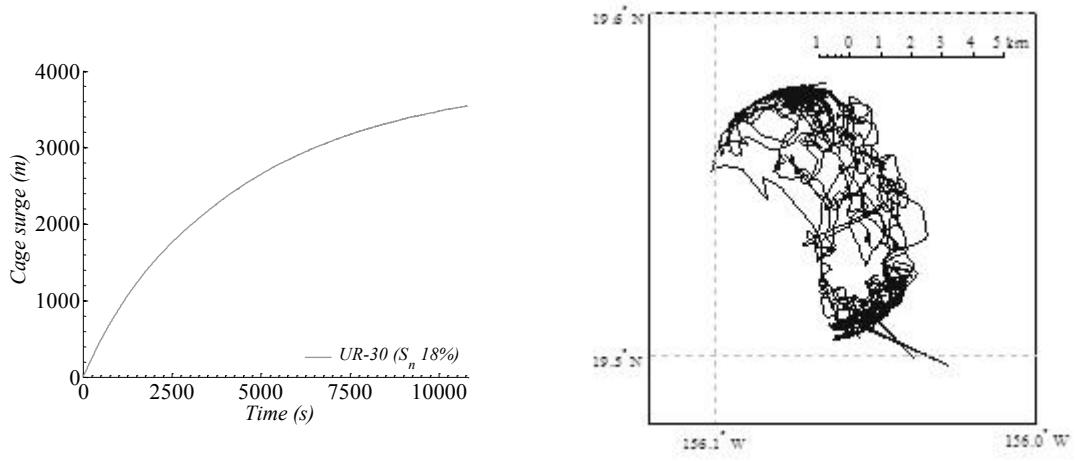

Figure 10.8 Cage surge in underwater conditions (a) Numerical result, (b) GPS tracking.

10.4.2 Surface cage results

In terms of fish-farm operations, locating the cage at the water surface presents better conditions for inspection, cleaning, and control. However, leaving the cage exposed to wave-current maximum loading could potentially lead to high tension especially at the umbilical line. The results for tension in the SPM and umbilical line are presented in Figures 10.9 and 10.10.

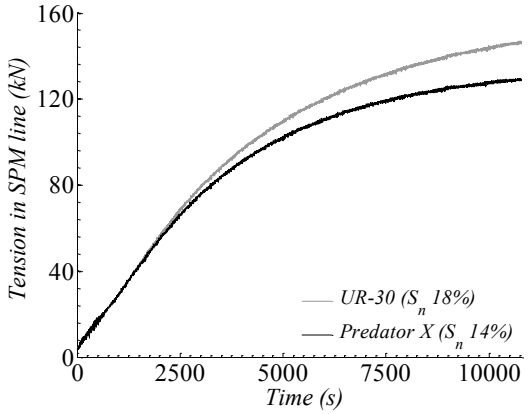

Figure 10.9 SPM line tension for surface cage

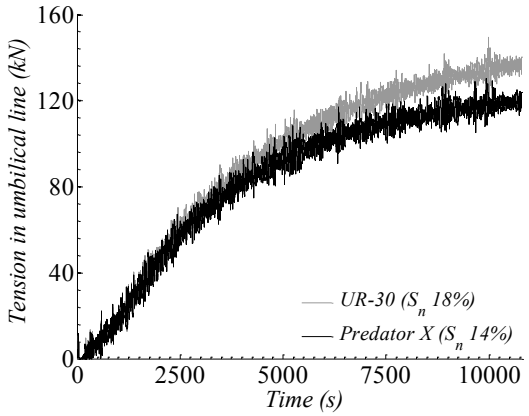

Figure 10.10 Umbilical line tension for surface cage

As in the underwater case, the influence of S_n is significant in the tension of SPM and umbilical lines. The differences are mainly due to the viscous drag over the cage. At the end of the simulation period, the tension for both underwater and surface cases is similar, since the underwater cage is lifted towards the sea surface. As expected, during the period between 2000 s. and 8000 s., the load for the underwater cage is about 10% reduced with respect to the surface cage, which implies that current is a primary source

of drag forces over the structure and wave loading does not significantly increase the tension on the mooring components. Therefore, S_n is the main parameter to consider during the mooring-design stage. The same conclusions are also drawn by Shainee et al (2013) in their experimental work using a single SPM cage under regular waves and following currents. Their results confirm that under wave and current loading, the principal source of tension on mooring lines comes from viscous drag. The effect of the cage over the global response of the vessel is described in Figure 10.11.

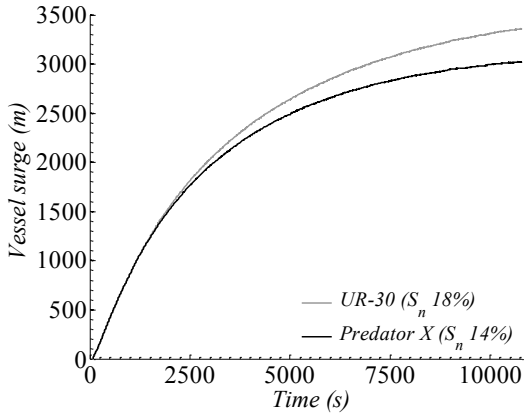

Figure 10.11 Vessel surge for surface cage

The results are similar to the ones for the cage underwater. The main difference can be seen in the surge of the feeder platform. Comparing with the underwater cage, in the region between 2000 s. and 8000 s., the vessel surge is 10% larger for the surface cage due to the increase in drag with additional wave-induced velocity. Since the mooring line is very slack, the natural period and surge of the platform are very large.

10.4.3 Coupled mooring cage system

Under storm conditions, the feeder vessel is disconnected and escaped. Thus, the system consists of the SPM buoy/line, umbilical line, and cage. Two cases are studied; a 10-yr storm event and a more extreme event considering a 100-year return period. Under severe weather, the SPM system allows the cage to go underwater. This self submerge characteristic is ideal for exposed locations. Previous analyses of this type of systems have demonstrated that under a constant current profile and waves, the cage finds its equilibrium position in the water column. This location is correlated to the intensity of current speed (M. Shainee et al., 2013; Mohamed Shainee et al., 2013; Shainee et al., 2014) and the S_n of the net material (DeCew et al., 2010). In the present study, strong shear currents are applied in combination with irregular waves. The umbilical line is attached to the Storm Attachment Point as described in Figure 10.1 and the initial position of the cage is 10 meters underwater.

10.4.4 10 Year storm condition

Under a 10 year storm, it is expected that the structure will not suffer any considerable damage and that operations can be resumed after the event. The current profile considers that the maximum current will go up to 35 m. underwater; below that, the current speed is reduced to 1.24 m/s until water depth reaches 70 m. and becomes zero from there to the seabed.

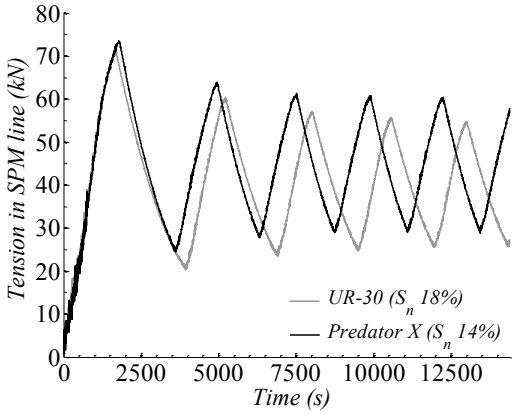

Figure 10.12 SPM line tension under 10 year storm event

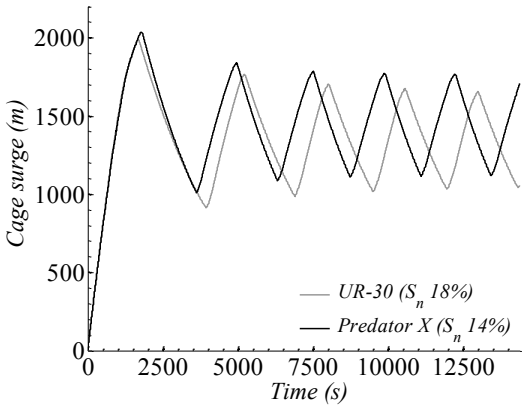

Figure 10.13 Cage surge under 10 year storm event

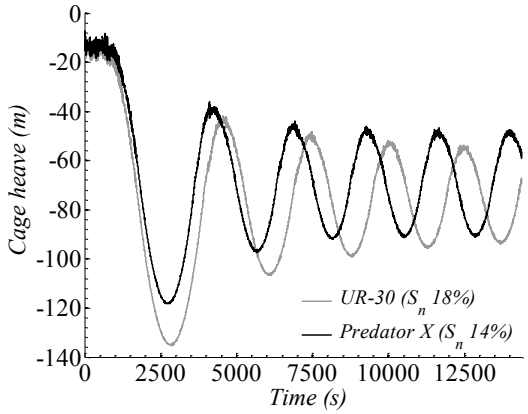

Figure 10.14 Cage heave under 10 year storm event

Results presented for the tension at the SPM line and the surge/heave of the cage in Figures 10.12 to 10.14 show that under the imposed environment, the cage enters into an oscillatory cycle both in surge and heave. This particular behavior is a consequence of the interaction of net buoyancy of the cage, positive buoyancy from surface buoy, tension of connection lines, and the depth-varying shear current. The mean of the heave motion for both net materials is close to the boundary of 1.24 m/s current and zero-current zone. During downward motion, the vertical downward component of the tension at the connection line overcomes the positive net buoyancy from the surface buoy and cage pulling the cage deep down into the water column. After the cage enters in the area of zero current, the downward tension is reduced and the positive buoyancy lifts the cage, this cycle is repeated over the simulation period. An interesting finding is that the tension and surge motion are in phase. This effect can also be seen in the influence of S_n. An increase in S_n extends the period of oscillation. Also, the peaks in surge and heave differ in about 15% for both net materials. In the wave-current condition analyzed, the

system is able to withstand the environmental loads and no failure is expected since the maximum calculated tensions are significantly smaller than the minimum breaking loads of the materials used for the system.

10.4.5 100 Year storm condition

The corresponding results are presented in Figures 10.15 to 10.17. In this case, the current is significantly stronger compared to the previous case i.e. the surface current is 2.4 m/s and is reduced to 1.8 m/s at 50-m water depth. Deeper than 100-m water depth, current speed is zero

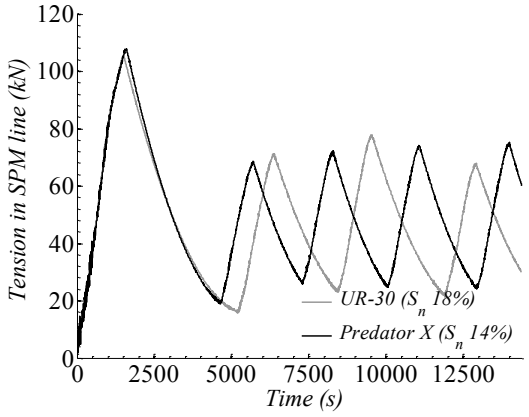

Figure 10.15 SPM line tension under 100 year storm event

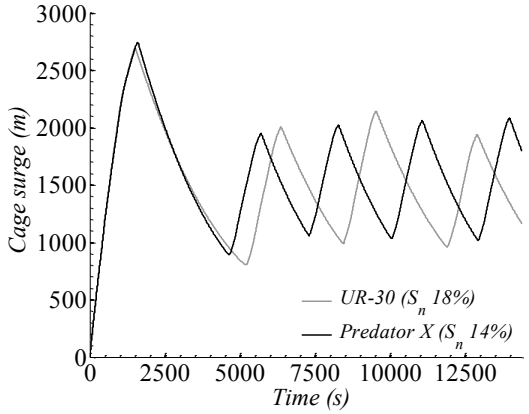

Figure 10.16 Cage surge under 100 year storm event

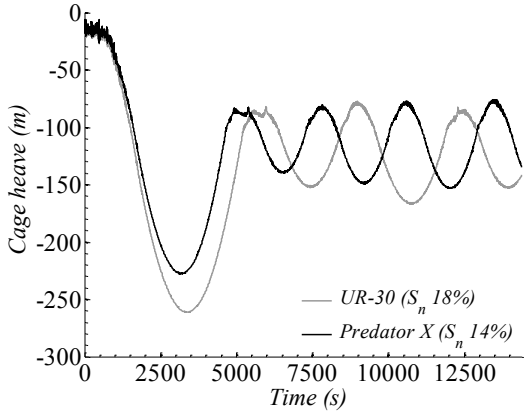

Figure 10.17 Cage heave under 100 year storm event

Similar to the 10-yr storm condition, the cage goes into a cycle driven by current speed, implying that the overall physics are analogous. With the increased current speed, the period of oscillation gets longer. The cage locates its mean position slightly below the starting point of zero-current zone. This can be observed for both net materials. It is also interesting that the period of oscillation becomes appreciably different when varying S_n; however, the tension is similar for both cases. The mean tension between the storm

and extreme event is similar since the net buoyancy of the cage/buoy system is the same. Nevertheless, the maximum tension in the initial transient phase is much more pronounced in the survival condition, which needs to be taken into consideration in the design. The dynamic tension amplitudes are also appreciably increased for both net materials compared to the 10-yr storm case.

10.5 Conclusions

The complete dynamic analysis of the global response of a SPM/Vessel/Cage system in time domain has been achieved. The analysis was performed using the nonlinear finite element software Orcaflex which has mostly been used for the coupled dynamic analysis of floating production facilities. The numerical modeling of the net was based on the equivalent drag concept by using a combination of lines and buoys. The hydrodynamic forces on the system are obtained by the use of Morison equation accounting for the normal relative velocity and acceleration between structural elements and fluid flow. Particular attention was given to the selection of adequate drag coefficients to obtain accurate results covering a wide range of Reynolds number.

The simulation of a coupled SPM/vessel/cage system under two different system arrangements, corresponding to three different environments was performed. Two net materials with different S_n ratio were used to exemplify the effect of net selection over the dynamic response of the structure.

In operational conditions, the initial position of the cage was varied over the water column to understand its effect on the global dynamic response. The solidity ratio

of the net considerably impacts the tension on the SPM line as well as the surge of the vessel and cage. On the other hand, the positon of the cage over the water column does not significantly influence the heave and pitch responses of the platform.

In 10-yr and 100-yr storm events without feeder vessel, the cage exhibits cyclic behaviors with respect to mean positions in line tension and surge/heave responses. The driving force over this effect is the combination of vertical tension and net buoyancy of the cage. The mean depths reached by the cage, the initial transient effects, and amplitudes of oscillations are appreciably increased in the survival (100-yr) condition. The maximum tension and displacement of the system show that the structure is able to withstand the extreme event. The results show that a SPM system coupled to a floating platform could potentially be a viable option for the future offshore fish farms in open oceans.

11. CONCLUSIONS AND FUTURE WORK

11.1 General conclusions

The description of the interaction between mooring, vessel and a single cage under a wide range of environmental conditions has been presented. The effect of the net nonlinear drag over the vessel´s motions and loads on the mooring system is fully described, providing valuable information for future design, installation and maintenance of fish farms installed in deep water. The study suggests that a SPM mooring line is a viable alternative for deep water installations since allows the cage to align with the dominant wave and current direction, increasing water exchange inside the cage. Net selection is also discussed describing a great impact on loads due to small changes on geometry.

Cage location over the water column mainly impacts vessel´s surge motion. Pitch and heave motion do not show differences when the cage is installed either at sea surface or underwater. However, to protect the fish from breaking waves and higher wave loading, the study suggests that an underwater cage is the best alternative under normal operations. Cage can be taken to the sea surface only on harvesting and possible net cleaning operations.

Before the coupled analysis, a complete validation of the methodology adopted in this work was presented. Each step of the numerical simulation of flexible structures under wave and current load has been carefully analyzed. The simples case being a cylindrical net exposed to steady current which helped to weight on the relevance of

shielding effect on the simulations. The application of interaction models derived for risers proved to be adequate for nets improving the accuracy of the results when compared to experimental values. The use of a variable drag coefficient formulation based first on simple cylinders and then on net geometry and Reynolds numbers, helped to increase the range of current velocities for which the methodology can be applied. The model can integrate complex phenomenon such as shielding and blockage effects. This method also proved to be valuable for the study hydrodynamics on slender bodies such as Submerged Floating Tunnel.

The model was extended to the floating collar which becomes relevant under waves and current. The highly flexible structure interacts with mooring lines thus its numerical description must be carefully done considering structural and hydrodynamic aspects. The methodology, selecting drag and inertia coefficient based on *KC* and *Re* numbers showed good agreement with experiments capturing the loads and deformations of the cage. In addition, a rational analysis of the effect of wave kinetic extrapolation methods reveled that Wheeler approximation is the adequate model for cage dynamics calculations. The study revealed the relative importance of wave and current loading. For long and high waves, current and wave loading are equally relevant for mooring tension.

Finally, a rational analysis of a single cage under irregular waves and current showed the correlation between motion, mooring tension and wave elevation in frequency and time domain. The study showed that for most of waves inside the spectra utilized, the cage follows the waves. At low frequency, current dominates the motion

and loading. At high frequencies, local deformations of the collar are observed. Resonance of the system at low frequencies were captured which is in accordance with previously published field data.

Overall, the methodology presented in this work shows great potential for further applications in offshore fish farming. It successfully integrates the complex hydrodynamic problems for slender flexible structures and vessel motion under waves and currents. The findings proved to be in close agreement with experimental and field measurements establishing a solid start point for further research.

11.2 Future work

Based on the findings presented in this work as well as the state of the art on the calculation of forces and deformations on cages, both numerical and experimental work needs to be done in order to further understand this complex problem.

The main uncertainty in the numerical determination of forces comes from the fact that only the cylindrical portion of the cage has been considered so far for numerical validation. The effect of a horizontal net panel at the top and bottom of the cage enclosing the internal volume is yet to be included. The flow pattern and forces when the net panel is tangent to the flow, as in the upper portion of the cage it is still unknown. As for the bottom portion, experimental data is available for a cylindrical main cage body with a cone at the bottom, yet no numerical assessment of this configuration has been carried out. Experimental studies of different nets under tangential and near tangential flow are needed to get closer to actual operational conditions. In addition, numerical and

experimental studies need to include the ballast ring and lines connecting this ring to the surface collar to account for possible clashing between components and estimation of fatigue loads which can lead to escapes.

In terms of loading, experiments including irregular waves and current need to be performed. No information other than numerical results are available and thus, further validation of those calculations are needed. Numerically, failure analysis of mooring and umbilical components were performed, but not included in this document for copyright reasons; however, based on those preliminary results, failure of connections can induce large loads over the floater and lead to potential failures, thus experimental and numerical validation of those phenomenon is another interesting area of work.

After full validation of a more detailed cage system is performed, the integration of technologies is another interesting point to study. Nowadays the integration of floating wind power and aquaculture is being analyzed in Europe. Therefore, the numerical coupled analysis of cages and floating wind turbines is a prominent area of future research.

The last and probably most challenging work to be done is full scale experimental analysis. Up to now, SINTEF Norway and University of New Hampshire have carried out full scale experiments; however, the conditions tested are particular to those sites. Applications to other locations are necessary to account for local environmental conditions as well as mooring installation procedures and operation protocols.

REFERENCES

Aarnes, J. V, Loland, G., 1990. Current foces on cage, net deflection, in: Engineering for Offshore Fish Farming. London, pp. 137–152.

Bae, Y.H., 2013. Coupled dynamic analysis of multiple unit floating offshore wind turbine. PhD Diss. Texas A&M University.

Bae, Y.H., Kim, M.H., 2014. Coupled dynamic analysis of multiple wind turbines on a large single floater. Ocean Eng. 92, 175–187. doi:10.1016/j.oceaneng.2014.10.001

Bardestani, M., Faltinsen, O.M., 2013. A two dimensional approximation of a floating fish farm in waves and current with the effect of snap loads, in: Proceedings of the ASME 2013 32nd International Conference on Ocean, Offshore and Arctic Engineering OMAE2013. Nantes, France, pp. 1–10.

Bi, C.W., Zhao, Y.P., Dong, G.H., Xu, T.J., Gui, F.K., 2014a. Numerical simulation of the interaction between flow and flexible nets. J. Fluids Struct. 45, 180–201. doi:10.1016/j.jfluidstructs.2013.11.015

Bi, C.W., Zhao, Y.P., Dong, G.H., Xu, T.J., Gui, F.K., 2013. Experimental investigation of the reduction in flow velocity downstream from a fishing net. Aquac. Eng. 57, 71–81. doi:10.1016/j.aquaeng.2013.08.002

Bi, C.W., Zhao, Y.P., Dong, G.H., Zheng, Y.N., Gui, F.K., 2014b. A numerical analysis on the hydrodynamic characteristics of net cages using coupled fluid-structure

interaction model. Aquac. Eng. 59, 1–12. doi:10.1016/j.aquaeng.2014.01.002

Blevins, R.D., 2005. Forces on and Stability of a Cylinder in a Wake. J. Offshore Mech. Arct. Eng. 127, 39. doi:10.1115/1.1854697

Blevins, R.D., Wu, M., 2007. Investigation of Interference Between Upstream and Downstream Cylinders in a Current for the HRTs and Jumpers W ith FPSO Application, in: Offshore Technology Conference. Houston, pp. 1–8.

Casarella, M.J., Parsons, M., 1970. Cable Systems under hydrodynamic loading. Mar. Technol. Soc. J. 4.

Chakrabarti, S.K., 1987. Hydrodynamics of Offshore Structures. Springer, New York.

Choo, Y.-I., Casarella, M.J., 1971. Hydrodynamic Resistance of Towed Cables. J. Hydronautics 5, 126–131. doi:10.2514/3.62882

Chung, J., Hulbert, G.M., 1993. A Time Integration Algorithm for Structural Dynamics With Improved Numerical Dissipation: The Generalized-α Method. J. Appl. Mech. 60, 371. doi:10.1115/1.2900803

Cifuentes, C., Kim, M.H., 2015a. Numerical simulation of wake effect in nets under steady current, in: ASME (Ed.), Proceedings of the ASME 2015 34th International Conference on Ocean, Offshore and Arctic Engineering OMAE2015. St. John's, Newfoundland, Canada, pp. 1–10.

Cifuentes, C., Kim, M.H., 2015b. Dynamic analysis for the global performance of an SPM-feeder-cage system under waves and currents. China Ocean Eng. 29, 415–

430. doi:10.1007/s13344-015-0029-8

Cifuentes, C., Kim, M.H., 2014. Numerical simulation of shielding effect in nets under steady current, in: Aquaculture America 2014. p. 6.

Cifuentes, C., Kim, M.H., Sims, N.A., Key, G., 2014. Coupled Analysis of a SPM Buoy-Feeder- Cage System for Offshore Aquaculture, in: Proceedings of the Twenty-Fourth (2014) International Ocean and Polar Engineering Conference. Busan, Korea, pp. 949–955.

DeCew, J., Celikkol, B., Rice, G., Tsukrov, I., 2006. Practical Applications of Numerical Modeling using Aqua-FE : A Case Study, in: OCEANS 2006. IEEE, Boston, MA. doi:10.1109/OCEANS.2006.307137

DeCew, J., Fredriksson, D.W., Bugrov, L., Swift, M.R., Eroshkin, O., Celikkol, B., 2005. A case study of a modified gravity type cage and mooring system using numerical and physical models. IEEE J. Ocean. Eng. 30, 47–58. doi:10.1109/JOE.2004.841400

DeCew, J., Fredriksson, D.W., Lader, P.F., Chambers, M., Howell, W.H., Osienki, M., Celikkol, B., Frank, K., Høy, E., 2013. Field measurements of cage deformation using acoustic sensors. Aquac. Eng. 57, 114–125. doi:10.1016/j.aquaeng.2013.09.006

DeCew, J., Tsukrov, I., Risso, a., Swift, M.R., Celikkol, B., 2010. Modeling of dynamic behavior of a single-point moored submersible fish cage under currents. Aquac. Eng. 43, 38–45. doi:10.1016/j.aquaeng.2010.05.002

Di Pilato, M., Perotti, F., Fogazzi, P., 2008. 3D dynamic response of submerged floating tunnels under seismic and hydrodynamic excitation. Eng. Struct. 30, 268–281. doi:10.1016/j.engstruct.2007.04.001

Dong, G.H., Xu, T.J., Zhao, Y.P., Li, Y.C., Gui, F.K., 2010. Numerical simulation of hydrodynamic behavior of gravity cage in irregular waves. Aquac. Eng. 42, 90–101. doi:10.1016/j.aquaeng.2009.12.004

Endresen, P.C., 2011. Vertical Wave Loads and Response of a Floating Fish Farm with Circular Collar. Norwegian University of Science and Technology.

Endresen, P.C., Fore, M., Fredheim, A., Kristiansen, D., Enerhaug, B., Føre, M., Kristiansen, D., 2013. Numerical modeling of wake effect on aquaculture nets, in: Proceedings of the ASME 2013 32nd International Conference on Ocean, Offshore and Arctic Engineering OMAE2013. Nantes, France, pp. 1–10.

Enerhaug, B., Føre, M., Endresen, P.C., Madsen, N., Hansen, K., 2012. Current loads on net panels with rhombic meshes, in: ASME (Ed.), Proceedings of the ASME 2012 31th International Conference on Ocean, Offshore and Arctic Engineering OMAE 2011. Rio de Janeiro, Brazil, pp. 1–12.

Eom, T.S., Kim, M.H., Bae, Y.H., Cifuentes, C., 2014. Local dynamic buckling of FPSO steel catenary riser by coupled time-domain simulations. Ocean Syst. Eng. 4, 215–241.

Faltinsen, O.M., 1993. Sea loads on ships and offshore structures. Cambridge University Press.

Faltinsen, O.M., Structures, O., Technology, M., 2011. Hydrodynamic aspects of a floating fish farm with circular collar. Proc. 26th Int. onWaterWaves Float. Bodies 1–4.

FAO, 2014. The State of World Fisheries and Aquaculture 2014. FAO.

Fredheim, A., 2005. Current forces on net structures. Norwegian University of Science and Technology.

Fredriksson, D.W., DeCew, J.C., Tsukrov, I., Swift, M.R., Irish, J.D., 2007. Development of large fish farm numerical modeling techniques with in situ mooring tension comparisons. Aquac. Eng. 36, 137–148. doi:10.1016/j.aquaeng.2006.10.001

Fredriksson, D.W., Irish, J.D., Swift, M.R., Celikkol, B., 2003a. The Heave Response of a Central Spar Fish Cage. J. Offshore Mech. Arct. Eng. 125, 242. doi:10.1115/1.1600471

Fredriksson, D.W., Swift, M.R., Irish, J.D., Tsukrov, I., Celikkol, B., 2003b. Fish cage and mooring system dynamics using physical and numerical models with field measurements. Aquac. Eng. 27, 117–146. doi:10.1016/S0144-8609(02)00043-2

Fu, S., Xu, Y., Hu, K., Zhang, Y., 2013a. Experimental investigation on hydrodynamics of floating cylinder in oscillatory and steady flows by forced oscillation test. Mar. Struct. 34, 41–55. doi:10.1016/j.marstruc.2013.08.005

Fu, S., Xu, Y., Hu, K., Zhang, Y., 2013b. Experimental investigation on hydrodynamics

of floating cylinder in oscillatory and steady flows by forced oscillation test. Mar. Struct. 34, 41–55. doi:10.1016/j.marstruc.2013.08.005

Gansel, L.C., McClimans, T. a., Myrhaug, D., 2012. Average Flow Inside and Around Fish Cages With and Without Fouling in a Uniform Flow. J. Offshore Mech. Arct. Eng. 134, 041201. doi:10.1115/1.4006150

Gansel, L.C., Plew, D.R., Endresen, P.C., Olsen, A.I., Misimi, E., Guenther, J., Jensen, Ø., 2015. Drag of Clean and Fouled Net Panels – Measurements and Parameterization of Fouling. PLoS One 10. doi:10.1371/journal.pone.0131051

Garrett, D.L., 1982. Dynamic Analysis of Slender Rods. J. Energy Resour. Technol. 104, 302. doi:10.1115/1.3230419

Goda, Y., 2010. Random seas and design of maritime structures. World Scientific Publishing Company.

Haritos, N., He, D.T., 1992. Modelling the response of cable elements in an ocean environment. Finite Elem. Anal. Des. 11, 19–32. doi:10.1016/0168-874X(92)90026-9

Hong, Y., Ge, F., 2010. Dynamic response and structural integrity of submerged floating tunnel due to hydrodynamic load and accidental load. Procedia Eng. 4, 35–50. doi:10.1016/j.proeng.2010.08.006

Huang, C.C., Tang, H.J., Wang, B.S., 2010. Numerical modeling for an in situ single-point-mooring cage system. IEEE J. Ocean. Eng. 35, 565–573.

doi:10.1109/JOE.2010.2050351

Huse, E., 1996. Experimental investigation of deep sea riser interaction. Proc. Annu. Offshore Technol. Conf. 2, 367–372.

Huse, E., 1993. Interaction in Deep-Sea Riser Arrays, in: Offshore Technology Conference. Houston, Texas, pp. 3–6.

Jakobsen, B., 2010. Design of the Submerged Floating Tunnel operating under various conditions. Procedia Eng. 4, 71–79. doi:10.1016/j.proeng.2010.08.009

Jensen, Ø., Dempster, T., Thorstad, E., Uglem, I., Fredheim, a, 2010. Escapes of fishes from Norwegian sea-cage aquaculture: causes, consequences and prevention. Aquac. Environ. Interact. 1, 71–83. doi:10.3354/aei00008

Jia, H., Moan, T., Jensen, Ø., 2012. Coupled hydrodynamic analysis between gravity cage and well boat in operation. Proc. Int. Offshore Polar Eng. Conf. 4, 1055–1062.

Kang, H., Kim, M.H., 2014. Hydroelastic Analysis and Statistical Assessment of Flexible Offshore Platforms. Int. J. Offshore Polar Eng. 24, 35–44.

Kim, M.H., Koo, B.J., Mercier, R.M., Ward, E.G., 2005. Vessel/mooring/riser coupled dynamic analysis of a turret-moored FPSO compared with OTRC experiment. Ocean Eng. 32, 1780–1802. doi:10.1016/j.oceaneng.2004.12.013

Klebert, P., Lader, P., Gansel, L., Oppedal, F., 2013. Hydrodynamic interactions on net panel and aquaculture fish cages: A review. Ocean Eng. 58, 260–274. doi:10.1016/j.oceaneng.2012.11.006

Kristiansen, D., Lader, P., Jensen, Ø., Fredriksson, D., 2015. Experimental study of an aquaculture net cage in waves and current. China Ocean Eng. 29, 325–340.

Kristiansen, T., Faltinsen, O.M., 2015. Experimental and numerical study of an aquaculture net cage with floater in waves and current. J. Fluids Struct. 54, 1–26. doi:10.1016/j.jfluidstructs.2014.08.015

Kristiansen, T., Faltinsen, O.M., 2012. Modelling of current loads on aquaculture net cages. J. Fluids Struct. 34, 218–235. doi:10.1016/j.jfluidstructs.2012.04.001

Kunisu, H., 2010. Evaluation of wave force acting on Submerged Floating Tunnels. Procedia Eng. 4, 99–105. doi:10.1016/j.proeng.2010.08.012

Kunisu, H., Mizuno, S., Mizuno, Y., Saeki, H., 1994. Study on Submerged Floating Tunnel Characteristics Under the Wave Condition, in: Proceedings of the Fourth (1994) International Offshore and Polar Engineering Conference. Osaka, Japan, pp. 27–32.

Lader, P., Fredriksson, D.W., Guenther, J., Volent, Z., Blocher, N., Kristiansen, D., Gansel, L., DeCew, J., 2015. Drag on hydro-fouled nets -An experimental approach. China Ocean Eng. 29, 369–389.

Lader, P., Fredriksson, D.W., Volent, Z., DeCew, J., Rosten, T., Strand, I.M., 2014. Drag forces on, and deformation of, closed flexible bags, in: ASME (Ed.), Proceedings of the ASME 2014 33rd International Conference on Ocean, Offshore and Arctic Engineering OMAE2014. ASME, San Francisco, California, pp. 1–9.

Lader, P., Jensen, A., Sveen, J.K., Fredheim, A., Enerhaug, B., Fredriksson, D., 2007. Experimental investigation of wave forces on net structures. Appl. Ocean Res. 29, 112–127. doi:10.1016/j.apor.2007.10.003

Lader, P.F., Enerhaug, B., 2005. Experimental investigation of forces and geometry of a net cage in uniform flow. IEEE J. Ocean. Eng. 30, 79–84. doi:10.1109/JOE.2004.841390

Lader, P.F., Fredheim, A., 2006. Dynamic properties of a flexible net sheet in waves and current-A numerical approach. Aquac. Eng. 35, 228–238. doi:10.1016/j.aquaeng.2006.02.002

Li, L., Fu, S., Xu, Y., 2013a. Nonlinear hydroelastic analysis of an aquaculture fish cage in irregular waves. Mar. Struct. 34, 56–73. doi:10.1016/j.marstruc.2013.08.002

Li, L., Fu, S., Xu, Y., Wang, J., Yang, J., 2013b. Dynamic responses of floating fish cage in waves and current. Ocean Eng. 72, 297–303. doi:10.1016/j.oceaneng.2013.07.004

Løland, G., 1993. Current forces on, and water flow through and around, floating fish farms. Aquac. Int. 1, 72–89. doi:10.1007/BF00692665

Lu, W., Ge, F., Wang, L., Wu, X., Hong, Y., 2011. On the slack phenomena and snap force in tethers of submerged floating tunnels under wave conditions. Mar. Struct. 24, 358–376. doi:10.1016/j.marstruc.2011.05.003

Lu, W., Ge, F., Wu, X., Hong, Y., 2013. Nonlinear dynamics of a submerged floating

moored structure by incremental harmonic balance method with FFT. Mar. Struct. 31, 63–81. doi:10.1016/j.marstruc.2013.01.002

Moe, H., Fredheim, a., Hopperstad, O.S., 2010. Structural analysis of aquaculture net cages in current. J. Fluids Struct. 26, 503–516. doi:10.1016/j.jfluidstructs.2010.01.007

Moe, H., Olsen, A., Hopperstad, O.S., Jensen, Ø., Fredheim, A., 2007. Tensile properties for netting materials used in aquaculture net cages. Aquac. Eng. 37, 252–265. doi:10.1016/j.aquaeng.2007.08.001

Moe-Føre, H., Christian Endresen, P., Gunnar Aarsæther, K., Jensen, J., Føre, M., Kristiansen, D., Fredheim, A., Lader, P., Reite, K.-J., 2015. Structural Analysis of Aquaculture Nets: Comparison and Validation of Different Numerical Modeling Approaches. J. Offshore Mech. Arct. Eng. 137, 041201. doi:10.1115/1.4030255

Moe-Føre, H., Endresen, P.C., Aarsæther, K.G., Jensen, J., Føre, M., Kristiansen, D., Fredheim, A., Lader, P., Reite, K.-J., Christian Endresen, P., Gunnar Aarsæther, K., Jensen, J., Føre, M., Kristiansen, D., Fredheim, A., Lader, P., Reite, K.-J., 2014. Structural analysis of aquaculture nets: comparison and validation of different numerical modelling approaches, in: Proceedings of the ASME 2014 33rd International Conference on Ocean, Offshore and Arctic Engineering OMAE2014. San Francisco, California, p. 041201. doi:10.1115/1.4030255

Morison, J.R., Johnson, J.W., Schaaf, S. a., 1950. The Force Exerted by Surface Waves on Piles. J. Pet. Technol. 2, 149–154. doi:10.2118/950149-G

Norway Standard, 2009. “NS 915:2009” Marine fish farms - Requirements for site survey, risk analyses, design, dimensioning, production, installation and operation.

Oh, S.-H., Park, W.S., Jang, S.-C., Kim, D.., Ahn, H.., 2013. Physical experiments on the hydrodynamic response of submerged floating tunnel against the wave action, in: Proceedings of the 7th International Conference on Asian and Pacific Coasts (APAC 2013). Bali, Indonesia, pp. 582–587.

Orcina, 2014. OrcaFlex Manual Version 9.8a. Ulverston, Orcina.

Østlid, H., 2010. When is SFT competitive? Procedia Eng. 4, 3–11. doi:10.1016/j.proeng.2010.08.003

Patursson, Ø., Swift, M.R., Tsukrov, I., Simonsen, K., Baldwin, K., Fredriksson, D.W., Celikkol, B., 2010. Development of a porous media model with application to flow through and around a net panel. Ocean Eng. 37, 314–324. doi:10.1016/j.oceaneng.2009.10.001

Romolo, A., Malara, G., Barbaro, G., Arena, F., 2008. An Analytical Approach for the Calculation of Random Wave Forces On Submerged Tunnels, in: Proceedings of the ASME 27th International Conference on Offshore and Arctic Engineering OMAE2008. Elsevier Ltd, Estoril, Portugal, pp. 1–7. doi:10.1016/j.apor.2009.04.001

Sarpkaya, T., 1976. Vortex shedding and resistance in harmonic flow about smooth and rough circular cylinders at high reynolds numbers. Monterrey, California.

Shainee, M., DeCew, J., Leira, B.J., Ellingsen, H., Fredheim, a., 2013. Numerical simulation of a self-submersible SPM cage system in regular waves with following currents. Aquac. Eng. 54, 29–37. doi:10.1016/j.aquaeng.2012.10.007

Shainee, M., Decew, J., Leira, B.J., Ellingsen, H., Fredheim, A., 2013. Self submersible SPM cage simulation in regular waves with oblique currents, in: Proceedings of the ASME 2013 32nd International Conference on Ocean, Offshore and Arctic Engineering OMAE2013. Nantes, France, pp. 1–8.

Shainee, M., Leira, B.J., Ellingsen, H., Fredheim, a., 2014. Investigation of a self-submersible SPM cage system in random waves. Aquac. Eng. 58, 35–44. doi:10.1016/j.aquaeng.2013.10.003

Sims, N.A., Key, G., 2011. Fish without footprints: a beta-test of the Velella concept to evaluate environmental and economic benefits of unanchored open ocean net pens, in: OCEANS 2011. IEEE, Waikoloa, HI.

Swift, M.R., Fredriksson, D.W., Unrein, A., Fullerton, B., Patursson, O., Baldwin, K., 2006. Drag force acting on biofouled net panels. Aquac. Eng. 35, 292–299. doi:10.1016/j.aquaeng.2006.03.002

Tsukrov, I., Drach, A., DeCew, J., Robinson Swift, M., Celikkol, B., 2011. Characterization of geometry and normal drag coefficients of copper nets. Ocean Eng. 38, 1979–1988. doi:10.1016/j.oceaneng.2011.09.019

Tsukrov, I., Eroshkin, O., Fredriksson, D., Swift, M.R., Celikkol, B., 2002. Finite element modeling of net panels using a consistent net element. Ocean Eng. 30,

251–270. doi:10.1016/S0029-8018(02)00021-5

Tsukrov, I.I., Ozbay, M., Swift, M.R., Celikkol, B., Fredriksson, D.W., Baldwin, K., 2000. Open Ocean Aquaculture Engineering: Numerical Modeling. Mar. Technol. Soc. J. 34, 29–40. doi:10.4031/MTSJ.34.1.4

Turner, A.A., Reid, G.K., 2015. Experimental investigation of fish farm hydrodynamic properties on 1:15 scale model circular aquaculture cages, in: ASME (Ed.), Proceedings of the ASME 2015 34th International Conference on Ocean, Offshore and Arctic Engineering OMAE2015. St. John's, Newfoundland, Canada, pp. 1–12.

Wu, M., Saint-Marcoux, J.-F., Blevins, R.D., Quiggin, P., 2008. Innovative 3-D Implementation of Riser Wake Interference Assessment, in: Proceedings of the Eighteenth (2008) International Offshore and Polar Engineering Conference. Vancouver, Canada.

Xu, T.J., Dong, G.H., Zhao, Y.P., Li, Y.C., Gui, F.K., 2011. Analysis of hydrodynamic behaviors of gravity net cage in irregular waves. Ocean Eng. 38, 1545–1554. doi:10.1016/j.oceaneng.2011.07.019

Xu, T.J., Zhao, Y.P., Dong, G.H., Bi, C.W., 2014. Fatigue analysis of mooring system for net cage under random loads. Aquac. Eng. 58, 59–68. doi:10.1016/j.aquaeng.2013.10.004

Xu, T.J., Zhao, Y.P., Dong, G.H., Gui, F.K., 2013. Analysis of hydrodynamic behavior of a submersible net cage and mooring system in waves and current. Appl. Ocean Res. 42, 155–167. doi:10.1016/j.apor.2013.05.007

Yang, C.K., 2009. Numerical modeling of nonlinear coupling between lines/beams with multiple floating bodies. Texas A&M University.

Zhao, Y.P., Bi, C.W., Dong, G.H., Gui, F.K., Cui, Y., Guan, C.T., Xu, T.J., 2013. Numerical simulation of the flow around fishing plane nets using the porous media model. Ocean Eng. 62, 25–37. doi:10.1016/j.oceaneng.2013.01.009